1-12-2015 12:00 AM

Regionally-Adjustable Generic Ground-Motion Prediction Equation

Emrah Yenier, *The University of Western Ontario*

Supervisor: Dr. Gail M. Atkinson, *The University of Western Ontario*
A thesis submitted in partial fulfillment of the requirements for the Doctor of Philosophy degree in Geophysics
© Emrah Yenier 2015

Recommended Citation

REGIONALLY-ADJUSTABLE GENERIC GROUND-MOTION PREDICTION EQUATION

(Thesis format: Integrated Article)

by

Emrah <u>Yenier</u>

Graduate Program in Geophysics

A thesis submitted in partial fulfillment
of the requirements for the degree of
Doctor of Philosophy

The School of Graduate and Postdoctoral Studies
Western University
London, Ontario, Canada

Abstract

We develop a simulation-based generic ground-motion prediction equation (GMPE) that can be adjusted for use in any region by simple modifications to its key modeling parameters.

First, we determine how to treat ground-motion saturation effects observed at close distances to large magnitude earthquakes in a point-source sense. We model the source and attenuation attributes of well-recorded $\mathbf{M} \geq 6$ events, considering ground motions originate from an equivalent point source placed at an overall effective distance such that the empirically-observed saturation effects are successfully reproduced. We investigate the trade-offs between source and attenuation modeling parameters through analysis of Fourier amplitudes for several alternative attenuation models.

Next, we describe response spectra for California earthquakes of $3.0 \leq \mathbf{M} < 7.5$ using stochastic ground-motion simulations based on the equivalent point-source concept. The best-fit simulation model suggests that the attenuation in California can be modeled as $R^{-1.3}$ at distances < 50 km and $R^{-0.5}$ at further distances; this does a better job at matching attenuation trends than the traditional model $1/R$ model at distances < 50 km, particularly for small magnitude events. We develop a stress parameter model for California earthquakes based on matching the simulated and observed response spectral shapes over a wide frequency range. We determine a simulation calibration factor for amplitude adjustment to match the observed spectral amplitudes with zero bias.

Finally, we perform equivalent point-source simulations with parameters calibrated to empirical data in California to determine the decoupled effects of basic source and attenuation parameters on response spectral amplitudes. Based on these isolated effects, we formulate the generic GMPE as a function of magnitude, distance, stress parameter, geometrical spreading rate and anelastic attenuation coefficient. This provides a fully adjustable predictive model, allowing users to calibrate its parameters using observed motions in the target region. As an example application, we show how the generic GMPE can be adjusted for use in central and eastern North America.

Keywords

Co-Authorship Statement

The materials present in Chapters 2, 3, and 4 of this thesis have been previously published or submitted for publication to the peer-reviewed journal of *Bulletin of Seismological Society of America*. This thesis contains only the original results of research conducted by the candidate under supervision of his mentor. The original contributions are summarized as follows:

Compilation and data processing of ground-motion time series for selected earthquakes in Italy, New Zealand and Turkey; Calculation of Fourier acceleration spectra and the closest rupture distances for ground motions studied in Chapter 2; Compilation of seismological parameters as well as peak ground motions and response spectral amplitudes from NGA-West2 and NGA-East flatfiles for the study events in Chapters 3 and 4; Determination of predicted motions from NGA-West1 and NGA-West2 GMPEs; Regression analysis and statistical analysis of residuals; Stochastic equivalent point-source simulations; Analysis of modeling trade-offs and determination of ground-motion saturation parameter; Calculation of stress parameters and simulation calibration factor for California events; Determination of model coefficients for the generic GMPE and its adjustment to the central and eastern North America.

Dr. Gail M. Atkinson is the co-author in all three articles presented in this thesis (Chapters 2, 3 and 4).

Acknowledgments

I would like to express my sincere gratitude to my supervisor, Dr. Gail M. Atkinson, for her continuous support, guidance, encouragement and insight throughout the completion of this thesis.

I would like to extend my appreciation to Dr. Julian J. Bommer, Dr. David M. Boore, Dr. Shahram Pezeshk and Dr. Carola Di Alessandro for their valuable reviews on the papers produced from this research. I also would like express my sincere thanks to Dr. Robert Mereu and Dr. Kristy Tiampo for their useful comments which likewise led to significant improvements in this thesis.

I would like to thank to my labmates and friends, Afshin, Azadeh, Behzad, Beth, Colin, Hadi, Karen, Luqi, Mark, Mingzhou, Sebastian, Abdullah, Murat and Ozgur for their friendship and support.

I am very grateful for my father M. Şerif Yenier, my mother Mebrure Yenier, and my brothers Erkan and Enes, and my sister Sebahat for their endless love, encouragement and confidence in me.

I would like to thank to my wife Zumrut, the angel of my life, for her continuous support, encouragement, patience and unwavering love. I always consider myself the luckiest man in the world since I met her.

Table of Contents

List of Tables

List of Figures

Chapter 1

1 Introduction

1.1 Purpose and significance of the study

Estimation of ground-motion amplitudes that may be produced by future earthquakes constitutes the foundation of seismic hazard assessment and earthquake resistant design. It is typically done by using a ground-motion prediction equation (GMPE) that quantifies amplitudes as a function of key seismological variables such as magnitude, distance and site condition. Prediction equations are typically derived based on ground motions obtained from past earthquakes. However, the empirical data are generally sparse in the magnitude-distance range of engineering interest for many regions, except well-monitored active regions such as California and Japan.

The purpose of this study is to develop a robust generic GMPE that can be adjusted for use in any region by modifying its key modeling parameters. We parameterize the generic GMPE in terms of fundamental source and attenuation parameters based on their isolated effects determined from ground-motion simulations. This approach provides a fully-adjustable predictive model, which has both conceptual and practical advantages. The generic GMPE can be easily calibrated to a target region using the available empirical data. Additionally, alternative GMPEs can be created by considering a range of possible parameter values that might be reasonable for the region to account for epistemic uncertainty in modeling parameters. Analysis of the residual trends and their variability under these alternative models can provide information on the limitations of the alternative parameter sets.

1.2   Stochastic simulation of ground motions

Stochastic simulations are widely used for prediction of ground motions as alternative to empirical methods, particularly in data-poor regions. The Fourier amplitude spectrum model is the essential ingredient in stochastic simulations. The amplitude spectrum is given as the product of source, path and site effects, encapsulating the basic physical processes involved in ground-motion generation (Boore, 2003). The seismic energy defined by the amplitude spectrum is distributed over a finite duration with random phase angles to generate the synthetic ground-motion time series. The algorithm starts with the generation of a Gaussian white noise for a duration related to the earthquake magnitude and distance (Figure 1.1.a). Next, the generated noise is windowed (Figure 1.1.b) and transformed to the frequency domain (Figure 1.1.c). The purpose of windowing is to give a realistic shape to the synthetic time series. The spectrum of the windowed noise is normalized by its root of mean square amplitude (Figure 1.1.d). Then, the normalized spectrum is multiplied by the target Fourier amplitude spectrum model (Figure 1.1.e). Finally, the resulting spectrum is transformed back to the time domain to obtain synthetic ground-motion time series (Figure 1.1.f).

In stochastic simulations, the seismic source can be modeled as either a point-source (e.g., Brune, 1970; Atkinson and Silva 2000; Boore et al., 2014) or a propagating stochastic finite-source (e.g., Motazedian and Atkinson, 2005; Boore, 2009). Point-source models assume that the total seismic energy is released from a single point. In stochastic finite-source models, however, the rupture area is divided into an array of sub-faults each of which is treated as a point-source with appropriate time lags. Source effects are represented by a source spectrum model that is given as a function of seismic moment and stress parameter. The seismic moment has influence on the Fourier amplitude spectrum over all frequencies, primarily at low frequencies, whereas the stress parameter controls high-frequency spectral amplitudes.
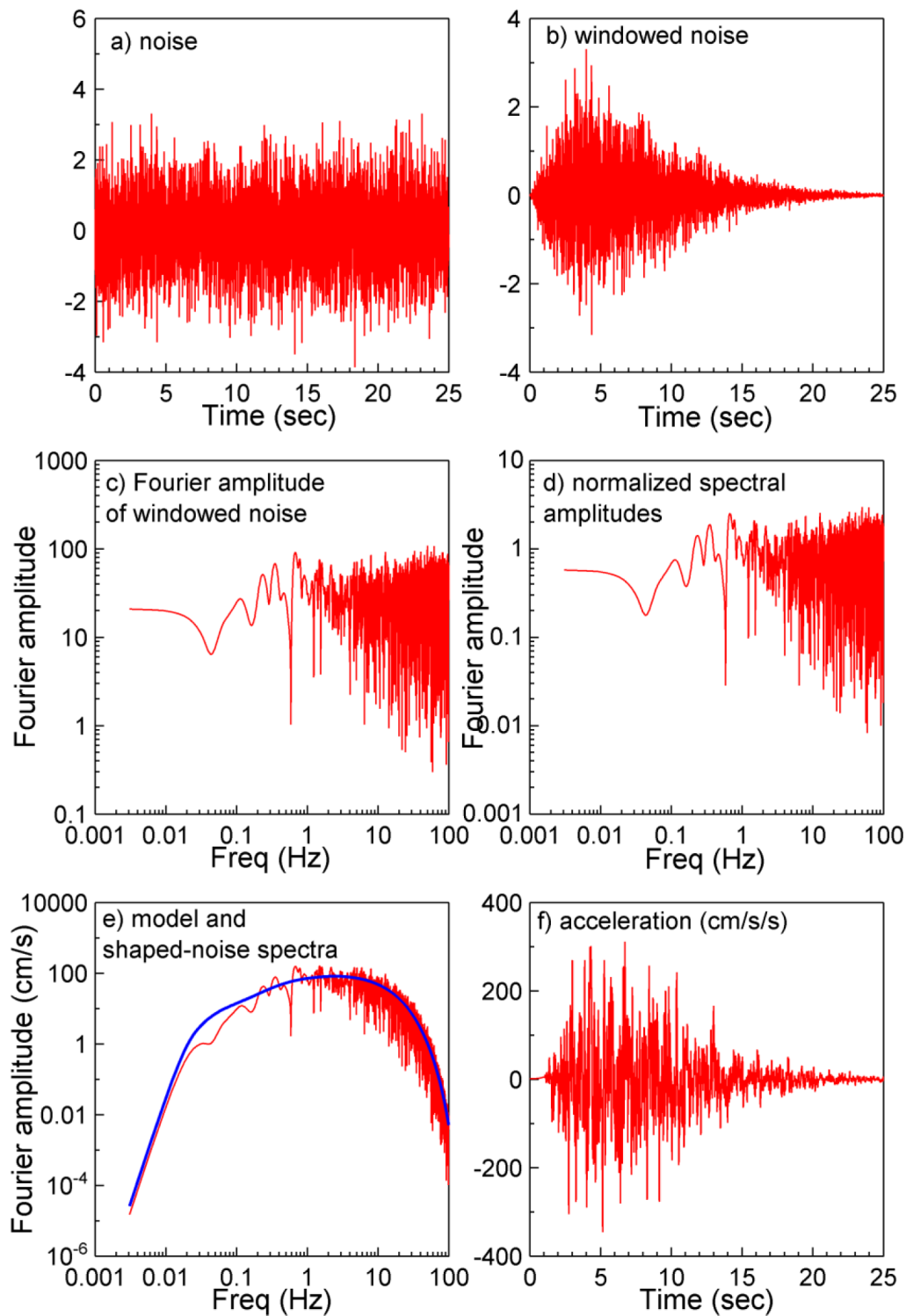
Figure 1.1 Illustration of the steps followed in the stochastic simulation process (courtesy of Boore, 2003)

The overall path effect on amplitude spectrum is divided into two components: geometrical spreading and anelastic attenuation. Geometrical spreading refers to the decay of ground-motion amplitudes due to spreading of seismic-wave energy over a continuously increasing area as a result of expansion of wavefronts. The decay rate of Fourier amplitudes due to geometrical spreading primarily depends on the source-to-site distance (R). Ground motions at close distances are dominated by direct waves, which would spread spherically in a homogeneous whole-space and their amplitudes would attenuate as $R^{-1.0}$. At far distances, however, ground motions are dominated by surface waves which decay as $R^{-0.5}$ due to cylindrical spreading.

Anelastic attenuation expresses the distance-dependent dissipation of seismic energy due to particle interaction that has not been accounted for by the geometrical spreading. It is generally described by a frequency-dependent Quality factor that represents the regional wave-transmission quality of the propagation medium (Lam et al., 2000). The Quality factor and anelastic attenuation are inversely related (i.e., the larger the Quality factor, the less the anelastic attenuation).

The conditions on the recording site have both amplification and attenuation effects on the amplitude spectrum. Seismic waves are amplified as they propagate from the source to the surface due to the impedance variations in the crust and overlying soil column. This amplification is frequency dependent. The site diminution effect represents the distance-independent attenuation of seismic waves within the near surface material as described by the κ_0 parameter of Anderson and Hough (1984). The κ_0 parameter is site dependent and mostly influences the Fourier amplitude spectrum at high frequencies.

1.3   Organization of thesis

The study is presented in five chapters in this thesis. Chapter 1 introduces the work and provides background material relevant to stochastic simulations. Chapter 2 presents discussions on the saturation effects observed in ground motions from moderate-to-large magnitude earthquakes at close distances. We identify the trade-offs between key ground-

motion modeling parameters and investigate the ability of equivalent point-source modeling technique to capture the empirically-observed saturation effects. In Chapter 3, we determine models for the source and attenuation attributes of California earthquakes, which can be incorporated into equivalent point-source simulations to predict average response spectra over wide magnitude and distance ranges. Chapter 4 presents the derivation of the generic GMPE based on the equivalent point-source simulations with parameters calibrated the observed motions in California. As an example application of the generic GMPE, we show how it can be adjusted for use in central and eastern North America. Finally, Chapter 5 lists overall conclusions and suggestions for future work. It is noted that Chapter 2 has been published in *Bull. Seism. Soc. Am* and Chapters 3 and 4 have been submitted for publication in *Bull. Seism. Soc. Am.* (August and November, 2014).

1.4 References

Anderson, J. G., and S. E. Hough (1984). A model for the shape of the Fourier amplitude spectrum of acceleration at high frequencies, *Bull. Seismol. Soc. Am.* **74**, 1969–1993.

Atkinson, G. M., and W. Silva (2000). Stochastic modeling of California ground motions, *Bull. Seismol. Soc. Am.* **90**, 255–274.

Boore, D. M. (2003). Simulation of ground motion using the stochastic method, *Pure and Applied Geophysics*, **160**, 635-376.

Boore, D. M. (2009). Comparing stochastic point-source and finite-source ground motion simulations: SMSIM and EXSIM, *Bull. Seismol. Soc. Am.* **99**, 3202–3216.

Boore, D. M., C. Di Alessandro, and N. A. Abrahamson (2014). A generalization of the double-corner-frequency source spectral model and its use in the SCEC BBP Validation Exercise, *Bull. Seismol. Soc. Am.* **104**, 2387–2398.

Brune, J. N. (1970). Tectonic stress and the spectra of seismic shear waves from earthquakes, *J. Geophys. Res.* **75**, 4997–5009.

Lam, N., J. Wilson, and G. Hutchinson (2000). Generation of synthetic earthquake accelerograms using seismological modeling: a review, *J. Earthq. Eng.* **4**, 321–354.

Motazedian, D., and G. M. Atkinson (2005). Stochastic finite-fault modeling based on a dynamic corner frequency, *Bull. Seismol. Soc. Am.* **95**, 995–1010.

Chapter 2

2 Equivalent point-source modeling of moderate-to-large magnitude earthquakes and associated ground-motion saturation effects[1]

2.1 Introduction

Mitigation of seismic hazard due to moderate-to-large earthquakes requires reliable predictions of the resulting ground motions. From an engineering perspective, simple ground-motion models are the most useful, as they facilitate generic predictions of the salient effects of future potential events in a range of circumstances. However, achieving both simplicity and reliability in ground-motion models is challenging. Ground motions are the product of a complex interaction of source, path and site effects; at close distances (< 20 km) to large events, this includes significant complications due to extended fault rupture effects.

A range of methodologies have been developed to model ground motions from large earthquakes, including empirical regressions (e.g., Abrahamson and Silva, 2008; Boore and Atkinson 2008; Campbell and Bozorgnia, 2008; Chiou and Youngs, 2008) and stochastic and/or deterministic simulations (e.g., Irikura, 1978; Hanks and McGuire, 1981; Boore, 1983; Somerville et al., 1991; Hartzell et al., 1999; Motazedian and Atkinson, 2005; Liu et al., 2006; Frankel, 2009; Graves and Pitarka, 2010). A common observation, as captured in empirical ground-motion prediction equations, is that the magnitude- and distance-scaling of ground motions weakens at close distances for large earthquakes, as illustrated in Figure 2.1. Weakening of the magnitude-scaling of ground motions from large earthquakes is referred to as *magnitude saturation*. Such saturation

---

[1] A version of this chapter has been published. Yenier, E., and G. M. Atkinson (2014). Equivalent point-source modeling of moderate- to-large magnitude earthquakes and associated ground-motion saturation effects, *Bull. Seismol. Soc. Am.* **104**, 1458–1478.

effects become more pronounced with decreasing distance, leading to apparently slower attenuation rates at close distances for large events, in comparison to small events. This is referred to as *distance saturation*. Although the saturation effects are given different names, they are inter-related, and share a common physical basis, in that near-fault ground motions from a large earthquake are primarily controlled by the closest portions of the rupture (discussed in the next section).
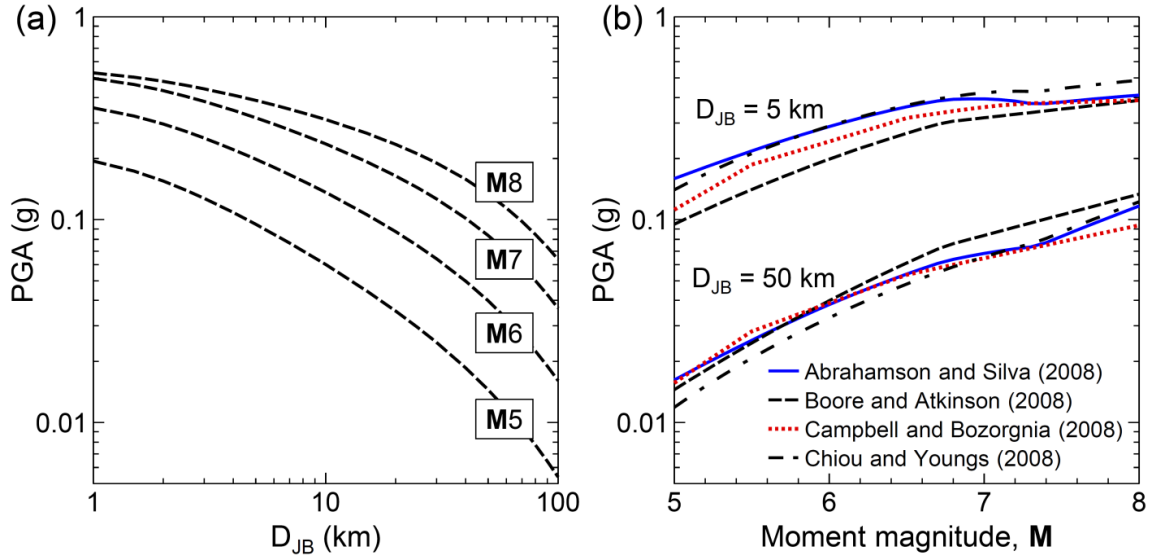
Figure 2.1 An example showing (a) distance- and (b) magnitude-dependent saturation of peak ground acceleration (PGA). Ground motions are empirical predictions as based on the Next Generation Attenuation (NGA) prediction equations (see the legend) for strike-slip faulting with a focal depth of 10 km and $V_{S30} = 760$ m/s. Here, V_{S30} is the travel-time weighted average of shear-wave velocities for the top 30 m of a site and D_{JB} is the closest distance to the surface-projection of fault rupture (a.k.a. Joyner-Boore distance).

Finite-source models can successfully predict the motions from large earthquakes, as they explicitly model the causative physical processes of ground-motion saturation. In general, point-source models are more limited in this respect. Point-source predictions of ground motions monotonically increase with decreasing distance, because the total energy is assumed to be released from a single point. However, previous studies (e.g., Atkinson and Silva, 2000; Boore, 2009) have shown that saturation effects can be simulated in

point-source models by placing the point at an equivalent overall distance, such that close-distance motions attenuate appropriately. This can be achieved by defining the ground-motion attenuation in terms of an effective distance metric rather than an actual distance metric. For example, the effective distance may be given as $R = (D^2 + h^2)^{0.5}$, where D is an actual distance measure (e.g., hypocentral or fault distance) and h is a "pseudo-depth" term that accounts for saturation effects (Atkinson and Silva, 2000). Here, $R \approx D$ at far distances ($D >> h$) whereas $R > D$ at close distances. This method, whereby the motions are considered to emanate from a virtual point, is referred to as *equivalent point-source modeling*.

There are several advantages to modeling motions by an equivalent point source, rather than invoking more detailed extended-fault models – assuming that we can do so without significant loss of ability to accurately describe observed ground motions. First, equivalent point-source models provide a simple basis for development of ground-motion prediction equations (GMPEs) through stochastic methods (e.g. Atkinson and Boore, 1995; Atkinson and Silva, 2000), requiring a minimum of parameters. This is particularly advantageous for GMPE development in data-poor regions such as eastern North America, or to enable simple regional modifications of GMPEs to account for regional differences in source or attenuation attributes. Additionally, the predictions of equivalent point-source models can provide a useful benchmark against which near-fault motions from large earthquakes can be compared, in order to discriminate other extended source effects (e.g., hanging-wall/footwall effects and rupture directivity effects). Finally, equivalent point-source models are a useful tool in seismic hazard analyses for integrating hazard contribution from large events that occur within areal sources, allowing consistent and computationally-efficient representation of distributed seismicity over all magnitudes (Bommer and Akkar, 2012). These advantages motivate this study, which aims to determine the extent to which equivalent point-source models can accurately describe observed ground motions from large earthquakes, including observations at close distances. We develop a simple formula for placement of a point source at an equivalent distance, such that motions can be predicted accurately with the equivalent point-source method over the range of magnitudes and distances of interest to practical engineering applications.

The study methodology is based on empirical modeling of the source and attenuation attributes of well-recorded **M**6+ earthquakes to define an equivalent point-source for each study event. We identify trade-offs between modeling parameters through analysis of Fourier amplitudes for several alternative attenuation models. We select the best-fitting attenuation model for each earthquake by regression analysis, using the residual statistics as a statistical constraint, and the known seismic moment as a physical constraint. We show that equivalent point-source models can successfully predict the average amplitudes of observed ground motions from large earthquakes and replicate the close-distance ground-motion saturation effects. We describe the magnitude dependency of distance-saturation effects observed in Fourier amplitudes. We also compare the apparent source spectrum from the model for each event with theoretical point-source models.

2.2   Origins of ground-motion saturation effects

The significant challenge in modeling extended ruptures with an equivalent point source is to correctly mimic observed ground-motion saturation effects. In a pure point-source model, amplitudes will continue to grow as we get closer and closer to the source. By contrast, for extended faults the observed ground-motion amplitudes become constant (or saturate) as we get sufficiently close to the fault. The commonly-accepted origin of ground-motion saturation effects relates to the fact that the closest portions of the rupture dominate the motions from large earthquakes close to the fault (e.g. Rogers and Perkins, 1996). This idea is routinely employed in standard finite-source modeling methods, in which the rupture surface is divided into a number of subfaults, each of which is treated as a point-source. At distant stations, seismic waves arrive at the observation point with relatively short time delays between the subfaults because they are all at about the same distance from the station (i.e. the observation distance is large relative to the size of the fault). Furthermore, ground motions from each segment are spread out over a long duration of time due to the large travel distances. This increases the chance of having constructive interference between the arrivals from various subfaults (Anderson, 2000). At close distances, only a small portion of the total fault extent is actually close to the observation point, while most of the fault is much further away. Furthermore, signals

from each of the subfaults have short durations, and may be well separated when they arrive at the observation point. This lowers the chance of having constructive interference for stations close to the fault. The net result is that ground motions near a large rupture are primarily controlled by the closest portions of the fault; thus on average the event appears to be smaller and/or the fault appears to be further away.

Considering the processes mentioned above, we can visualize that near-fault stations have a "field of view" and can effectively "see" only the seismic waves radiated within this area in case of a large earthquake, as demonstrated in Figure 2.2. This representation can shed some light on the underlying mechanisms of magnitude-saturation effects seen in empirical data. For a small earthquake (e.g., E_1 in Figure 2.2), seismic waves radiated from the entire rupture contribute to ground motions because the "field of view" of the station is larger than the rupture area; thus, the whole rupture can be "seen" effectively from the observation point. The effective rupture area and the ground-motion amplitudes therefore increase with increasing magnitude. However, once the rupture area exceeds the "field of view" of the station (e.g., E_2 and E_3 in Figure 2.2), ground motions are primarily controlled by seismic waves radiated from the rupture area within the "field of view". This restricts the magnitude-scaling of ground motions at close distances, leading to slower rates of magnitude scaling for large earthquakes compared to small earthquakes. Consequently, we expect ground motions to saturate with magnitude, at close distances. At larger distances, magnitude-saturation effects become less pronounced, because the effective rupture area that controls the ground motions expands with increasing distance. The duration of seismic waves radiated from each subfault increases with distance, leading to a higher chance of having constructive interference between different arrivals, at further stations. This allows seismic waves radiated from a larger rupture area to effectively contribute to ground motions, lessening the magnitude-saturation effect.
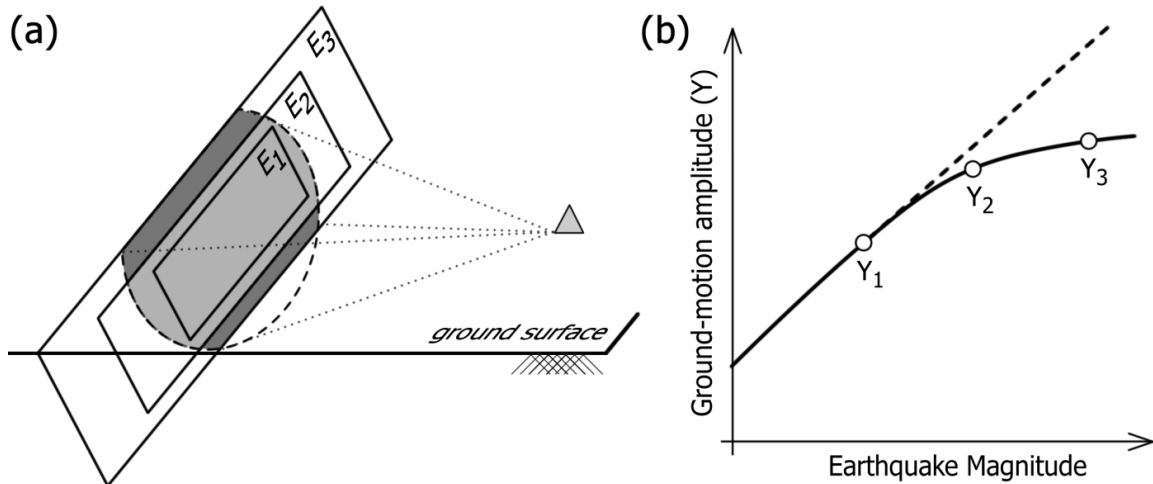
Figure 2.2 Conceptual illustration of saturation of magnitude-scaling of ground motions for large earthquakes. In part (a), the triangle represents a near-fault station and the dashed curve shows its "field of view". Rectangles indicate rupture areas for three earthquakes with different magnitudes: E_1, E_2 and E_3 ($\mathbf{M}_{E1} < \mathbf{M}_{E2} < \mathbf{M}_{E3}$). Rupture areas within the "field of view" designate the effective areas (shaded) that dominate ground motions at the site for earthquakes E_2 and E_3. In part (b), the solid line shows the saturation of magnitude-scaling for ground motions at close distances and open circles show observed amplitudes (Y) at the site, for the three earthquakes. The dashed line indicates constant magnitude-scaling, as would be expected from pure self-similar point-source scaling (i.e. no saturation).

The distance-scaling of ground-motions also saturates at close distances to large earthquakes. There are two typical characteristics of distance-saturation effects: (i) ground-motion amplitudes level off at close distances, and (ii) distance-saturation effects are magnitude-dependent, extending to further distances with increasing magnitude. These effects can be explained by the expansion of effective rupture area with increasing distance. Figure 2.3 illustrates three near-fault stations located at different distances from a large rupture. Ground motions at stations S_1 and S_2 are primarily controlled by seismic radiations from the effective rupture areas designated by A_1 and A_2, respectively. Note that more seismic energy contributes to ground motions at S_2 compared to S_1 because the effective rupture area expands with increasing distance (i.e., $A_2 > A_1$). However, the attenuation effects are stronger for S_2 than that of S_1 due to increased distance. The

increased contribution of seismic waves at S_2 may weaken or cancel out the distance-attenuation effects for S_2, leading to similar ground-motion amplitudes at stations S_1 and S_2 (i.e., $Y_1 \approx Y_2$). This explains the saturation of distance scaling of ground motions and the leveling off of amplitudes at close distances for large earthquakes.
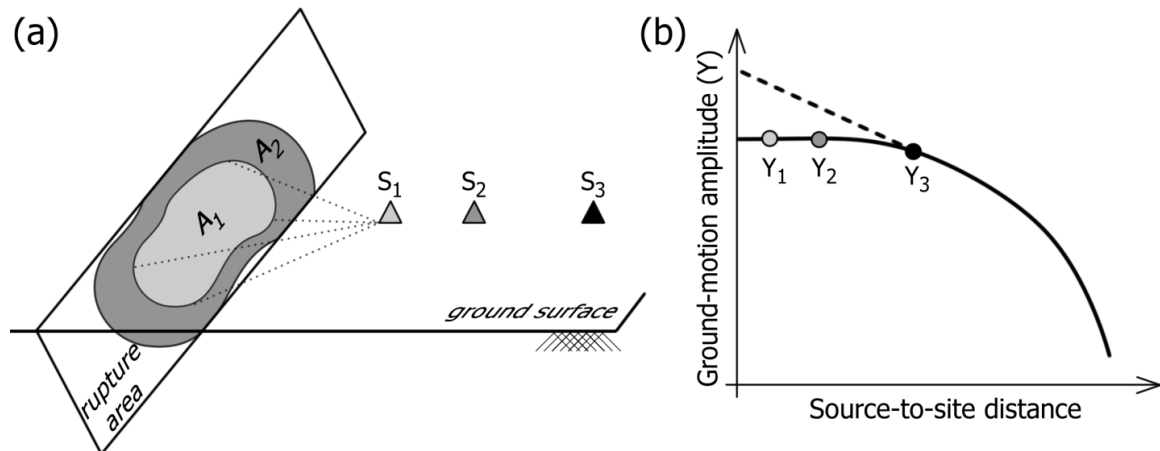
Figure 2.3 Conceptual illustrations of distance-saturation of ground motions for a large earthquake. In part (a), triangles represent near-fault stations and A_1 and A_2 indicate the effective areas of fault rupture that dominate ground motions at stations S_1 and S_2, respectively. Station S_3 is at the minimum distance for which the entire rupture effectively contributes to observed ground motions. In part (b), the solid line shows distance scaling of ground motions incorporating the saturation effects (where Y_1, Y_2 and Y_3 are the amplitudes at stations S_1, S_2 and S_3, respectively) and the dashed line shows the distance scaling that would be expected for a pure point source, with no saturation.

Expansion of the effective rupture area with increasing distance continues until we reach a distance at which the entire rupture can be effectively "seen" from the observation point. This distance (station S_3 in Figure 2.3) is the rationale for the saturation term (h) that we employ in equivalent point-source modeling. At very distant stations (beyond S_3), ground motions are expected to decay steadily with increasing distance, because the effective rupture area has reached the full rupture area. Note that the minimum distance at which the whole rupture area can be seen is magnitude-dependent; a large rupture area can only be seen in its entirety from a large distance. This suggests that the distance-

saturation effects (and hence the saturation term, *h*) should increase with magnitude; this accords with empirical observations, as will be shown (Figure 2.4).

2.3 Data

We selected 11 well-recorded, crustal earthquakes of **M** ≥ 6 that had sufficient numbers of near-fault observations (< 20 km) to model the ground-motion saturation effects at close distances; the study events are listed in Table 2.1. We compiled processed ground motion accelerograms of selected events from publicly available databases such as the PEER-NGA (Pacific Earthquake Engineering Research Center - Next Generation Attenuation) database; see Data and Resources. We visually inspected the Fourier acceleration spectra, as well as the velocity and displacement time-series to determine the reliable frequency range for analysis, for each record. For a few records, we selected more conservative cut-off frequencies than those listed in the original databases; we re-filtered these motions at the selected cut-off frequencies by using an acausal, 4-pole/4-pole, band-pass Butterworth filter. Note that such an assessment was not performed for records obtained from the PEER-NGA database, because those ground motions were processed based on record-by-record visual screening of Fourier spectra and integrated displacement time series (Chiou et al., 2008).

We computed Fourier acceleration spectra within the usable frequency band of the processed ground motions. This was defined as extending from $1.25f_{lc}$ to $f_{hc}/1.25$, where f_{lc} and f_{hc} are the low- and high-cut filter frequencies, respectively. Log(10) Fourier amplitudes were averaged with intervals of 0.1 log frequency units and tabulated at the center of each frequency bin.

Table 2.1 Selected crustal earthquakes and their main seismological parameters

Earthquake*	Date (yyyy/mm/dd)	Latitude (deg)	Longitude (deg)	M	Depth (km)	Faulting Style†	No. of Records
Landers, California	1992/06/28	34.200	-116.430	7.28	7.0	SS	103
Northridge, California	1994/01/17	34.206	-118.554	6.69	17.5	R	159
Parkfield, California	2004/09/28	35.819	-120.371	6.00	8.3	SS	93
Darfield, New Zealand	2010/09/03	-43.615	172.049	7.00	10.9	SS	159
Christchurch-I, New Zealand	2011/02/21	-43.568	172.694	6.30	5.6	RO	127
Christchurch-II, New Zealand	2011/06/13	-43.580	172.740	6.00	9.0	SS	125
Chi-Chi, Taiwan	1999/09/20	23.860	120.800	7.62	6.8	RO	410
Chi-Chi Aftershock, Taiwan	1999/09/20	23.810	120.850	6.20	7.8	R	236
Kocaeli, Turkey	1999/08/17	40.727	29.990	7.51	15.0	SS	31
Duzce, Turkey	1999/11/12	40.775	31.187	7.14	10.0	SS	53
L'Aquila, Italy	2009/04/06	42.334	13.334	6.30	9.0	N	60

*Earthquakes are clustered according to their geographic region, each of which is separated by a horizontal line.
†Faulting Style: N: Normal, R: Reverse, RO: Reverse oblique, SS: Strike-slip

We used vertical-component Fourier amplitudes in the analysis, assuming that site amplifications for vertical ground motions are small enough to neglect; thus vertical motions are taken as a proxy for unamplified horizontal component motions (e.g. Lermo and Chavez-Garcia, 1993). This is consistent with common practice in stochastic simulation studies to develop ground-motion prediction equations; for example, Atkinson and Boore (2006) use the ratio of the horizontal to the vertical component, on rock sites, as an estimate of the crustal amplification effects on the horizontal component. To test our assumption that there are minimal site amplification effects on the vertical component, we compared vertical Fourier accelerations and their attenuation trends for different site conditions, as shown in Figure 2.4. Most of the ground motions were recorded on NEHRP C and D sites, with some records on NEHRP A and B sites (see the caption of Figure 2.4 for site class definitions). In this study, we excluded ground motions recorded at very soft sites (i.e., NEHRP E: $V_{S30} < 180$ m/s). In Figure 2.4, we observe that vertical motions attain similar amplitudes and attenuation trends, regardless

of the site condition, which supports our assumption. It should be acknowledged, however, that there may be some residual regional site effects (including crustal amplification) in the vertical-component motions, and if so these would map into the obtained source amplitudes.

In Figure 2.4, a notable trend is that the distance-scaling of ground motions weakens at close distances, as mentioned earlier. Fourier amplitudes of the **M**7.0 Darfield earthquake saturate at distances < 15 km whereas saturation effects appear to extend out to 30 km for the **M**7.62 Chi-Chi earthquake. Although there are fewer near-fault data from the **M**6.69 Northridge earthquake, ground motion saturation is apparent at distances < 10 km. This suggests that close-distance saturation is magnitude-dependent, extending to further distances as the earthquake size increases. It is noteworthy that other factors such as focal depth and source-to-site azimuth may also have influence on the observed saturation effects at close distances. In this study, we consider observations from all azimuths in order to determine the overall saturation effects in a point-source sense. We model the attenuation attributes of observed motions as a function of the closest distance to the rupture area (D_{rup}), which implicitly considers the rupture depth by definition (see the next section).
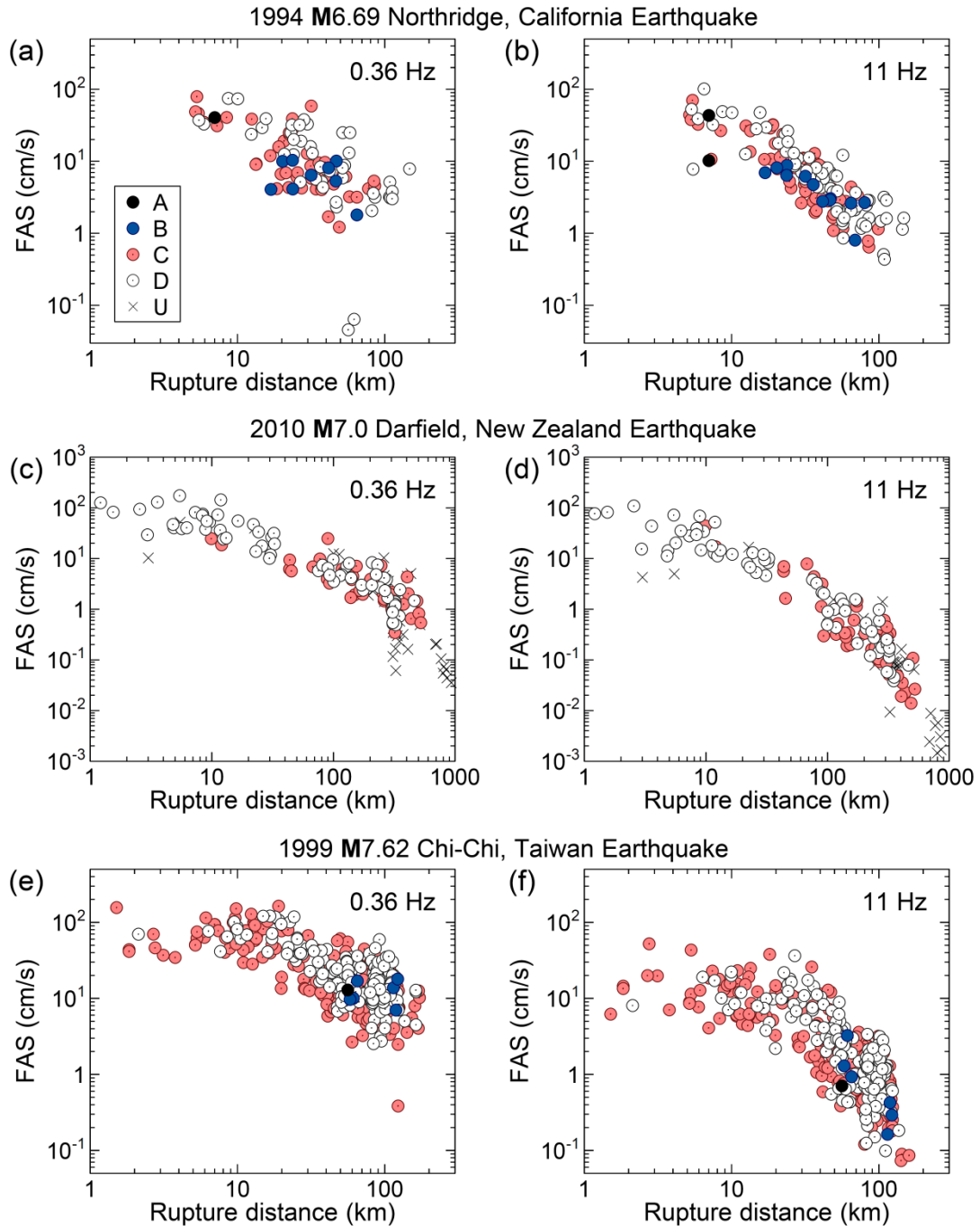
Figure 2.4 Attenuation of vertical Fourier acceleration spectra (FAS) for selected events at frequencies $f = 0.36$ Hz and $f = 11$ Hz. Symbols show motions by NEHRP (National Earthquake Hazards Reduction Program) site classification: A: $V_{S30} > 1500$ m/s, B: 760 m/s $< V_{S30} \leq 1500$ m/s, C: 360 m/s $< V_{S30} \leq 760$ m/s, D: 180 m/s $\leq V_{S30} \leq 360$ m/s and U: unknown (NEHRP, 2000).

2.4   Model and regression analysis

We modeled Fourier amplitudes based on the equivalent-point source approach to characterize the source and attenuation attributes of selected earthquakes. We regressed observed ground motions to fit the following functional form on an earthquake-by-earthquake basis:

$$logA(f,R) = c_1(f) + logZ(R) + c_2(f)R \qquad\qquad (2.1)$$

where A is the Fourier spectral acceleration (vertical component), f is frequency and R is a distance metric. The term c_1 is the product of the source spectrum and high-frequency site effects as modeled by the κ_0 operator of Anderson and Hough (1984), and c_2 is the coefficient of anelastic attenuation. The geometrical attenuation, $Z(R)$, refers to the decay of ground motions due to spreading of seismic-wave energy over an increasing area as a result of expansion of wavefronts. The attenuation rate primarily depends on the source-to-site distance. At close distances, ground motions are dominated by direct waves. Theoretically, direct waves would spread spherically in a whole-space and their amplitudes would attenuate as $R^{-1.0}$. At far distances, however, ground motions are typically dominated by surface waves (and/or trapped phases containing multiple reflections and refractions) which decay as $R^{-0.5}$ due to cylindrical spreading. The transition distance from direct-wave to surface-wave spreading can range from 40 km to 100 km, depending on the focal depth, faulting mechanism and crustal structure (Burger et al. 1987; Ou and Herrmann 1990). In some regions (e.g., eastern North America), the joining of direct waves by post-critical reflections from Moho discontinuity can create a transition zone wherein ground motions show little or no attenuation (Atkinson and Mereu, 1992; Atkinson, 2004), modifying the attenuation pattern at distances between ~70 km and ~150 km.

We examined the attenuation trends of Fourier amplitudes at low frequencies ($f < 0.5$ Hz), for which anelastic attenuation effects are minimized, to assess the general shape of the geometrical attenuation for selected earthquakes. We deduced that ground motions can be adequately modeled by using a piecewise function with two segments, allowing

for a transition from direct-wave to surface-wave spreading. The geometrical attenuation, Z, was formulated as

$$logZ(R) = \begin{cases} b_1 logR & \text{if } R \leq R_1 \\ b_1 logR_1 + b_2 log(R/R_1) & R > R_1 \end{cases} \tag{2.2}$$

Here, R is the effective rupture distance, defined as $R = (D_{rup}^2 + h^2)^{0.5}$, where D_{rup} is the closest distance to the rupture surface and h is a "pseudo-depth" term that accounts for saturation effects. R_1 represents the transition distance and b_1 and b_2 are attenuation rates at $R \leq R_1$ and $R_1 > R$, respectively. As shown in Figure 2.5, this geometrical attenuation form produces a bilinear shape in logarithmic space when there is no close-distance saturation effect ($h = 0$). However, amplitudes roll off to attain a constant value at close distances when saturation effects are considered ($h > 0$).
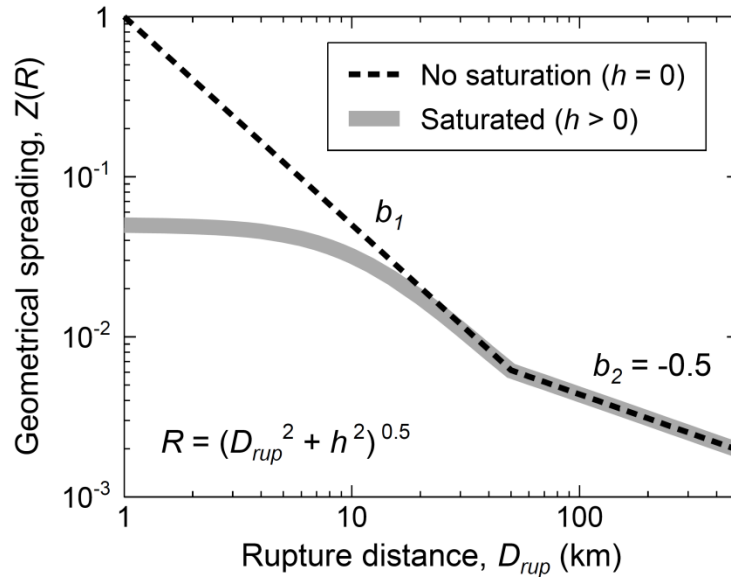
Figure 2.5 Illustration of geometrical attenuation model in terms of rupture distance, plotted for $R_1 = 50$ km, $b_1 = -1.3$ and $b_2 = -0.5$; $h = 10$ km for the saturated model.

We conducted regression analysis for alternative values of the parameters of the geometrical spreading model to find the best-fitting model for each earthquake. For each event, the descriptive parameters of Z were varied in small steps within the following

ranges: R_1: 20 km – 150 km, b_1: (-1.8) – (-1.0) and h: 0 – 50 km. The attenuation rate at far distances (b_2) was fixed at -0.5 based on the theoretical attenuation of surface waves in a half-space (Ou and Herrmann 1990). First, we computed the regression coefficients and residual statistics for all combinations of R_1, b_1 and h. Then, we selected the value of h that best describes the observed saturation effects for each R_1-b_1 combination, based on the mean of the absolute values of residuals, *mean|res|*, where residuals were defined as the logarithmic difference between observed and predicted amplitudes (i.e., *res = $logA_{observed}$ - $logA_{predicted}$*). This exercise results in a set of alternative parameter combinations that describe the observed attenuation trends for each event.

2.5   Trade-offs between modeling parameters

It is well known that attenuation and source parameters trade off against each other in ground-motion modeling, making the separation between such components ambiguous and non-unique (e.g. Atkinson and Mereu, 1992; Boore et al., 2010; Atkinson, 2012). Figure 2.6 shows a typical example of this problem. It compares observed and predicted Fourier accelerations for the **M**7.0 Darfield earthquake. The predictions were determined based on Equation 2.1, using regression coefficients obtained for two different geometrical attenuation models: (i) b_1 = -1.0, R_1 = 50 km and h = 16 km and (ii) b_1 = -1.5, R_1 = 50 km and h = 23.4 km. Both models are in good agreement with the observed ground motions, predicting remarkably similar amplitudes despite having significantly different attenuation parameters.
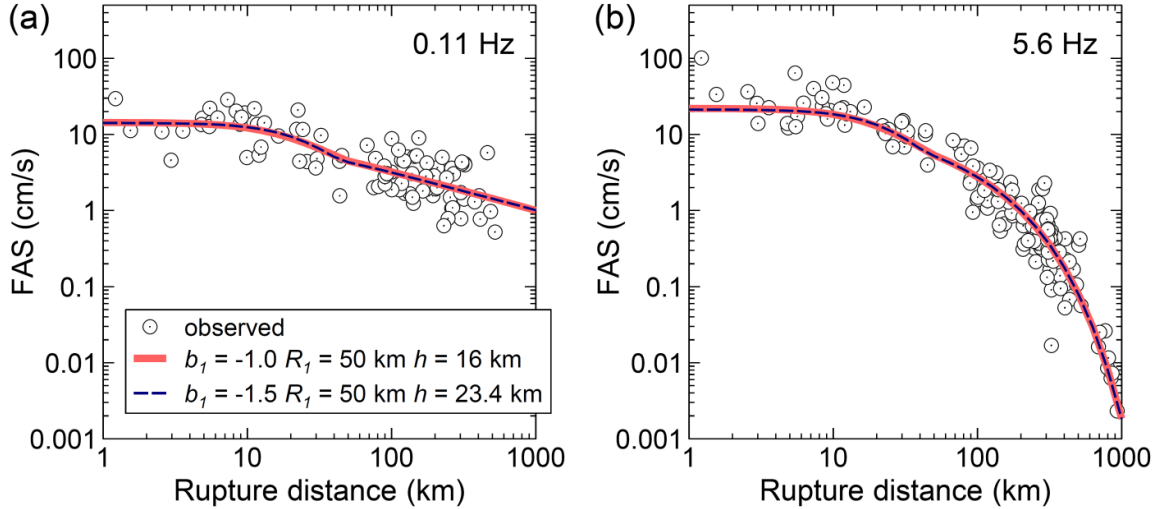
Figure 2.6 Comparison of the observed and predicted Fourier accelerations for the 2010 **M**7.0 Darfield earthquake at frequencies $f = 0.11$ Hz and $f = 5.6$ Hz. Lines represent the predictions based on two different geometrical attenuation models (see the legend).

Trade-off issues also affect our interpretation of apparent source spectra. The apparent source term (c_1) can be considered the combined effects of the source and κ_0:

$$c_1(f) = \log A_0(f) - \frac{\pi \kappa_0}{\ln 10} f \qquad (2.3)$$

where A_0 is the apparent acceleration source spectrum and the second term is the logarithm of the κ_0-effect. Here, κ_0 is the zero-distance value of the decay slope of spectral amplitudes at high frequencies, as described by Anderson and Hough (1984). Equation 2.3 implicitly assumes that a single value of κ_0 applies to all sites recording an earthquake. In other words, it ignores the site-to-site variation of κ_0-effects at high frequencies. Therefore, κ_0 determined from Equation 2.3 can be considered as an average value for vertical motions at all sites, which are mostly NEHRP C and D in our study. It is also possible that there is a source component to our observed κ_0; it is not possible to determine its origin (source vs. site) with our method, only its value.

First, we examined the sensitivity of the value of κ_0 to regression trade-offs. We computed κ_0 from the slope of a trend line fit to c_1 at high frequencies and plotted it as a function of b_1, as shown in Figure 2.7 for the **M**7.0 Darfield earthquake. We calculated

the average of κ_0-factors obtained in this way for all transition distances. It is clear in Figure 2.7 that κ_0 is well defined and relatively insensitive to the choice of geometrical attenuation model. We note that the observed value of $\kappa_0 = 0.023$ s is somewhat lower than typical values of 0.03–0.04 s observed for horizontal-component data (e.g. Anderson and Hough, 1984; Boore and Joyner, 1997; Houtte et al., 2011). This is expected because we are using the vertical component and expect lesser site effects, and therefore lower κ_0.
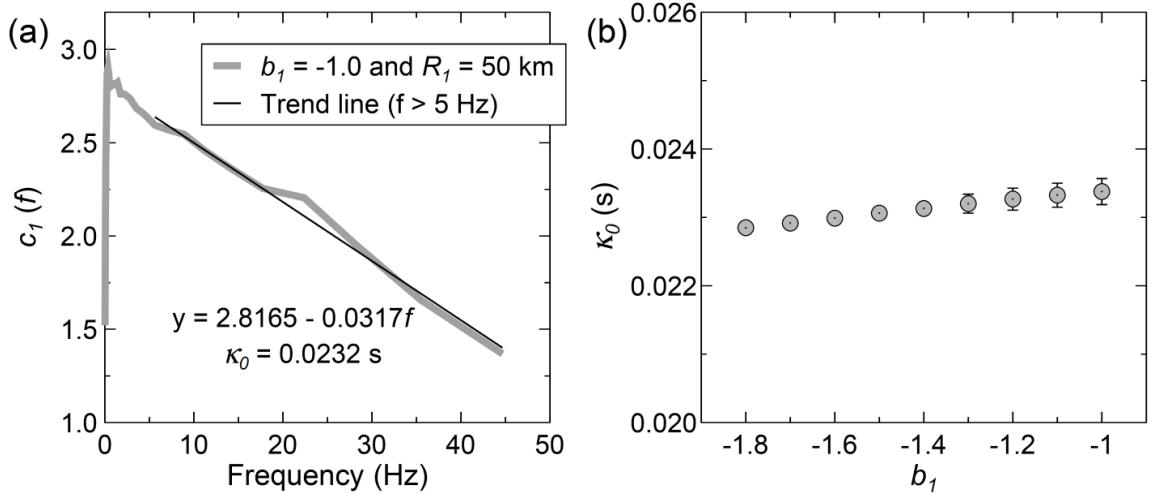
Figure 2.7 (a) Calculation of κ_0 from the source term (c_1) and (b) the trade-off between κ_0 and geometrical attenuation for the 2010 **M**7.0 Darfield earthquake. Symbols are the average of κ_0-factors obtained for all R_1 values and error bars indicate standard deviation ($\pm 1\sigma$) around the mean.

Having obtained κ_0 values, we then determined the apparent source spectra from c_1 by subtracting off the κ_0-effects (Equation 2.3). The apparent source spectrum can be expressed in terms of seismic moment (M_0), stress-drop ($\Delta\sigma$) and corner frequency (f_0) using the simple Brune (1970; 1971) point-source model, which can be written as (Boore, 1983):

$$A_0(f) = CM_0 \frac{(2\pi f)^2}{1 + (f/f_0)^2} \tag{2.4}$$

The scaling constant is $C = R_{\Theta\phi}VF/(4\pi\rho\beta^3)$, where $R_{\Theta\phi}$ is the radiation pattern (= 0.55 on average for shear waves), V is the partitioning of seismic energy onto two horizontal components (= 0.71) and F is the free surface amplification (= 2). ρ and β represent the density and shear-wave velocity in the vicinity of the source, respectively. In this study, we assumed typical values of ρ = 2.8 g/cm^3 and β = 3.5 km/s, for all earthquakes. The crustal parameters, ρ and β, may change depending on the location and depth of the earthquake. In the analysis, we ignored this variation, choosing typical regional crustal properties as proposed in the CRUST 2.0 model for seismogenic depths (see Data and Resources). Note that by using Equation 2.4 we implicitly assume that the Fourier source spectrum determined from the vertical component is equivalent to that of an unamplified random horizontal component (e.g., as in Atkinson and Boore, 2006). The corner frequency (in Hz) is (Boore, 1983):

$$f_0 = 4.9 \times 10^6 \, \beta \, (\Delta\sigma/M_0)^{1/3} \tag{2.5}$$

where $\Delta\sigma$ is the stress drop in bars, M_0 is seismic moment in dyne-cm and β is in km/s. We visually inspected the empirical source spectra to make an initial estimate for f_0. The displacement source spectrum, $D_0(f) = A_0(f)/(2\pi f)^2$, attains relatively constant amplitudes ($D_0 \approx CM_0$) at low frequencies ($f << f_0$). We calculated M_0 from the displacement spectrum using the apparent source spectral amplitudes at frequencies lower than the estimated f_0. We then calculated the actual value of f_0 for the determined moment by matching the Brune model with empirical source accelerations at high frequencies ($f >> f_0$) (Equation 2.4), and thereby obtained the stress drop (Equation 2.5). We compared the actual f_0 and its initial estimate to make sure that parameters (moment and stress) were calculated based on frequencies sufficiently far from f_0.

The dependence of the source parameters on the values of the geometric attenuation parameters R_1 and b_1 is shown in Figure 2.8. There is a strong trade-off between the acceleration source spectrum (A_0) and the value of the geometric spreading coefficient, b_1, as expected (e.g., Boore et al., 2010). The amplitudes that we attribute to the source spectrum increase with increasing steepness of the geometric attenuation slope. Similarly, the values we infer for M_0 and $\Delta\sigma$ also increase with increasing steepness of the

geometric attenuation slope. As discussed in the next section, this places important and useful constraints on the selection of appropriate regression models, because the value of seismic moment is known. Although the amplitude level of the source scales with the geometric spreading coefficient, its shape does not, and thus f_0 is relatively unaffected by the choice of geometrical attenuation model.
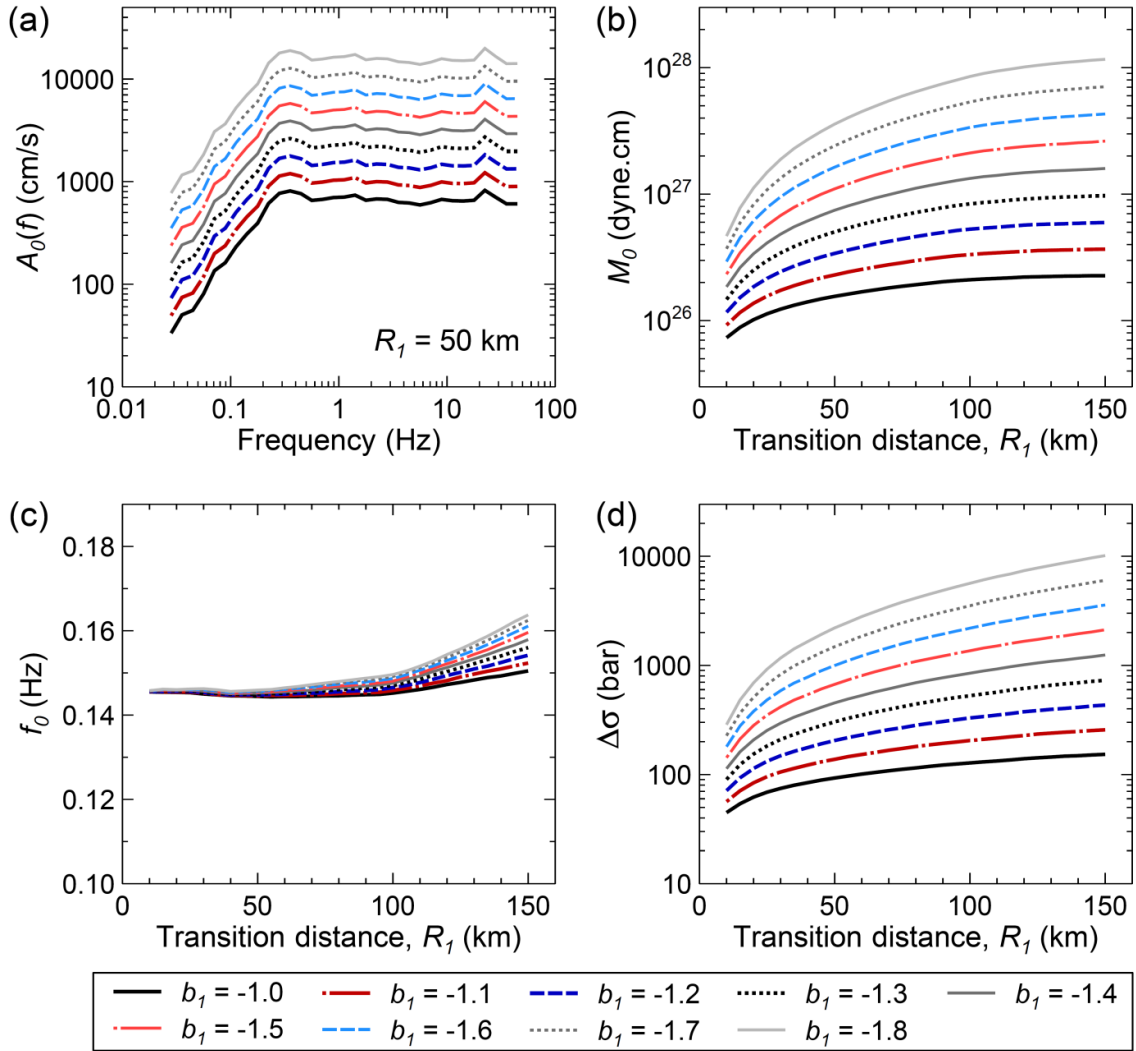
Figure 2.8 Comparison of (a) acceleration source spectra, A_0, (b) seismic moments, M_0, (c) corner frequencies, f_0, and (d) stress-drops, $\Delta\sigma$, obtained for different geometrical attenuation models, for the 2010 **M**7.0 Darfield earthquake.

Finally, we verified that the anelastic attenuation coefficients (c_2) determined for different geometrical attenuation models are insensitive to b_1 and R_1. This was the expected result because c_2 is primarily controlled by ground motions at far distances, where the rate of geometric attenuation is fixed at -0.5 in our model.

2.6 Constraints on geometrical attenuation

In empirical modeling, goodness-of-fit techniques are useful statistical tools for testing the performance of a set of alternative predictive models against observed motions in order to draw a conclusion on the best-fitting model. However, statistical methods alone may not be sufficient. For example, Mahani and Atkinson (2012) tested the ability of various functional forms to describe the ground-motion attenuation in eastern, central and western North America. They concluded that linear, bilinear and trilinear geometrical spreading models all fit the empirical data equally well, and that statistical measures are not very helpful to draw a distinction between the models. This was also illustrated in this study in Figure 2.6, in the context of modeling trade-offs. Moreover, a statistical match between a predictive model and empirical data does not necessarily ensure physically reliable estimates when the model is extrapolated beyond the magnitude-distance range constrained by data.

As shown in the previous section, there is a strong trade-off between geometrical attenuation and the parameters of the source spectrum: M_0 and $\Delta\sigma$. Therefore, comparison of independently-determined values of these parameters with those obtained from empirical regressions can provide a useful constraint on the attenuation model. These constraints can be used in tandem with the regression statistics to define those models that are both physically and statistically plausible. Figure 2.9 shows an example of this process for the **M**7.0 Darfield earthquake. The goodness-of-fit for alternative combinations of the attenuation coefficients is measured by the mean of absolute residuals (*mean|res|*). We use this as the reference statistical metric because it is less sensitive to the outliers than the higher-order averages. We note in Figure 2.9 that the residuals attain a minimum value for a transition distance of $R_1 = $ ~50 km, regardless of the attenuation rate. The residual statistics suggest a preferred value of $b_1 = $ -1.0, but the

goodness-of-fit does not degrade much for other b_1 values. On the other hand, M_0 obtained from the empirical source spectrum depends strongly on b_1, matching the known seismic moment for the Darfield event for $b_1 = -1.2$ and $R_1 = 55$ km. We note that *mean|res|* is also close to its minimum value for this combination. This example illustrates how statistical measures may ensure the selection of the model with minimum misfit but may not satisfy physical constraints on the source parameters. The use of moment as a constraint allows us to reduce ambiguity and non-uniqueness in the regression results.

We repeated the process illustrated in Figure 2.9 for each event in our study. Thus, for each earthquake we determined the combination of geometric spreading rate and transition distance required to match the moment constraint, finding also the best pseudo-depth (h) to model the near-distance saturation effects (for the given combination of b_1 and R_1). Figure 2.10 plots the determined attenuation parameters versus magnitude, distinguishing amongst geographic regions. The inferred transition distance, R_1, varies between 40 km and 60 km, regardless of the magnitude or region. The rate of geometric attenuation is generally steeper than $b_1 = -1.0$. This is in agreement with the findings of other studies. For example, Mahani and Atkinson (2012) found that b_1 ranges between -1.1 and -1.3 for most regions in North America. Allen et al. (2007) indicated that $b_1 = -1.3$ describes the decay of ground-motion amplitudes in southeastern Australia. Theoretical wave propagation studies suggest that direct-wave attenuation rates steeper than $D^{-1.0}$ are expected due to crustal layering and velocity gradients as well as crustal heterogeneities (Ojo and Mereu 1986; Burger et al., 1987; Ou and Herrmann, 1990; Somerville et al., 1990; Chapman and Godbee, 2012). There is some suggestion in Figure 2.10 of regional dependence in geometrical spreading, but the data are insufficient to draw conclusions.
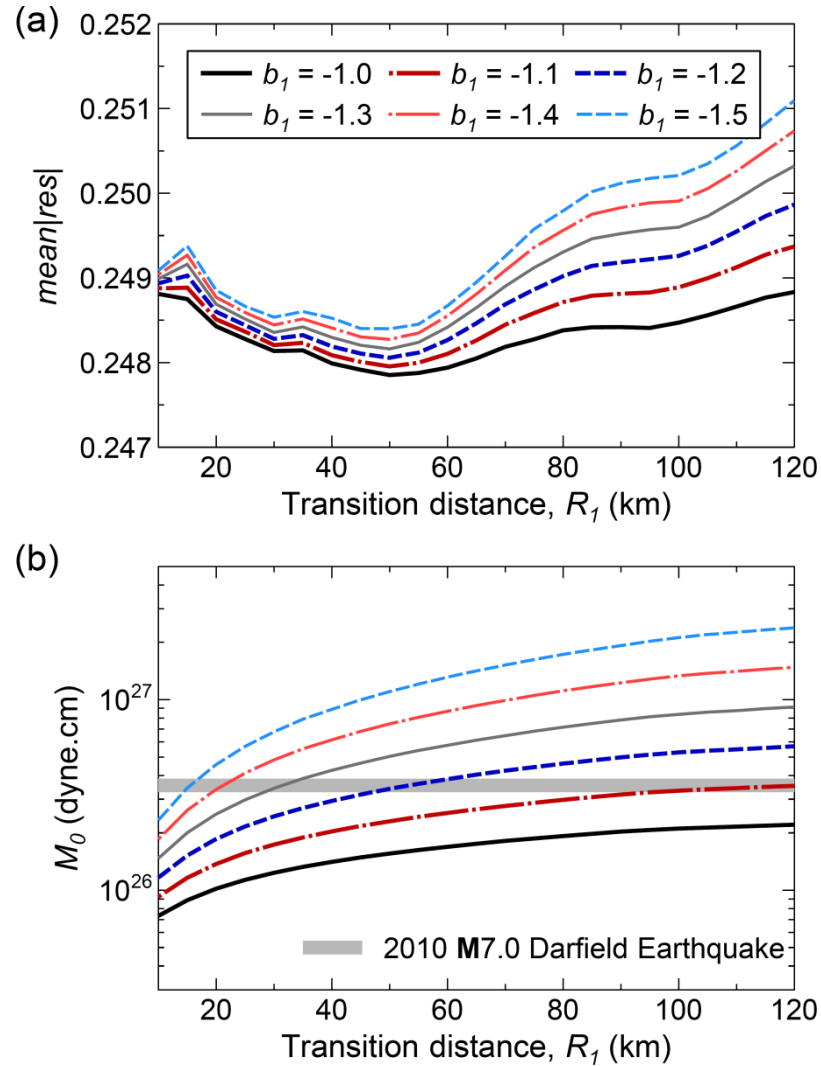
Figure 2.9 Comparison of (a) mean of absolute residuals (*mean|res|*) and (b) seismic moments (M_0) obtained from regressions for different geometrical spreading models, for the 2010 **M**7.0 Darfield earthquake. The thick grey line in part (b) represents the actual seismic moment of the earthquake.

The pseudo-depth term, modeling near-distance ground-motion saturation effects, is magnitude-dependent. As shown in Figure 2.10, for $6.0 \leq \mathbf{M} < 7.0$, ground motions saturate at distances < 20 km. This finding is similar to previous results as reported by Atkinson and Silva (2000) and Halldorsson and Papageorgiou (2005). Our study is able to extend such results to higher magnitudes, due to the inclusion of larger events in the ground-motion database. This reveals that ground-motion saturation effects extend out to

30 km for events of **M** > 7.0. We model the magnitude dependency of the saturation term, based on the values obtained from the study events. The median value of the pseudo-depth is:

$$log(h) = -1.72 + 0.43\mathbf{M} \tag{2.6}$$

Equation 2.6 has a standard deviation of 0.19 in log10 units. It agrees well with the near-source saturation model proposed by Atkinson and Boore (2003), which was derived from ground motions of subduction events for magnitudes up to **M**8.3.
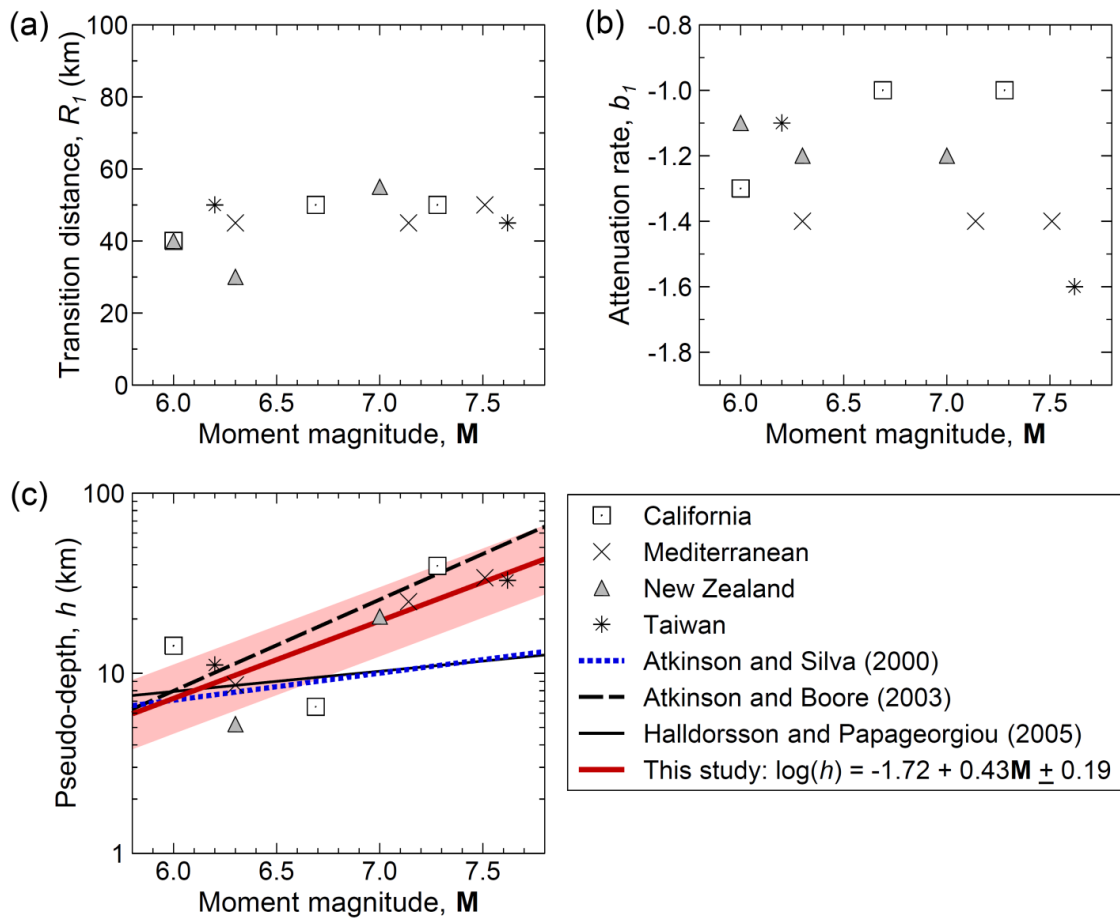
Figure 2.10 Determined values of (a) transition distance, (b) attenuation rate and (c) pseudo-depth by magnitude and region. Shaded area in part (c) represents one standard deviation about the median for pseudo-depth, based on our model.

We should note that no distance-saturation effects were observed for the **M**6.0 Christchurch-II earthquake, and we therefore initially assigned it a value of $h \sim 0$ and did not use the event in deriving Equation 2.6. However, because there were no data within 5 km for this event, any value of $h < 5$ km is essentially equivalent, and we could have fit the data just as well with $h = 3$ km; this is shown explicitly later. Equation 2.6 would predict a larger pseudo-depth, of $h = 7$ km, for an event of this size. Considering the standard deviation of values about Equation 2.6, and the lack of observations that could constrain h values < 5 km, the lack of evidence of saturation effects for this event is not too surprising.

2.7 Anelastic attenuation

We express the anelastic attenuation coefficient through its inverse, the regional quality factor, Q, (e.g., Trifunac, 1976):

$$c_2(f) = -\frac{\pi f}{Q(f)\beta ln10} \leq 0 \tag{2.7}$$

Figure 2.11 shows inferred Q-factors for the study events in comparison to two reference models: (i) $Q = 180f^{0.45}$ for California (Raoof et al., 1999) and (ii) $Q = 117f^{0.77}$ for Taiwan (Chen et al., 1989). Overall, our inferred anelastic attenuation agrees with previous studies for the appropriate region. Moreover, we infer that earthquakes in the Mediterranean have anelastic attenuation similar to California. This is in accord with observations made by other studies that predictive models derived for western North America are applicable to earthquakes in Europe, Mediterranean and the Middle East (Campbell and Bozorgnia, 2006; Stafford et al., 2008; Bommer et al., 2010). There is a suggestion that the anelastic attenuation in New Zealand is significantly different than in California; higher Q in New Zealand at $f > 2$ Hz implies richer high-frequency components relative to California (closer to the Taiwan model).
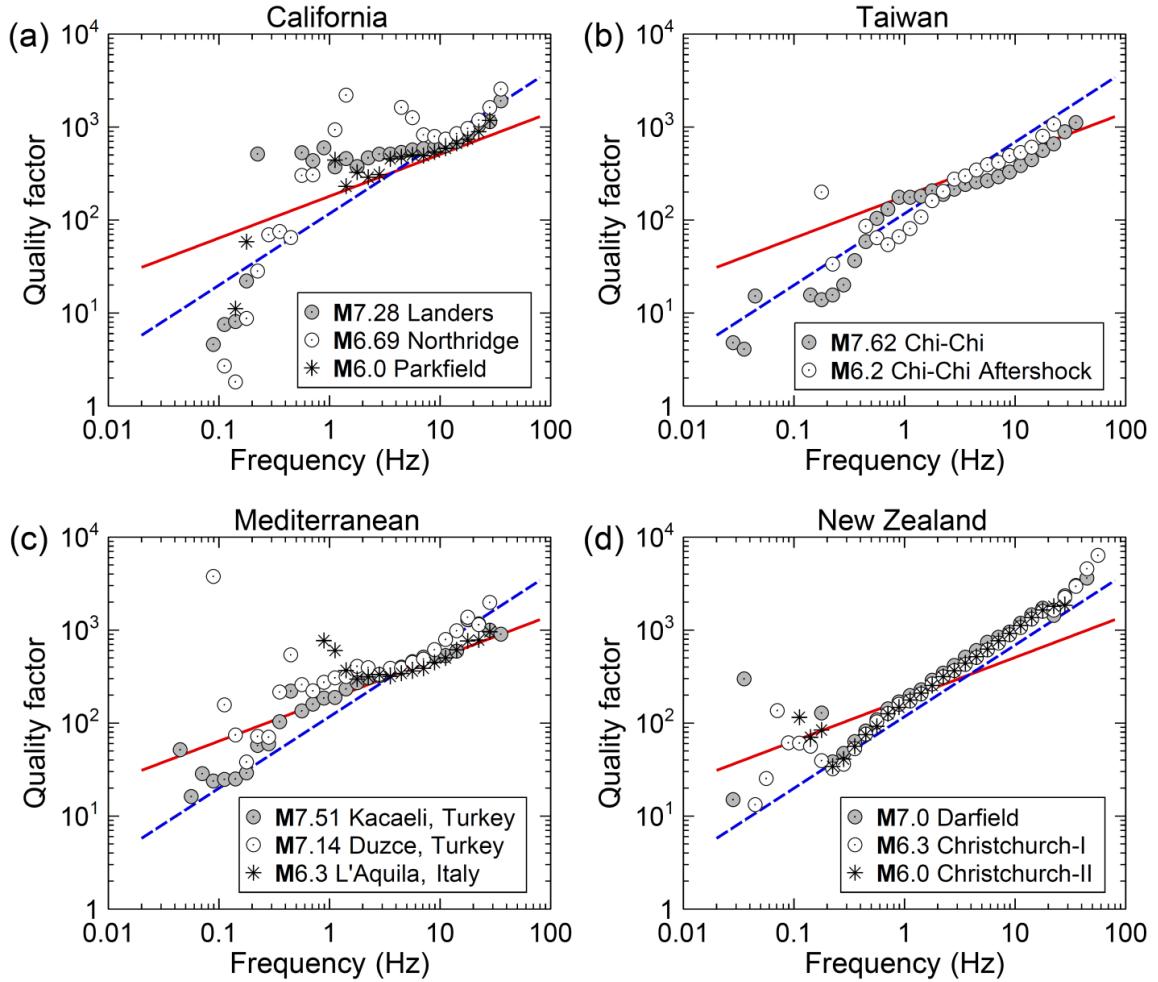
Figure 2.11 Regional comparison of obtained values of Quality factors (symbols). The solid line represents the *Q*-model proposed for California by Raoof et al. (1999), $Q = 180f^{0.45}$. The dashed line displays the *Q*-model proposed for Taiwan by Chen et al. (1989), $Q = 117f^{0.77}$.

2.8   Equivalent point-source spectrum

As described in previous sections, we obtained the apparent source spectrum from the regression analysis at a reference distance of $R = 1$ km. In physical space, R cannot attain a value less than h, by definition. Thus, $R = 1$ represents a virtual point which defines the ground motions that would be projected to the source if there were no saturation effects. It is important to recognize that the equivalent point source is this virtual point, not an actual point on the fault rupture.

The spectra obtained for the equivalent point source ($R = 1$) are shown in Figures 2.12 and 2.13, in comparison to the corresponding Brune-model spectra for the known seismic moments and determined stress drops. Note that the amplitude levels of the equivalent point-source spectra are much greater than the actual observed ground-motion amplitudes at distances close to the fault, which are also shown in the figures. This is due to the near-distance ground-motion saturation effects. Figures 2.12 and 2.13 emphasize the conceptual nature of the equivalent point source, and shows its relationship to actual ground-motion amplitudes, which can be predicted by attenuating the equivalent point-source spectrum to the saturation distance of $R = h$. The maximum ground motions that can be observed correspond to those predicted at $R = h$.

The equivalent point-source spectra in Figures 2.12 and 2.13 agree remarkably well with those predicted by the simple Brune point-source model for all events, with the exception of the **M**7.28 Landers and **M**6.69 Northridge earthquakes. For these two events, the empirical source spectra have significantly lower amplitudes than the predictions of the single-corner Brune model around their corner frequencies. This is the "double-corner" source effect previously reported by Gusev (1983), Boatwright and Choy (1992), and Atkinson and Silva (1997). It may also be noted that the **M**7.62 and **M**6.2 Chi-Chi earthquakes show a "bump" in implied source amplitudes at frequencies near 0.2 Hz. This anomaly has been attributed to the strong surface waves reported at close distances to the fault (Boore, 2001; Furumura et al. 2002; Wang et al., 2006).
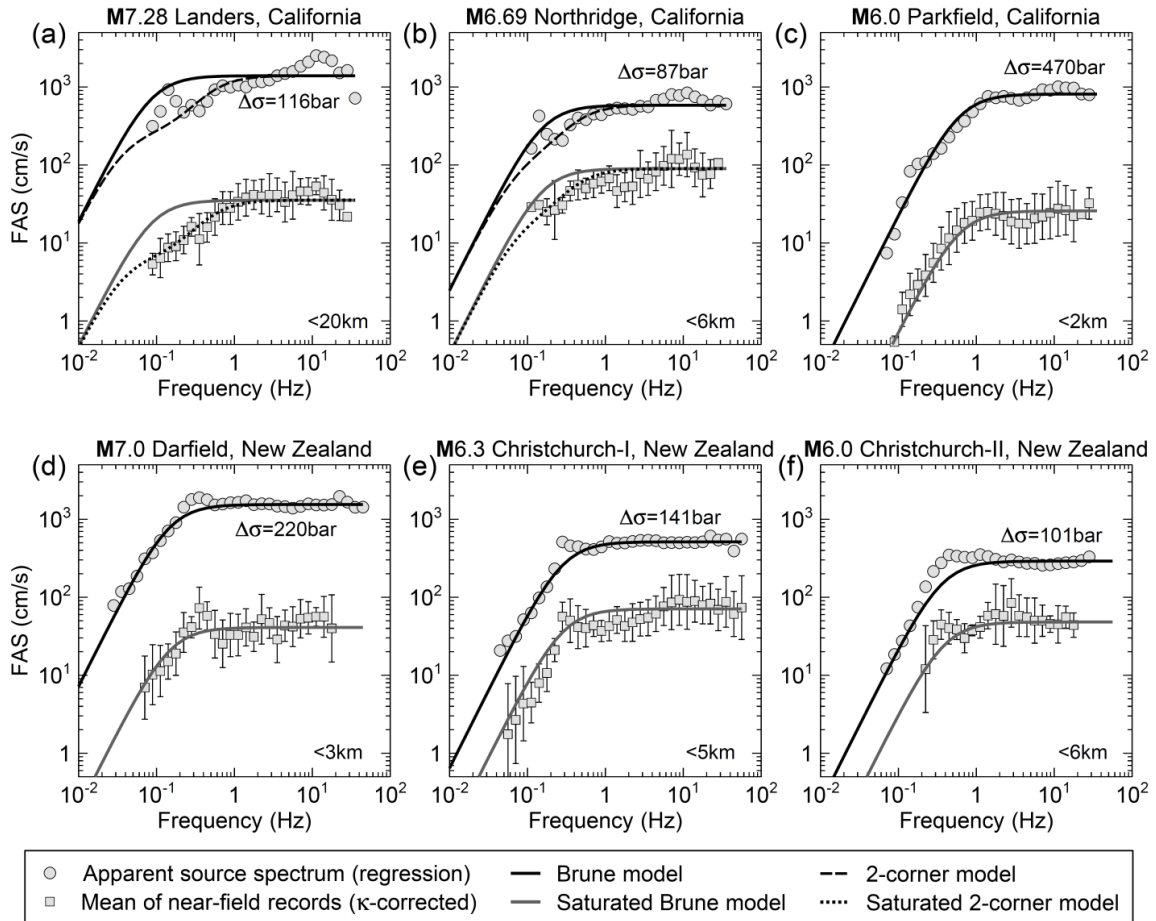
Figure 2.12 Comparison of apparent source spectra with the corresponding predictions of a Brune point-source model for the study earthquakes in California (top row) and New Zealand (bottom row). Solid black lines show Brune-model spectra at $R = 1$ km for the known moment, in comparison to apparent source spectral amplitudes at $R = 1$ from regressions (circles); the inferred stress drop is shown in each plot. Squares show the mean of actual ground-motion amplitudes, after κ_0 correction, for stations at close distances (error bars show one standard deviation about the mean). The maximum rupture distance used for the determination of these mean near-distance spectra is shown at the lower-right corner of each plot. Solid grey lines in parts (a)-(e) show apparent Brune source spectra attenuated to $R = h$. Solid grey line in part (f) indicates apparent Brune source spectrum attenuated to $R = (5^2 + h^2)^{0.5}$ due to lack of near-fault records for the Christchurch-II earthquake; a value of $h = 3$ km was assumed for this event (no observable saturation effect).
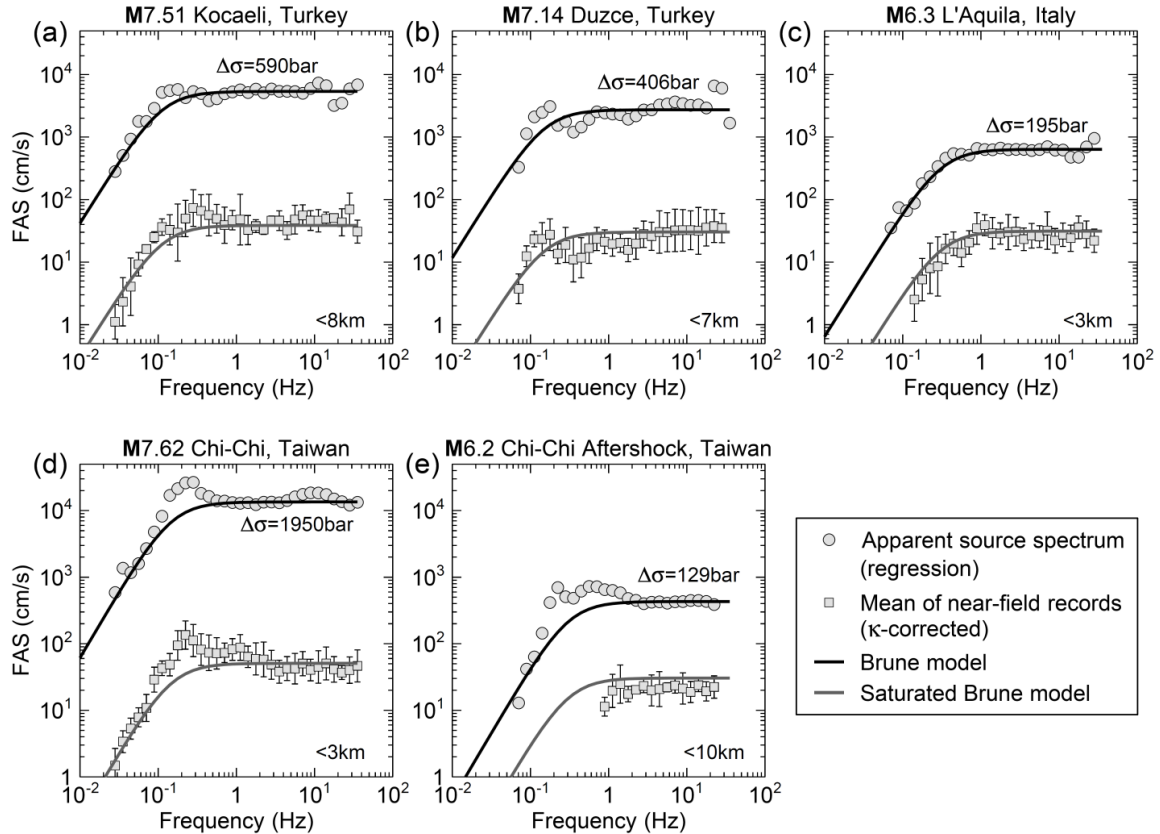
Figure 2.13 Comparison of apparent source spectra with the corresponding predictions of a Brune point-source model for the study earthquakes in Mediterranean (top row) and Taiwan (bottom row). See the caption of Figure 2.12 for the definitions of lines and symbols.

We adopted a modified version of the 2-corner point-source model proposed by Atkinson and Silva (2000) to evaluate the observed spectral sag for the **M**7.28 Landers and **M**6.69 Northridge earthquakes. Their original 2-corner model is characterized by two corner frequencies (f_a and f_b) and a weighting parameter (ε). f_a determines where the spectral sag starts; ε controls the amount of sag and f_b defines the spectral amplitudes at high frequencies. In the original model, all three parameters are determined from magnitude-dependent relationships, such that the high-frequency spectral level corresponds to a fixed Brune stress drop of 80 bars. Boore (personal comm., 2013) modified this model to let the high-frequency level be determined by $\Delta\sigma$. In the revised parameterization suggested by Boore, f_b is defined as

$$f_b = \sqrt{\frac{f_0{}^2 - (1-\varepsilon)f_a{}^2}{\varepsilon}} \qquad (2.8)$$

Here, f_a is as obtained from the original model of Atkinson and Silva (2000), f_0 is the Brune corner frequency (Equation 2.5) and ε is determined by matching the empirical and theoretical source spectra at intermediate frequencies. Equation 2.8 ensures that the modified 2-corner model and Brune model will attain the same high-frequency amplitudes for a specified value of $\Delta\sigma$ (or corner frequency). We found $\Delta\sigma = 116$ bar; $\varepsilon = 0.027$ and $\Delta\sigma = 87$ bar; $\varepsilon = 0.113$ for **M**7.28 Landers and **M**6.69 Northridge earthquakes, respectively. This 2-corner model successfully predicts the source amplitudes at intermediate frequencies, for both earthquakes, as shown in Figure 2.12.

There are important implications of the differences observed in Figures 2.12 and 2.13 between the Brune spectrum for the known moment and the actual ground-motion amplitudes near the fault. Stations near the rupture surface of a large earthquake "feel" the ground shaking as if it was generated by a smaller event. The apparent moment magnitude (**M$_a$**), that represents the effective size of the fault rupture as seen by stations at close distances, can be determined for each earthquake based on the low-frequency spectral displacements of the saturated Brune model (the grey lines in Figures 2.12 and 2.13, evaluated at $R = h$). As shown on Figure 2.14, this apparent magnitude is significantly smaller than the actual moment magnitude for all events except the **M**6.0 Christchurch-II earthquake, for which no saturation distance could be determined ($h = 0$ to 3 km). The discrepancy between the apparent and actual magnitudes (i.e., the vertical lines in Figure 2.14) increases with earthquake size. All events of **M** > 6.5 attain relatively constant apparent magnitudes of ~**M$_a$**6.0. In other words, events attain similar amplitudes at distances close to the fault, regardless of the fault size. This acts to limit near-fault ground-motion amplitudes at low frequencies to a constant value. For example, the close-distance Fourier amplitudes of earthquakes shown in Figure 2.4 generally attain values of ~50–100 cm/s at low-frequencies, regardless of the magnitude. Interestingly, the high-frequency amplitudes are not as tightly constrained. The close-distance stations see only a portion of the fault but that portion could be characterized by a high stress

drop, and thus produce strong motions at higher frequencies. This concept is illustrated in Figure 2.14, which plots the stress drop values inferred from the saturated spectrum for each event (as calculated assuming a moment based on its apparent magnitude). In addition to stress drop, variations in κ_0- and Q-factors can also cause differences in high-frequency spectral amplitudes between the study events.
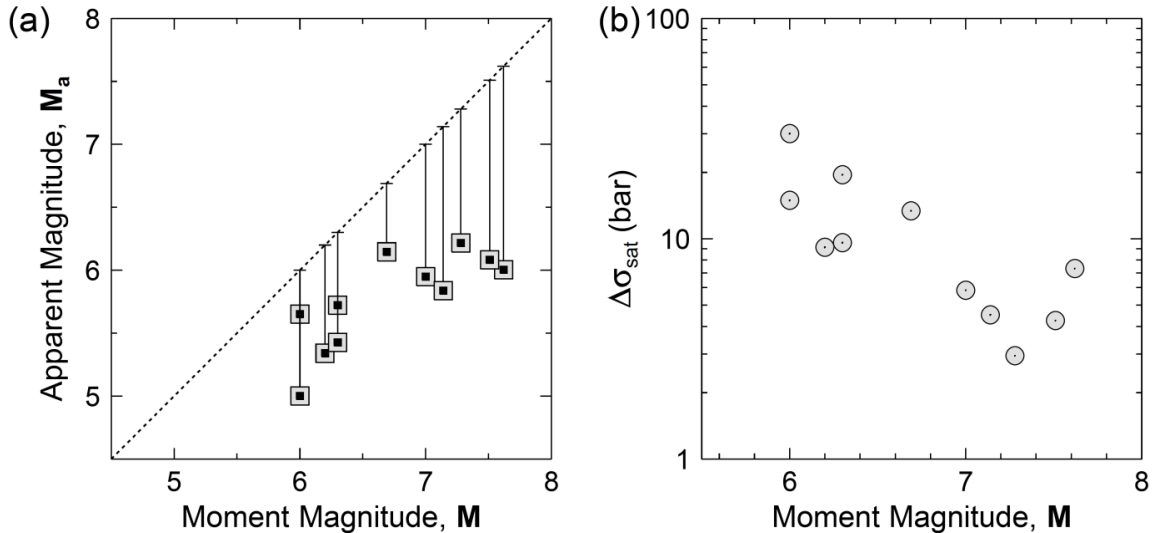
Figure 2.14 (a) Apparent magnitudes, $\mathbf{M_a}$, and (b) corresponding stress drops, $\Delta\sigma_{sat}$, obtained from saturated source spectra ($R = h$), in comparison to the actual moment magnitudes. The dotted line represents $\mathbf{M_a} = \mathbf{M}$ and vertical lines show the amount of deviation of $\mathbf{M_a}$ from $\mathbf{M}$. For the M6.0 Christchurch-II earthquake, we assumed $h = 3$ km. $\mathbf{M_a} = \mathbf{M}6.0$ and $\Delta\sigma_{sat} = \Delta\sigma = 101$ bar if no saturation (i.e., $h = 0$) is assumed for this event.

The stress drop of the Brune model is an important parameter because it controls the strength of high-frequency ground motions in point-source modeling. Figure 2.15 plots the stress drops ($\Delta\sigma$) determined from the apparent equivalent point-source spectra (at $R = 1$) for the study events. $\Delta\sigma$ values are high, ranging between 80 bars and 500 bars for most of the earthquakes, and attaining a value of 1950 bars for the $\mathbf{M}7.62$ Chi-Chi earthquake. Such a high value for Chi-Chi event may sound "odd", knowing that previous studies have suggested values of ~50–100 bars for the same event (e.g.,

Roumelioti and Beresnev, 2003; Liu et al., 2012). The reason for this discrepancy is the strong trade-off between $\Delta\sigma$ and the adopted value of b_1, as illustrated in Figure 2.15. The strong correlation between the values of stress and geometric spreading means that the stress drop cannot be compared across events or studies without referencing the associated geometric spreading (see also Boore et al., 2010).
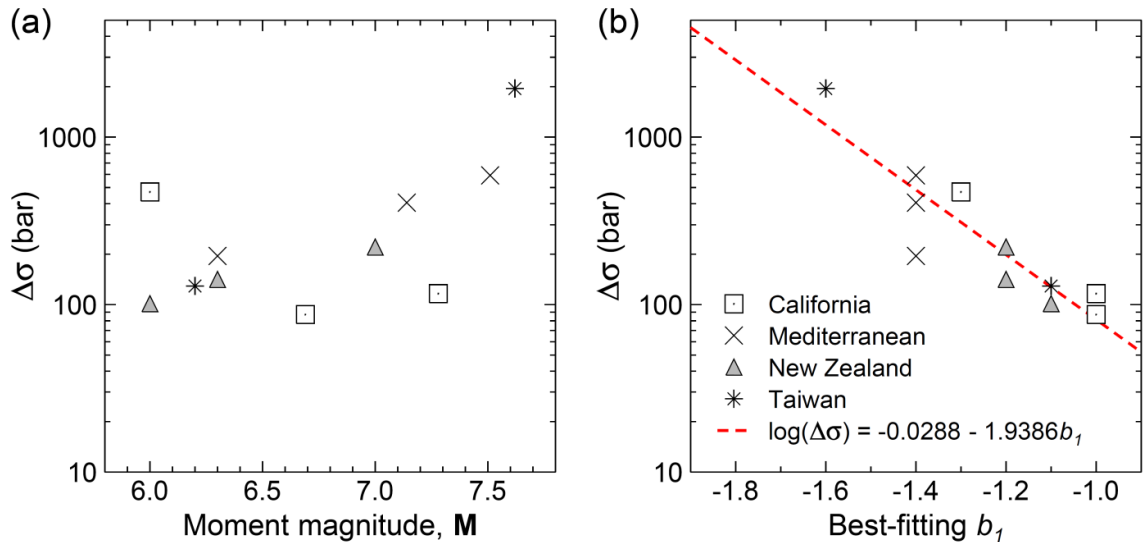
Figure 2.15 Stress drops for equivalent point-source spectra depicted as a function of (a) magnitude and (b) the best-fitting attenuation rate. Symbols represent different geographic regions.

A standard geometric attenuation rate assumed in many previous studies has been $b_1 = -1.0$, based on direct-wave spreading in a whole space. In this study, we have shown that the geometric attenuation rate of $b_1 = -1.0$ does not satisfy the seismic moment constraint for most events, and have thereby determined steeper values of b_1, implying larger stress drops. Note that the near-distance ground motions are the same regardless, as the apparent source spectrum is attenuated through the effective distance concept. This suggests that we could calculate the corresponding stress drops that would have been obtained for the common $b_1 = -1.0$ value, in order to allow consistent comparisons across different events and studies. By using the slope of a trend line fit to the dependence of $\Delta\sigma$ on the adopted b_1 (Figure 2.15), we corrected all stress parameters to the equivalent

values that would be obtained for b_1 = -1.0. The b_1-corrected stress parameter is given by $log\Delta\sigma_{-1.0} = log\Delta\sigma + 1.9386(b_1 + 1.0)$, where $b_1 \leq$ -1.0. The equivalent stress drops for the standard b_1 = -1.0 spreading rate, $\Delta\sigma_{-1.0}$, are shown in Figure 2.16. These values are remarkably less scattered compared to the original model values. The log-average stress drop for a fixed b_1 = -1.0 is 81 bars with a standard deviation of a factor of 1.5. For comparison, we also show the corresponding stress drops for a fixed geometric spreading rate of b_1 = -1.3 ($\Delta\sigma_{-1.3}$) obtained in analogous fashion; these stresses have the log-averaged value of 310 bars. Figure 2.17 shows the obtained values of κ_0, which are mostly in the range of 0.02 s to 0.04 s. Table 2.2 lists the descriptive source and attenuation parameters for the earthquakes studied.
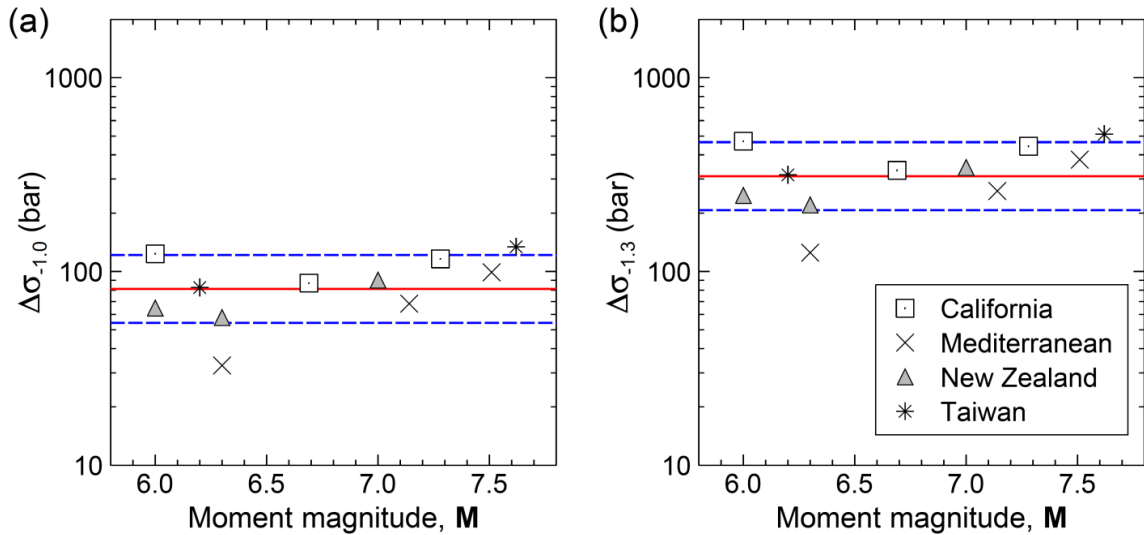
Figure 2.16 Equivalent Brune stress drops for specified geometric spreading rate of (a) b_1 = -1.0 and (b) b_1 = -1.3. Solid line represents the log-averaged stress drop and dash lines show its 16% and 84% percentiles.
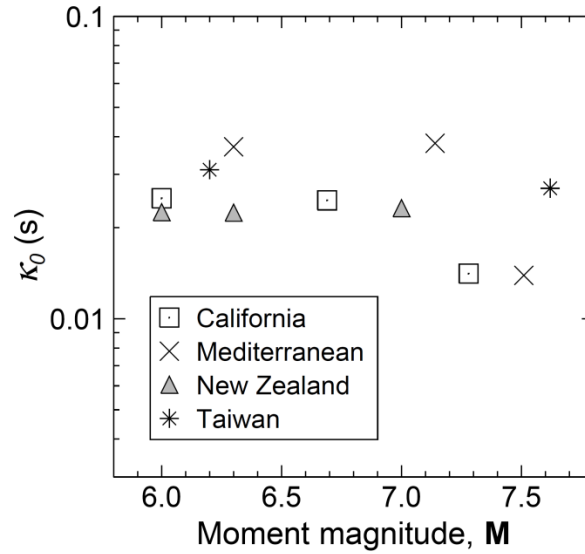
Figure 2.17 Comparison of κ_0-factors in terms of magnitude and geographic region.

Table 2.2 The equivalent point-source modeling parameters of the selected earthquakes

Earthquake	M	b_1	b_2	R_1 (km)	h (km)	$\Delta\sigma$ (bar)	$\Delta\sigma_{-1.0}$* (bar)	κ_0 (s)	M_a
Landers, California	7.28	-1.0	-0.5	50	39.4	116	116	0.0141	6.22
Northridge, California	6.69	-1.0	-0.5	50	6.5	87	87	0.0246	6.14
Parkfield, California	6.00	-1.3	-0.5	40	14.2	470	123.2	0.0250	5.00
Darfield, New Zealand	7.00	-1.2	-0.5	55	20.6	220	90.1	0.0232	5.95
Christchurch-I, New Zealand	6.30	-1.2	-0.5	30	5.2	141	57.7	0.0224	5.72
Christchurch-II, New Zealand	6.00	-1.1	-0.5	40	0-3	101	64.6	0.0225	6.00-5.65
Chi-Chi, Taiwan	7.62	-1.6	-0.5	45	32.8	1950	133.9	0.0270	6.00
Chi-Chi Aftershock, Taiwan	6.20	-1.1	-0.5	50	11.1	129	82.6	0.0311	5.34
Kocaeli, Turkey	7.51	-1.4	-0.5	50	33.9	590	98.9	0.0139	6.08
Duzce, Turkey	7.14	-1.4	-0.5	45	24.9	406	68.1	0.0380	5.84
L'Aquila, Italy	6.30	-1.4	-0.5	45	8.6	195	32.7	0.0370	5.43

* The b_1-corrected stress parameters ($\Delta\sigma_{-1.0}$) are presented only for comparative purposes. Source spectra were determined using the actual seismic moments and $\Delta\sigma$ values.

2.9 Adequacy of the equivalent point-source models

Best-fit Model

We inspected the residuals of Fourier amplitudes (vertical component) calculated based on the equivalent point-source model to evaluate its ability to describe the ground motions of large earthquakes over a range of distances from near-fault to regional (under the assumption that the model parameters are known). The predictions were determined using (Boore, 1983; 2003):

$$A(M_0, R, f) = A_0(M_0, \Delta\sigma, f)Z(R)exp\left(-\frac{\pi f R}{Q(f)\beta}\right)exp(-\pi\kappa_0 f) \qquad (2.9)$$

where the acceleration source spectrum (A_0), geometrical spreading (Z) and κ_0 values were assigned based on the parameters listed in Table 2.2 for the best-fit equivalent point-source model for each event. We adopted the Brune model to calculate the acceleration source spectra (A_0) for all earthquakes, except the **M**7.28 Landers and **M**6.69 Northridge events. For these two events, we used the modified 2-corner model of Atkinson and Silva (2000) with parameters as determined for each event in the previous section. The anelastic attenuation was defined based on the empirical Q values determined for each event.

Figure 2.18 summarizes the residuals versus rupture distance for the predicted Fourier accelerations, for three different frequency ranges: low ($f < 0.1$ Hz), intermediate (0.1 Hz $< f < 1$ Hz) and high frequencies ($f > 1$ Hz). The mean residuals are close to zero over a wide distance range, including distances close to the fault (< 20 km). This observation is valid for all frequency ranges, including low frequencies. This is due to the fact that the M_0-constraint was applied to select the best-fitting attenuation model for each earthquake. We note that mean residuals for 0.1 Hz $< f < 1$ Hz are slightly greater than zero due to the discrepancies observed between the Brune model and apparent source spectra at intermediate frequencies, in Figures 2.12 and 2.13. We observed no discernible distance-dependent residual trends, not even at close distances. This indicates that an equivalent point source can replicate observed ground motions accurately on average, including their distance-saturation effects, provided that the basic source and attenuation parameters are
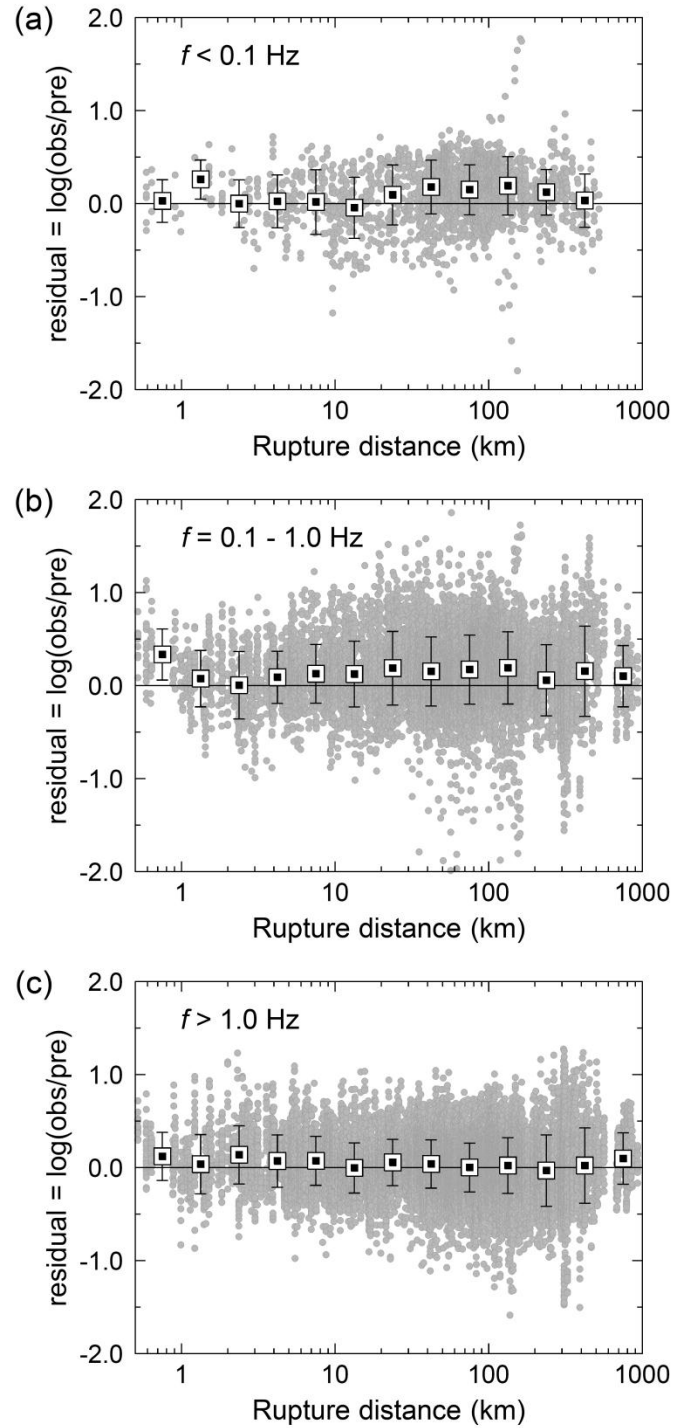
Figure 2.18 Residuals for Fourier amplitude predictions at (a) low (b) intermediate and (c) high frequencies based on the equivalent point-source model, for all study events. Squares indicate the mean residuals computed in logarithmically-spaced distance bins; error bars represent standard deviation about the mean.

known. Residuals of individual ground motions are mostly scattered within a residual band of ±0.3 log units, suggesting that ground motions show a typical variation of factor of 2 (intra-event variability). Figure 2.19 shows the distance-dependent variation of residuals subdivided by geographic regions, at an example frequency of $f = 1.1$ Hz.
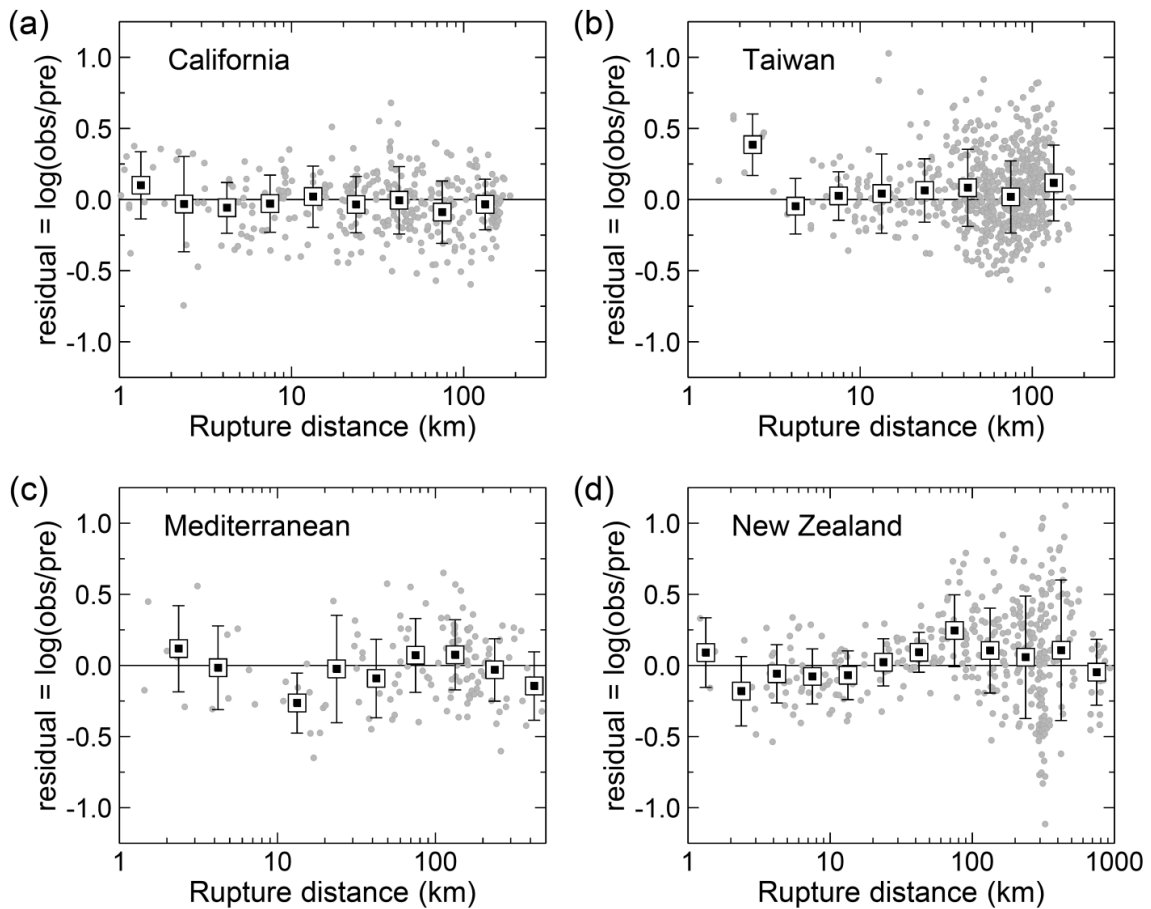
Figure 2.19 Residuals for Fourier amplitude predictions at $f = 1.1$ Hz, based on the equivalent point-source model, for different geographic regions. Squares indicate the mean residuals computed in logarithmically-spaced distance bins; error bars represent standard deviation about the mean.

Classic $R^{-1.0}$ Model

The comparison of low-frequency spectral amplitudes imposed by the known seismic moment and the apparent source spectrum obtained from regressions strongly suggests that an attenuation rate at steeper than $b_1 = -1.0$ is required for most of the study events to match the moment constraint when a bilinear geometrical spreading model is adopted. However, this leads to associated high apparent stress drops at the source, with the implication of strong near-distance saturation. Thus we pose the question: what if we assume the simple $R^{-1.0}$ model over all distances (linear rather bilinear attenuation)? We examine the degree to which we could fit the ground motion amplitudes assuming the simple $b = -1.0$ model over all distances.

Within this context, we repeated regressions to fit the functional form given in Equation 2.1, assuming a linear geometrical attenuation of $Z = R^{-1.0}$. We re-calculated the associated source and attenuation parameters (i.e., $\Delta\sigma$, κ_0 and Q), as well as the saturation term (h), as described in the previous sections. We did not consider the agreement of the actual M_0 with the moment obtained from regression for the linear model, because the attenuation rate is fixed at $b = -1.0$. Figure 2.20 compares the best-fitting modeling parameters obtained for the linear and bilinear geometrical attenuation. The stress drops determined for the linear model are smaller than those obtained for the bilinear model due to the trade-off between b_1 and $\Delta\sigma$. The values of h and κ_0 determined for the linear model are similar to those obtained for the bilinear model. However, the Q-values obtained for the linear model are larger than those obtained for the bilinear model. This is due to the trade-off between anelastic attenuation and the geometric spreading rate at large distances; the assumed spreading at regional distance decreases from -0.5 to -1.0 when the geometrical attenuation is switched from the bilinear to the linear form.
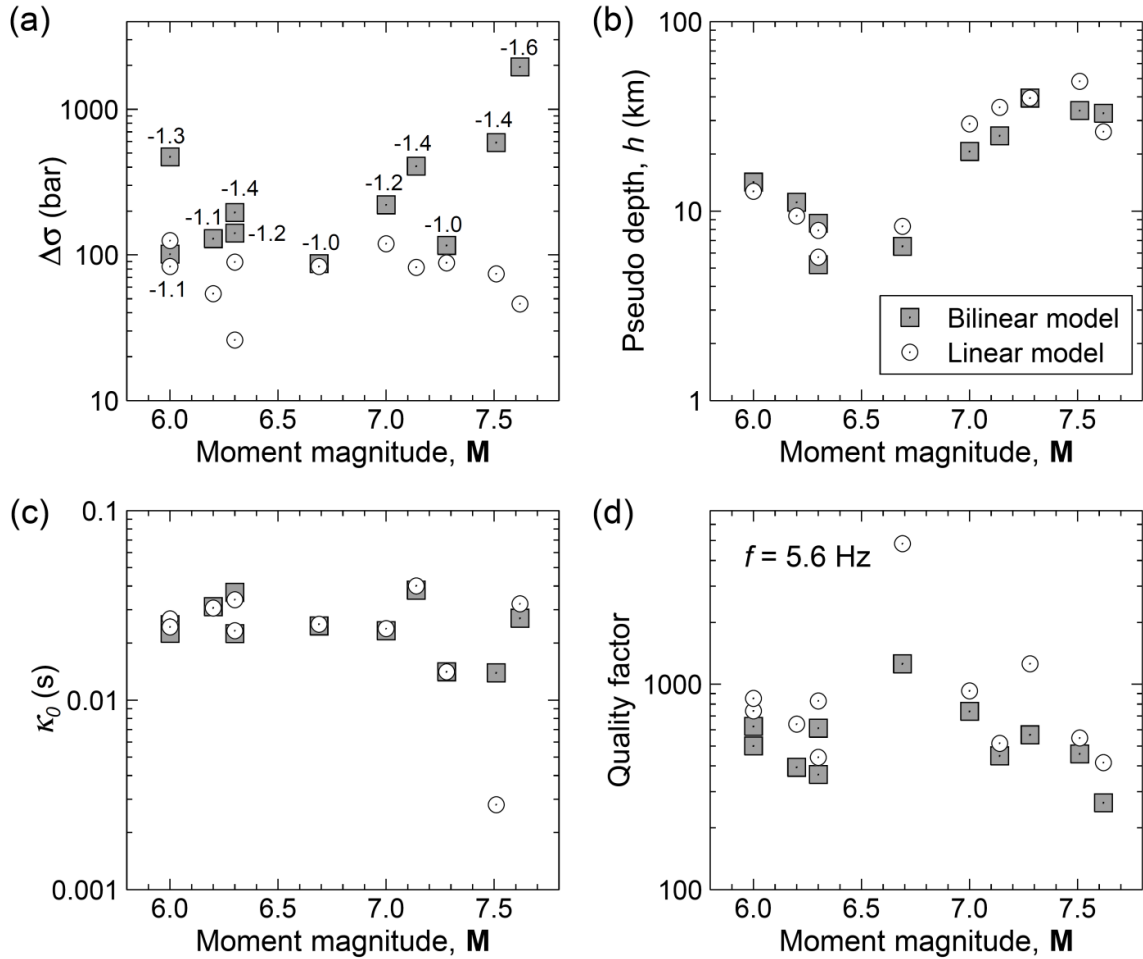
Figure 2.20 The best-fitting modeling parameters obtained for the linear and bilinear geometrical attenuation. Values shown in part (a) represent the best-fitting b_1 for the bilinear model.

Figure 2.21 shows the residuals for the Fourier amplitudes predicted based on the best-fit linear geometrical attenuation model ($R^{-1.0}$), for each event. The linear model performs as well as the bilinear model at frequencies $f > 0.1$ Hz. Mean residuals attain values near zero over a wide distance range, including at close distances to the fault. However, the linear model attains negative mean residuals for $f < 0.1$ Hz, suggesting that its performance is poor compared to the bilinear model at low frequencies. This is due to the fact that the Brune model (as determined based on the actual moment) attains larger amplitudes than the apparent source spectra obtained for the $R^{-1.0}$ model at low frequencies. In other words, the $R^{-1.0}$ model is inconsistent with the moment constraint.
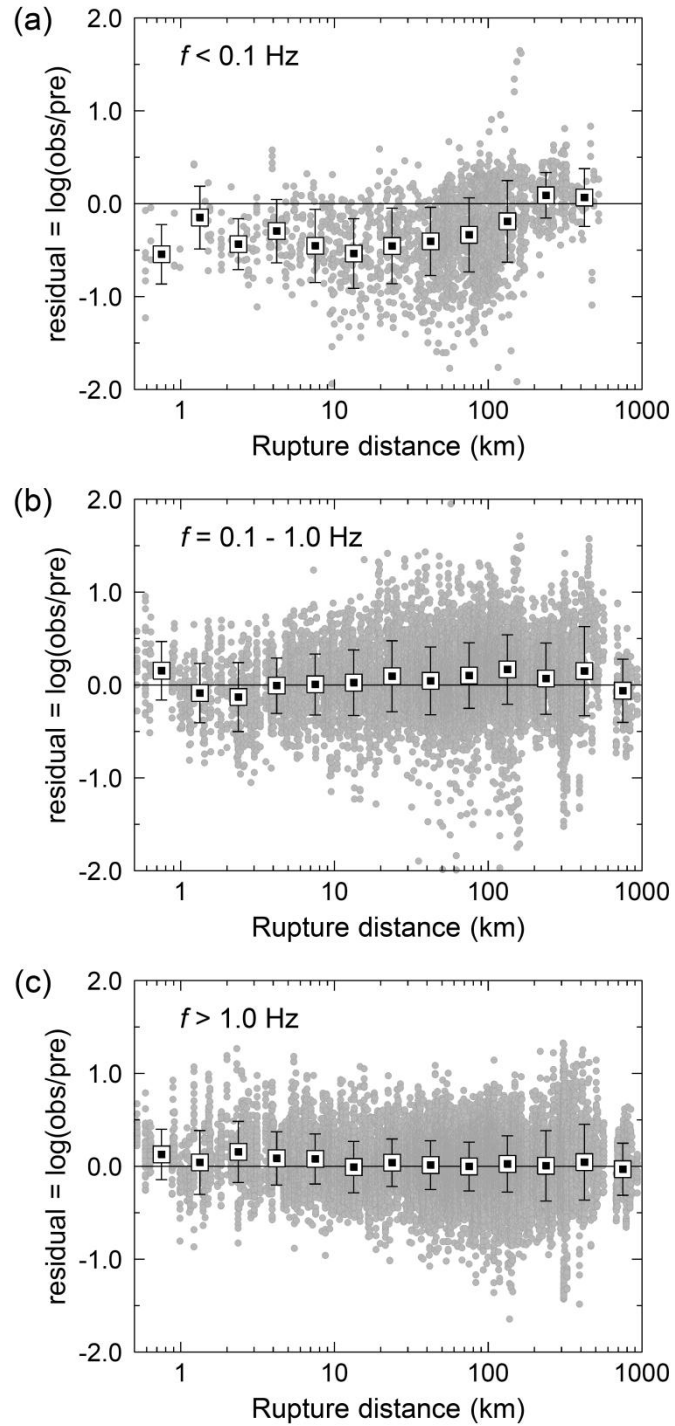
Figure 2.21 Residuals for Fourier amplitude predictions at (a) low (b) intermediate and (c) high frequencies based on the equivalent point-source model that is determined for linear geometrical attenuation with $b = -1.0$. Squares indicate the mean residuals computed in logarithmically-spaced distance bins; error bars represent standard deviation about the mean.

2.10 Insights into magnitude-dependent attenuation

Finally, we compared observed Fourier amplitudes of the **M**6.0 Christchurch-II and **M**7.62 Chi-Chi earthquakes to gain insights into the magnitude-dependent attenuation effects. As shown in Figure 2.22, the ground motions of the Christchurch-II earthquake monotonically increase with decreasing distance, showing no saturation at close distances. We note that the attenuation trend of this event remains unclear at distances less than 5 km due to the lack of empirical data. For example, an alternative attenuation model defined by b_1 = -1.1 and h = 3 km matches the ground motions of the Christchurch-II earthquake as well as the attenuation model with no saturation (i.e., b_1 = -1.1 and h = 0), as shown in Figure 2.22. However, we can say with confidence that the Christchurch-II earthquake shows no saturation at distances beyond 5 km, providing a clear distinction between the two events in the distance range over which the saturation effect applies. Both events attain similar amplitudes at ~5 km from the fault. However, ground motions from the Chi-Chi earthquake appear to attenuate at a much slower rate than for the Christchurch-II earthquake; thus Chi-Chi motions are larger than Christchurch-II motions at further distances. This behavior is typically represented as a dependence of ground-motion attenuation on magnitude in empirical ground-motion prediction equations (e.g., Figure 2.1).

Figure 2.22 also shows that while the simple equivalent point-source model does a good job of capturing the major amplitude trends, it does not reproduce all of the observed features perfectly. For example, the near-fault amplitudes (< 3 km) from Chi-Chi tend to be under-predicted at this frequency. For the Christchurch-II event, there is under-prediction of amplitudes from 50 to 150 km, possibly due to Moho-bounce effects. However, such discrepancies tend to average out when residuals are considered over multiple events, and over multiple frequency bands.
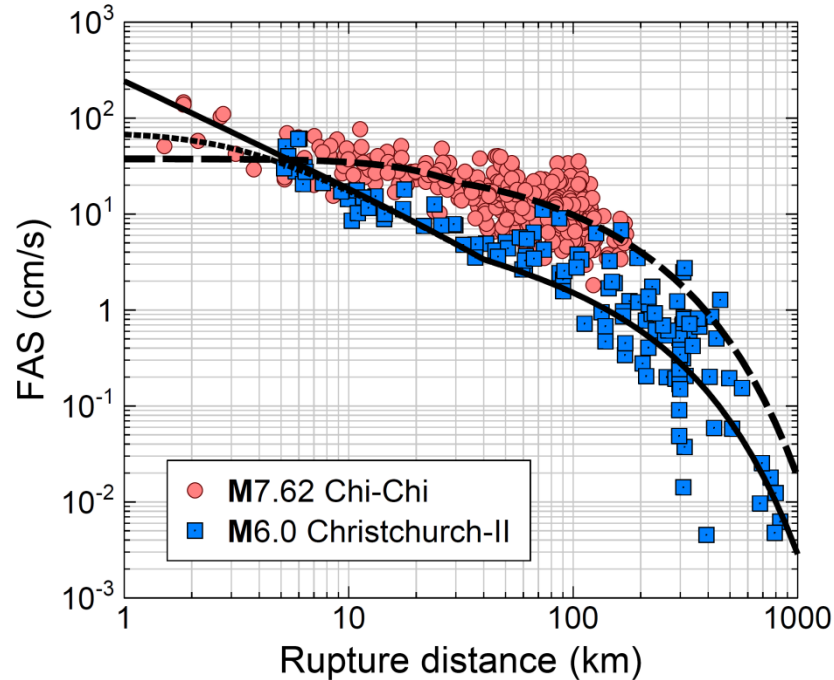
Figure 2.22 Observed Fourier amplitudes of **M**6.0 Christchurch-II (squares) and **M**7.62 Chi-Chi earthquakes (circles) at f = 1.1 Hz. Dotted and dashed lines represent the ground motions predicted based on the equivalent point-source model using the selected bilinear attenuation models, for **M**6.0 Christchurch-II (b_1 = -1.1 and h = 3 km) and **M**7.62 Chi-Chi (b_1 = -1.6 and h = 32.8 km) earthquakes, respectively. Solid line shows an alternative attenuation model for the Christchurch-II earthquake, where b_1 = -1.1 and h = 0.

In this study, the geometrical attenuation of observed ground motions are best described by b_1 = -1.1 and h = 0 to 3 km for the **M**6.0 Christchurch-II, and b_1 = -1.6 and h = 32.8 km for the **M**7.62 Chi-Chi earthquakes. Although the Chi-Chi earthquake is described by steeper b_1 than the Christchurch-II earthquake, the combined effects of b_1 and h result in a slower attenuation rate for the Chi-Chi earthquake. The comparison of attenuation attributes in Figure 2.22 has two important implications for ground-motion modeling with an equivalent point source:

(i)   The pseudo-depth (h), that determines the distance-dependent saturation effects, is the primary parameter that controls the resultant rate of ground-motion attenuation at close distances; and

(ii)   The origin of the observed magnitude-dependent attenuation in ground motion prediction equations is the dependence of h on magnitude, because h increases with magnitude, and the combined effects of b_1 and h result in a slower attenuation rate for large magnitude earthquakes compared to small events.

As a caution, we note that the magnitude-dependent attenuation attributes may be somewhat different when considering response spectral amplitudes rather than Fourier amplitudes, because the full frequency content and the ground-motion duration contribute to the response spectrum. For example, Cotton et al. (2008) and Atkinson (2012) have shown that even if no magnitude-dependency is prescribed for the attenuation of Fourier amplitudes in point-source simulations, simulated response spectra attenuate with distance at a slower rate for large earthquakes than that for small events.

2.11 Conclusions

We modeled 11 well-recorded **M**6+ shallow crustal earthquakes from different regions to investigate the utility of the equivalent point-source approach to describe the ground motions from large earthquakes. The main conclusions of this study are:

- There is a strong trade-off between source and attenuation modeling parameters. Seismic moment and stress drop inferred from regressions increase as the assumed geometrical attenuation at close distances gets steeper (i.e., b_1 decreases). Using the known seismic moment as a regression constraint ensures that the selected model is both statistically and physically consistent with observed ground motions.

- Stress drop should not be compared between events or studies without reference to the adopted attenuation models. Stress drops corrected to the equivalent value for the commonly-adopted $b_1 = -1.0$ attenuation model have a log-average value of 81 bars with a standard deviation of a factor of 1.5, for **M**6+ earthquakes. For an attenuation model with $b_1 = -1.3$, the corresponding average stress would be 310 bars.

- Most of the **M** ≥ 6 earthquakes can be modeled satisfactorily by using the Brune point-source model. For two **M**6+ earthquakes in California we observed a spectral-sag at intermediate frequencies. For such earthquakes, a double-corner point source model provides a better match than the Brune model.

- Observed ground motions saturate at close distances to the fault, with the saturation distance increasing with magnitude. The relation between pseudo-depth (*h*), that determines the distance-saturation effects, and magnitude is defined as $\log(h) = -1.72 + 0.43\mathbf{M}$ with standard deviation of 0.19 in log units, for **M** ≥ 6 earthquakes.

- The pseudo-depth controls the resultant rate of ground-motion attenuation at close distances. The magnitude-dependent attenuation observed in empirical data is primarily due to the dependence of *h* on magnitude.

- An equivalent point-source model based on the effective distance concept can successfully predict the average ground motions from **M**6+ earthquakes at a wide distance range, including close distances (<20 km).

2.12 Data and resources

Ground motions used in this study were compiled from following online databases (last accessed March 2014): PEER-NGA (http://peer.berkeley.edu/nga), USGS National Strong-Motion Project (http://nsmp.wr.usgs.gov), Center for Engineering Strong Motion Data (http://strongmotioncenter.org), New Zealand Geological Hazard Monitoring System (ftp://ftp.geonet.org.nz), European Strong-Motion Database (http://www.isesd.hi.is), Italian Accelerometric Archive (http://itaca.mi.ingv.it/ItacaNet) and Turkish Strong-Motion Database (http://kyhdata.deprem.gov.tr/2K/kyhdata_v4.php). PGA predictions presented in Figure 2.1 and source-to-site distances were determined by using Dr. David M. Boore's NGA08_GM_TMR.EXE and DIST_3D.EXE software, respectively (http://www.daveboore.com/software_online.html, last accessed March 2014). Fault geometries adopted in distance calculations were obtained from Dr. P. Martin Mai's finite-source rupture model database (http://www.seismo.ethz.ch/static

/srcmod/ Homepage.html, last accessed March 2014). The global crustal model, CRUST 2.0, used for values of ρ and β, is available at http://igppweb.ucsd.edu/~gabi/crust2.html (last accessed March 2014). All graphics were produced using CoPlot (www.cohort.com, last accessed March 2014).

2.13 Acknowledgements

2.14 References

Abrahamson, N., and W. Silva (2008). Summary of the Abrahamson & Silva NGA Ground-Motion Relations, *Earthquake Spectra* **24**, 67–97.

Allen, T., P. Cummins, T. Dhu, and J. Schneider (2007). Attenuation of ground-motion spectral amplitudes in southeastern Australia, *Bull. Seismol. Soc. Am.* **97**, 1279–1292.

Anderson, J. G. (2000). Expected shape of regressions for ground-motion parameters on rock, *Bull. Seismol. Soc. Am.* **90**, S43–S52.

Anderson, J. G., and S. E. Hough (1984). A model for the shape of the Fourier amplitude spectrum of acceleration at high frequencies, *Bull. Seismol. Soc. Am.* **74**, 1969–1993.

Atkinson, G. M. (2004). Empirical attenuation of ground-motion spectral amplitudes in southeastern Canada and the northeastern United States, *Bull. Seismol. Soc. Am.* **94**, 1079–1095.

Atkinson, G. M. (2012). Evaluation of attenuation models for the northeastern United States/southeastern Canada, *Seismol. Res. Lett.* **83**, 166–178.

Atkinson, G. M., and D. M. Boore (1995). Ground-motion relations for eastern North America, *Bull. Seism. Soc. Am.* **85**, 17-30.

Atkinson, G. M., and D. Boore (2006). Ground motion prediction equations for earthquakes in eastern North America. *Bull. Seism. Soc. Am.* **96**, 2181-2205.

Atkinson, G. M., and R. F. Mereu (1992). The shape of ground motion attenuation curves in southeastern Canada, *Bull. Seismol. Soc. Am.* **82**, 2014-2031.

Atkinson, G. M., and W. Silva (1997). An empirical study of earthquake source spectra for California earthquakes, *Bull. Seismol. Soc. Am.* **87**, 97–113.

Atkinson, G. M., and W. Silva (2000). Stochastic modeling of California ground motions, *Bull. Seismol. Soc. Am.* **90**, 255–274.

Boatwright, J., and G. L. Choy (1992). Acceleration source spectra anticipated for large earthquakes in northeastern North America, *Bull. Seismol. Soc. Am.* **82**, 660–682.

Bommer, J. J., and S. Akkar (2012). Consistent source-to-site distance metrics in ground-motion prediction equations and seismic source models for PSHA. *Earthquake Spectra*, **28**, 1–15.

Bommer, J. J., P. J. Stafford, and S. Akkar (2010). Current empirical ground-motion prediction equations for Europe and their application to Eurocode 8, *Bulletin of Earthquake Engineering*, **8**, 5–26.

Boore, D. M. (1983). Stochastic simulation of high-frequency ground motions based on seismological models of the radiated spectra, *Bull. Seismol. Soc. Am.* **73**, 1865–1894.

Boore, D. M. (2001). Comparisons of ground motions from the 1999 Chi-Chi earthquake with empirical predictions largely based on data from California, *Bull. Seismol. Soc. Am.* **91**, 1212–1217.

Boore, D. M. (2003). Simulation of ground motion using the stochastic method, *Pure and Applied Geophysics*, **160**, 635-376.

Boore, D. M. (2009). Comparing stochastic point-source and finite-source ground motion simulations: SMSIM and EXSIM, *Bull. Seismol. Soc. Am.* **99**, 3202–3216.

Boore, D. M., and G. M. Atkinson (2008). Ground-motion prediction equations for the average horizontal component of PGA, PGV, and 5%-damped PSA at spectral periods between 0.01 s and 10.0 s, *Earthquake Spectra* **24**, 99–138.

Boore, D. M., K. W. Campbell, and G. M. Atkinson (2010). Determination of stress parameters for eight well-recorded earthquakes in eastern North America, *Bull. Seismol. Soc. Am.* **100**, 1632–1645.

Brune, J. N. (1970). Tectonic stress and the spectra of seismic shear waves from earthquakes, *J. Geophys. Res.* **75**, 4997–5009.

Brune, J. N. (1971). Tectonic stress and the spectra of seismic shear waves from earthquakes: Correction, *J. Geophys. Res.* **76**, 5002.

Burger, R. W., P. G. Somerville, J. S. Barker, R. B. Herrmann, and D. V. Helmberger (1987). The effect of crustal structure on strong ground motion attenuation relations in eastern North America, *Bull. Seismol. Soc. Am.* **77**, 420–439.

Campbell, K. W., and Y. Bozorgnia, (2006). Next Generation Attenuation (NGA) empirical ground motion models: can they be used in Europe? *Proceedings of the 1st European Conference on Earthquake Engineering and Seismology*, Paper No. 458.

Campbell, K. W., and Y. Bozorgnia (2008). NGA ground motion model for the geometric mean horizontal component of PGA, PGV, PGD and 5% damped linear elastic response spectra for periods ranging from 0.01 to 10 s, *Earthquake Spectra* **24**, 139–171.

Chen, K. C., T. C. Shin, and J. H. Wang (1989). Estimates of coda Q in Taiwan, *Proceedings of the Geological Society of China* **32**, 339–353.

Chapman, M. C., and R. W. Godbee (2012). Modeling geometrical spreading and the relative amplitudes of vertical and horizontal high-frequency ground motions in eastern North America, *Bull. Seismol. Soc. Am.* **102**, 1957–1975.

Chiou, B., R. Darragh, N. Gregor, and W. Silva (2008). NGA Project Strong-Motion Database, *Earthquake Spectra* 24, 23–44.

Chiou, B. S.-J., and R. R. Youngs (2008). An NGA model for the average horizontal component of peak ground motion and response spectra, *Earthquake Spectra* **24**, 173–215.

Cotton, F., G. Pousse, F. Bonilla and F. Scherbaum (2008). On the discrepancy of recent European ground-motion observations and predictions from empirical models: Analysis of KiK-net accelerometric data and point-sources stochastic simulations. *Bull. Seismol. Soc. Am.* **98**, 2244–2261.

Frankel, A. (2009). A constant stress-drop model for producing broadband synthetic seismograms: Comparison with the Next Generation Attenuation relations, *Bull. Seismol. Soc. Am.* **99**, 664–680.

Furumura, T., K. Koketsu, and K.-L. Wen (2002). Parallel PSM/FDM hybrid simulation of ground motions from the 1999 Chi-Chi, Taiwan, earthquake, *Pure and Applied Geophysics* **159**, 2133–2146.

Graves R. W., and A. Pitarka (2010). Broadband ground-motion simulation using a hybrid approach, *Bull. Seismol. Soc. Am.* **100**, 2095–2123.

Gusev, A. A. (1983). Descriptive statistical model of earthquake source radiation and its application to an estimation of short-period strong motion, *Geophys. J. R. Astr. Soc*. **74**, 787–808.

Halldorsson, B., and A. S. Papageorgiou (2005). Calibration of the specific barrier model to earthquakes of different tectonic regions, *Bull. Seismol. Soc. Am.* **95**, 1276–1300.

Hanks, T. C., and R. K. McGuire (1981). The character of high-frequency strong ground motion, *Bull. Seismol. Soc. Am.* **71**, 2071–2095.

Hartzell, S., S. Harmsen, A. Frankel, and S. Larsen (1999). Calculation of broadband time histories of ground motion: Comparison of methods and validation using strong-

ground motion from the 1994 Northridge earthquake, *Bull. Seismol. Soc. Am.* **89**, 1484–1504.

Houtte, C. V., S. Drouet, and F. Cotton, (2011). Analysis of the origins of κ (kappa) to compute hard rock to rock adjustment factors for GMPEs, *Bull. Seismol. Soc. Am.* **101**, 2926–2941.

Irikura, K. (1978). Semi-empirical estimation of strong ground motions during large earthquakes, *Bull. Disast. Prev. Res. Inst., Kyoto Univ.* **33**, 63–104.

Lermo, J., and F. Chavez-Garcia (1993). Site effect evaluation using spectral ratios with only one station, *Bull. Seismol. Soc. Am.* **83**, 1574–1594.

Liu, P., R. Archuleta, and S. H. Hartzell (2006). Prediction of broadband ground motion time histories: Frequency method with correlation random source parameters, *Bull. Seismol. Soc. Am.* **96**, 2118–2130.

Liu, T. J., G. M. Atkinson, H. P. Hong, and K. Assatourians (2012). Intraevent spatial correlation characteristics of stochastic finite-fault simulations, *Bull. Seismol. Soc. Am.* **102**, 1740–1747.

Mahani, A. B., and G. M. Atkinson (2012). Evaluation of functional forms for the attenuation of small-to-moderate-earthquake response spectral amplitudes in North America, *Bull. Seismol. Soc. Am.* **102**, 2714–2726.

Motazedian, D., and G. M. Atkinson (2005). Stochastic finite-fault modeling based on a dynamic corner frequency, *Bull. Seismol. Soc. Am.* **95**, 995–1010.

NEHRP (2000). *NEHRP Recommended provisions for seismic regulations for new buildings and other structures, Part 1, Provisions, FEMA 368*, Federal Emergency Management Agency, Washington, D.C.

Ojo, S., and R. Mereu (1986). The effect of random velocity functions on the travel times and amplitudes of seismic waves, *Geophysical Journal of the Royal Astronomical Society* **84**, 607–618.

Ou, G.-B., and R. B. Herrmann (1990). A statistical model for ground motion produced by earthquakes at local and regional distances, *Bull. Seismol. Soc. Am.* **80**, 1397–1417.

Raoof, M., R. B. Herrmann, and L. Malagnini, (1999). Attenuation and excitation of three-component ground motion in southern California, *Bull. Seismol. Soc. Am.* **89**, 888–902.

Rogers, A. M., and D. M. Perkins (1996). Monte Carlo simulation of peak acceleration attenuation using a finite-fault uniform-patch model including isochron and extremal characteristics, *Bull. Seismol. Soc. Am.* **86**, 79–92.

Roumelioti, Z., and I. A. Beresnev (2003). Stochastic finite-fault modeling of ground motions from the 1999 Chi-Chi, Taiwan, earthquake: Application to rock and soil sites with implications for nonlinear site response, *Bull. Seismol. Soc. Am.* **93**, 1691–1702.

Somerville, P., J. McLaren, C. Saikia, and D. Helmberger (1990). The 25 November 1988 Saguenay, Quebec earthquake: Source parameters and the attenuation of strong ground motion, *Bull. Seismol. Soc. Am.* **80**, 1118–1143.

Somerville, P., M. Sen, and B. Cohee (1991). Simulations of strong ground motions recorded during the 1985 Michoacan, Mexico and Valparaiso, Chile, earthquakes, *Bull. Seismol. Soc. Am.* **81**, 1–27.

Stafford, P. J., F. O. Strasser, and J. J. Bommer (2008). An evaluation of the applicability of the NGA models to ground-motion prediction in the Euro-Mediterranean region, *Bulletin of Earthquake Engineering* **6**, 149–177.

Trifunac, M. D. (1976). Preliminary empirical model for scaling Fourier amplitude spectra of strong ground acceleration in terms of earthquake magnitude, source-to-station distance, and recording site conditions, *Bull. Seismol. Soc. Am.* **66**, 1343–1373.

Wang, G.-Q., G.-Q. Tang, D. M. Boore, G. V. N. Burbach, C. R. Jackson, X.-Y. Zhou, and Q.-L. Lin (2006). Surface waves in the western Taiwan coastal plain from an aftershock of the 1999 Chi-Chi, Taiwan, earthquake, *Bull. Seismol. Soc. Am.* **96**, 821–845.

Yenier, E., and G. M. Atkinson (2014). Equivalent point-source modeling of moderate-to-large magnitude earthquakes and associated ground-motion saturation effects, *Bull. Seismol. Soc. Am.* **104**, 1458–1478.

Chapter 3

3 An equivalent point-source model for stochastic simulation of earthquake ground motions in California[2]

3.1 Introduction

Engineers require predictions of earthquake ground motions for future events in order to determine the earthquake-driven forces and deformations for structural design. Stochastic simulations are widely used to develop ground-motion prediction equations (GMPEs) as an alternative to empirical methods, particularly in stable continental regions where empirical data are limited (e.g., Atkinson and Boore, 1995; 2006; Toro et al., 1997; Campbell, 2003; Pezeshk et al., 2011; Atkinson et al., 2014). Stochastic methods are a useful tool in engineering seismology due to their simplicity and success in predicting ground motions at frequencies of common engineering interest (Hanks and McGuire, 1981; Boore, 2003).

The Fourier acceleration spectrum (*FAS*) as a function of magnitude and distance is the essential component of stochastic simulations, as it carries the underlying seismological model. It is defined as the product of source, travel-path and site effects operators. The seismic source can be modeled as either a point-source (e.g., Brune, 1970; Atkinson and Silva 2000; Boore et al., 2014a) or a propagating finite-source (e.g., Motazedian and Atkinson, 2005; Boore, 2009). Point-source models typically assume that the total seismic energy is released from a single point, which yields simulated amplitudes that increase constantly with decreasing distance. As observed in empirical data, however, the magnitude- and distance-scaling of ground motions weakens at close distances to large earthquakes, because ground motions near a large rupture are primarily controlled by the

---

[2] A version of this chapter has been submitted for publication. Yenier, E., and G. M. Atkinson (2015). An equivalent point-source model for stochastic simulation of earthquake ground motions in California, *Bull. Seismol. Soc. Am.*

closest portions of the fault. This effect is called *ground-motion saturation* and is magnitude dependent, extending to further distances with increasing magnitude (Rogers and Perkins, 1996; Anderson, 2000; Yenier and Atkinson, 2014). Finite-source models are often employed at close distances to large earthquakes because they are better able to model the causative physical processes of saturation effects (e.g., Atkinson and Silva, 2000; Motazedian and Atkinson, 2005).

Alternatively, the predictions from point-source models can be improved to mimic finite-fault effects by placing the point at an equivalent overall distance, such that the close-distance motions saturate appropriately (Atkinson and Silva, 2000; Boore, 2009; Yenier and Atkinson, 2014). This can be achieved by defining the ground-motion attenuation as a function of an effective distance metric that is given as $R = (D^2 + h^2)^{0.5}$, where D is an actual distance measure (e.g., hypocentral or rupture distance) and h is a pseudo-depth term that accounts for saturation effects. This method, whereby the motions are assumed to radiate from a virtual point, is referred to as *equivalent point-source modeling*. Recent studies (e.g., Yenier and Atkinson, 2014; Boore et al., 2014a) have shown that this method can successfully reproduce the average observed motions from moderate-to-large events (moment magnitude, $\mathbf{M} \geq 6$) at close distances (< 20 km), based on parameters obtained from empirical inversion. In this study, we greatly widen the scope of previous studies, to produce an equivalent point-source model that reproduces response spectra for California earthquakes of $\mathbf{M}3.0$ to $\mathbf{M}7.5$, at frequencies > 0.2 Hz, for distances from 1 km to 400 km.

The recently-compiled Next Generation Attenuation - West 2 (NGA-West2) database provides a rich ground-motion database for California, from which to examine the reliability of equivalent point-source simulations over a wide range of magnitudes, distances and frequencies. Stochastic simulations in previous studies, by contrast, were assessed using more limited ground-motion datasets (e.g., Silva et al., 1996; Atkinson and Silva, 2000; Goulet et al. 2015; Boore et al., 2014a). The current database enables a much more comprehensive evaluation of the methodology and its parameter trade-offs. Furthermore, the simulation model can provide guidance to develop prediction equations for magnitude and distance ranges where the empirical data are sparse. For example,

predictions from equivalent point-source simulations can be compared against observed motions from large earthquakes in order to examine other extended source effects, such as hanging-wall/footwall effects and rupture directivity effects. Finally, equivalent point-source simulations can provide a reasonable basis for developing a generic ground-motion prediction equation (GMPE) that can be adjusted for regional source and attenuation parameters, facilitating the development of GMPEs in data-poor regions such as eastern North America.

This study derives models for the source and attenuation attributes of California earthquakes, which can be incorporated into equivalent point-source simulations to predict average response spectra. In this respect, we develop a regional model for the stress parameter using the values obtained from study events. Conventionally, the stress parameter is often determined by matching the observed high-frequency amplitudes to the values predicted for the given seismic moment, most commonly using the Brune (1970) point-source model (e.g. Hanks and McGuire, 1981; Atkinson, 1993). In this study, by contrast, we calculate the stress parameter by matching the simulated and observed response spectral *shapes* (rather than amplitudes) over a wide frequency range. The use of spectral shape ensures that an appropriate corner frequency is determined for each event. Because the source spectrum for an event is defined only by shape, its overall level may require adjustment by a constant in order to match the long-period amplitudes as predicted by the seismic moment. The advantage of using shape to specify the spectrum is that the application of this frequency-independent constant ensures a good match of the observed spectrum to the model spectrum over a wide frequency band. In our study, we will show that the shape-based stress parameter has an average value of 150 bars for all events having focal depths > 12 km. However, there is clear evidence that its value is depth-dependent, with shallow events having lower stress. For small-to-moderate events, we also observe a magnitude-dependence of stress, as has been noted in previous studies. We also show that a significant calibration constant may be required to match the observed response spectral amplitudes. The value of the calibration constant is linked to the attenuation model, in particular the geometric spreading rate. We select the best-fitting geometric spreading model by inspecting distance-dependence of the residuals between observed and simulated amplitudes, as evaluated for alternative

models. We conclude the paper with a recipe for developing a generic GMPE that can be adjusted for use in a different region, by simple modifications of its source and attenuation modeling parameters.

3.2 California ground-motion dataset

We compile response spectra for California earthquakes with $\mathbf{M} \geq 3.0$ that were recorded by three or more stations within 400 km. We use the 5%-damped, pseudo-spectral acceleration (*PSA*) of the average horizontal-component ground motion, as provided in NGA-West2 flatfile (see Data and Resources), where the average horizontal-component *PSA* values were calculated based on the RotD50 measure (see Boore (2010) regarding RotD50). Figure 3.1 shows a map of the epicenters of the study events and Figure 3.2 shows the magnitude-distance distribution of the selected records.
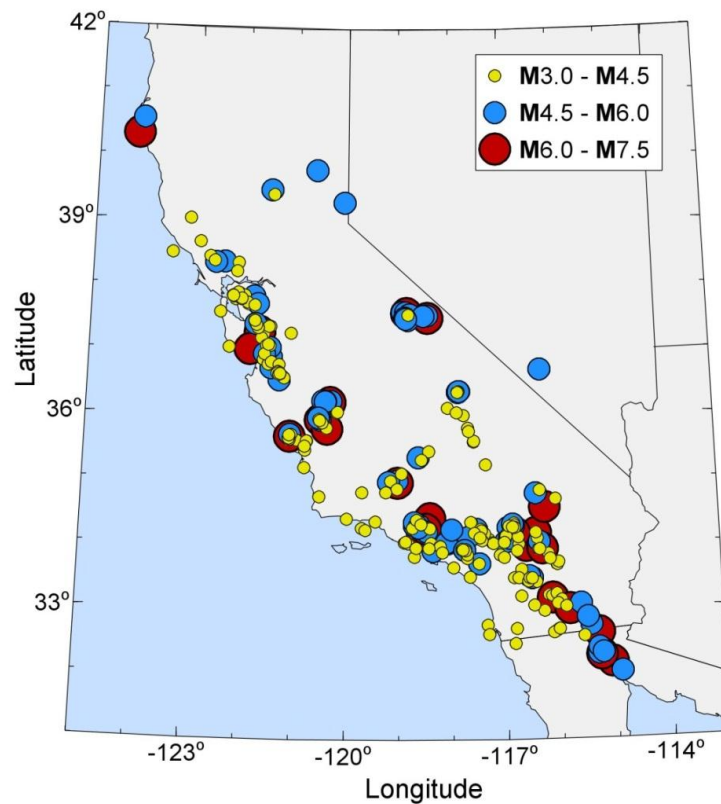
Figure 3.1 Epicenters of California earthquakes selected for analysis
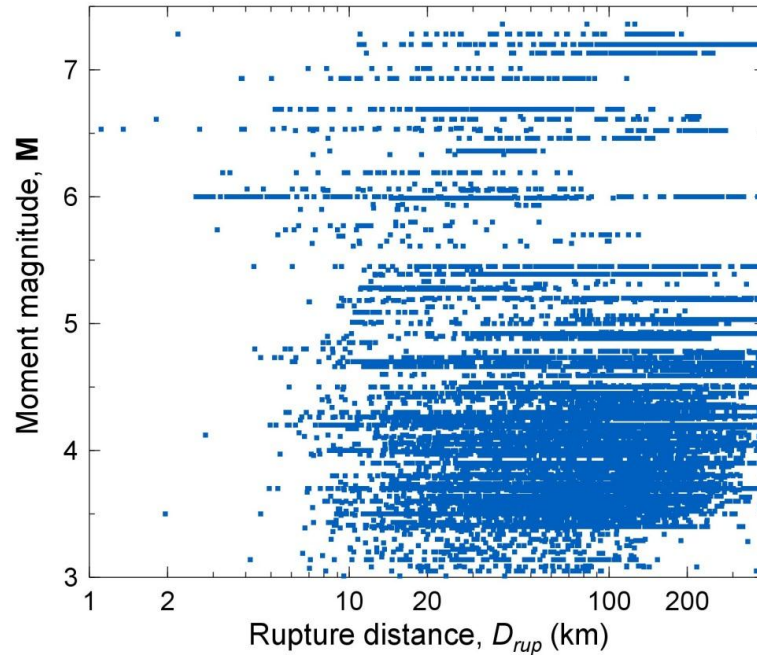
Figure 3.2 Magnitude-distance distribution of the ground-motion data used in this study

The selected ground motions were recorded on a variety of site conditions. To reduce the complications due to site effects, we use the California site effects model of Boore et al. (2014b) to correct all observed response spectra to equivalent motions on NEHRP (National Earthquake Hazards Reduction Program) B/C site conditions (travel-time weighted average shear-wave velocity over the top 30 m, V_{S30}, of 760 m/s). Ground motions recorded at NEHRP E sites ($V_{S30} < 180$ m/s) are excluded in this study. We acknowledge that any inadequacies or misfits in the site response model will map into trade-offs or unresolved residuals in the study results, which we search for later.

3.3 Ground-motion simulation methodology

We implement time-domain ground-motion simulations using the SMSIM algorithm (Boore, 2005), which is based on the stochastic point-source simulation method introduced by Boore (1983, 2003). The Fourier acceleration spectrum (*FAS*) is the fundamental ingredient of stochastic simulations. It encapsulates the basic physics of the

seismic-wave radiation from an earthquake source and all propagation effects (Boore, 2003). The Fourier acceleration spectrum at frequency f, is given as:

$$FAS(f) = A_0(M_0, f) \, Z(R) \, exp(-\pi f R/Q\beta) \, S(f) \, exp(-\pi \kappa_0 f) \tag{3.1}$$

M_0 is the seismic moment and β is the shear-wave velocity in the vicinity of the source. A_0 represents the acceleration source spectrum, Z is the geometrical spreading as a function of distance (R) and $exp(-\pi f R/Q\beta)$ defines the anelastic attenuation as the inverse of the regional Quality factor, Q. The site amplification (including amplification through the crustal velocity gradient) is given by S and the near-surface attenuation is formulated by the last exponential term, in terms of the κ_0 operator of Anderson and Hough (1984). We use the single-corner frequency Brune (1970) model to characterize the acceleration source spectrum, A_0:

$$A_0(M_0, f) = C M_0 \left[\frac{(2\pi f)^2}{1 + (f/f_0)^2} \right] \tag{3.2}$$

where C is a scaling constant, and f_0 is the corner frequency. The relationship between seismic moment (M_0) and moment magnitude (**M**) is $\log M_0 = 1.5\mathbf{M} + 16.05$ for M_0 in dyne-cm (Hanks and Kanamori, 1979). The scaling constant in Equation 3.2 is typically taken as $C = R_{\Theta\phi} V F/(4\pi\rho\beta^3)$, where $R_{\Theta\phi}$ is the radiation pattern ($= 0.55$ on average for shear waves), V is the partitioning of seismic energy onto two horizontal components ($= 0.707$) and F is the free surface amplification ($= 2$). The typical values of density and shear-wave velocity in the vicinity of the source are $\rho = 2.8$ g/cm^3 and $\beta = 3.7$ km/s for California, respectively. The corner frequency, f_0, of the Brune model is:

$$f_0 = 4.9 \times 10^6 \, \beta \, (\Delta\sigma/M_0)^{1/3} \tag{3.3}$$

where the seismic moment (M_0), stress parameter ($\Delta\sigma$), and shear-wave velocity (β) are in dyne-cm, bar and km/s, respectively (see Boore, 2003). Note that corner frequency is the essential spectral shape parameter for the Brune model: the acceleration spectrum rises as the square of frequency to the corner frequency, above which it attains a constant amplitude level (except for the effects of the κ_0 operator). There is a well-known trade-off

between $\Delta\sigma$ and κ_0, so that these parameters should be considered coupled in ground-motion modeling.

To account for ground-motion saturation effects with distance, we define the ground-motion attenuation as a function of effective distance, R, which is given as:

$$R = \sqrt{D_{rup}^2 + h^2} \qquad (3.4)$$

where D_{rup} is the closest distance to the rupture surface and h is a pseudo-depth term that accounts for saturation effects. Physically, R cannot attain a value less than h, by definition. Therefore, in a general case for which $h > 1$ km, $R = 1$ km represents a virtual point which defines the ground motions that would be projected to the source if there were no saturation effects. It is important to recognize that the equivalent point source is this virtual point, not an actual point on the fault rupture.

Figure 3.3 shows pseudo-depths (h) determined from modeling of well-recorded earthquakes around the world (including California, Italy, Japan, New Zealand, Taiwan and Turkey). As noted in previous studies, h values show an increasing trend with magnitude due to the extended saturation effects for large events. The h model proposed by Atkinson and Silva (2000), which was derived from California earthquakes, agrees with the pseudo-depths obtained from $\mathbf{M} < 6$ Christchurch aftershocks, in general. For large events, however, h values attain a steeper slope with magnitude in comparison to those obtained from small earthquakes. This might be related to the change in the aspect ratio of the rupture area with increasing magnitude. For $\mathbf{M} > 6$, the h model proposed by Yenier and Atkinson (2014, Chapter 2) is in good agreement with the empirically determined values. On balance, we adopt the relation of Atkinson and Silva (2000) for events of $\mathbf{M} < 6.0$, and the relation of Yenier and Atkinson (2014) for events of $\mathbf{M} > 6.0$ as:

$$\log h = \max(-0.05 + 0.15\mathbf{M}, -1.72 + 0.43\mathbf{M}) \qquad (3.5)$$
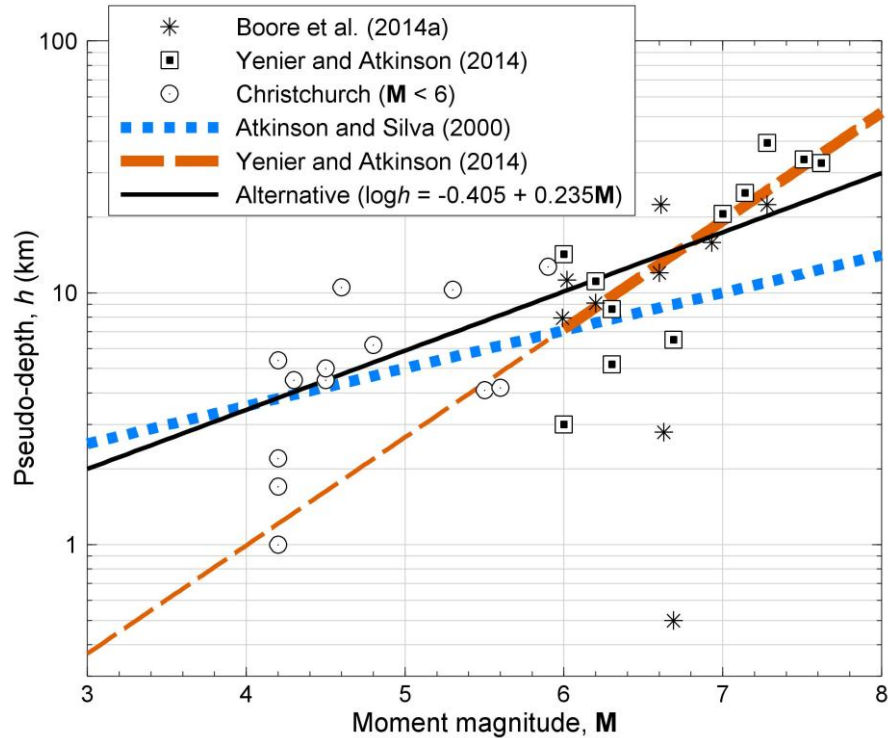
Figure 3.3 Pseudo-depths (*h*) determined from modeling of observed ground motions (symbols). Asterisks and squares indicate *h* values obtained from well-recorded earthquakes of $\mathbf{M} \geq 6$ around the world by Boore et al. (2014a) and Yenier and Atkinson (2014), respectively. Pseudo-depths obtained from the analysis of the 2010-2012 Christchurch, New Zealand aftershocks are also shown (Yenier and Atkinson, manuscript in preparation). The relations proposed by Atkinson and Silva (2000) and Yenier and Atkinson (2014) are indicated by heavy lines. The latter model was derived for earthquakes of $\mathbf{M} \geq 6$. The thin dashed line shows its extrapolation for smaller events. The thin solid line shows an alternative *h* model (Equation 3.13) that avoids over-saturation of predicted amplitudes for large M (discussed later).

In Equation 3.1, the total path effect is determined as the product of geometrical spreading and anelastic attenuation. The geometrical spreading, *Z*, refers to the decay of ground-motion amplitudes due to the spreading of seismic-waves over an increasing area with the expansion of the wavefronts. *Z* is generally modeled as a piecewise continuous function, because the rate of geometrical spreading is often distance-dependent. At close distances, ground motions are primarily controlled by direct waves. Direct waves would

attenuate as $R^{-1.0}$ as a result of spherical spreading in a whole-space. However, theoretical waveform simulations suggest steeper spreading, about $R^{-1.3}$, for typical layered earth models (Ojo and Mereu 1986; Burger et al., 1987; Ou and Herrmann, 1990; Somerville et al., 1990; Chapman and Godbee, 2012, Chapman 2013). Recent studies on the empirical modeling of ground motions also support this finding. For example, Babaie Mahani and Atkinson (2012) investigated variations in the shape and rate of geometrical spreading across North America, and found apparent rates between $R^{-1.1}$ and $R^{-1.3}$ at close distances, for most regions in North America. Additionally, Yenier and Atkinson (2014) modeled ground motions from 11 well-recorded earthquakes of $\mathbf{M} \geq 6$ selected across the world, including California, and found that geometrical spreading is generally steeper than $R^{-1.0}$ at close distances, for most of the study events.

At far distances, ground motions are dominated by surface waves (and/or trapped phases containing multiple reflections and refractions) which typically decay as $R^{-0.5}$ (cylindrical spreading in a half space). The transition from direct-wave to surface-wave spreading generally occurs at distances from 40 km to 100 km, depending on the focal depth, faulting mechanism and crustal structure (Burger et al. 1987; Ou and Herrmann 1990).

In this study, we use a hinged bilinear geometrical spreading function for the simulation of ground motions:

$$Z(R) = \begin{cases} R^{b_1} & R \leq R_t \\ R_t^{(b_1-b_2)} R^{b_2} & R > R_t \end{cases} \tag{3.6}$$

where the transition from direct-wave to surface-wave spreading is assumed to occur at a distance of R_t = 50 km. This assumption is in accord with the findings of the studies mentioned above, which have also shown that the obtained models are not sensitive to the exact value selected for the transition distance (e.g., similar results would be obtained for any transition distance in the range from 40 to 70 km). The parameters b_1 and b_2 represent the geometrical spreading rates at $R \leq 50$ km and $R > 50$ km, respectively. The geometrical spreading rate at $R > 50$ km is fixed at the widely-used value of b_2 = -0.5, consistent with attenuation of surface waves in a half-space (Ou and Herrmann 1990; Atkinson 2012). We perform simulations for two alternative geometrical spreading rates

at $R \leq 50$ km: (i) $b_1 = -1.0$ and (ii) $b_1 = -1.3$, and assess their ability to reproduce observed motions in California, particularly at close distances.

Figure 3.4 shows the two alternative geometrical spreading models. Both models produce a bilinear shape in logarithmic space when there is no close-distance saturation ($h = 0$). However, their amplitudes roll off to attain a constant value at close distances when saturation effects are considered ($h > 0$). This is more prominent for large events due to their stronger saturation effects. At distances less than 50 km, the ground-motion attenuation is controlled by the apparent rate of geometrical spreading, which is a function of both b_1 and h (Yenier and Atkinson, 2014). For small events, b_1 has more control on the apparent geometrical-spreading rate than h because small events show little ground-motion saturation. Therefore, geometrical spreading models with different b_1 values show diagnostic differences in shape of the attenuation curve only for small events, as seen in Figure 3.4. Saturation effects extend to further distances with increasing magnitude, so that the apparent geometrical-spreading rate is overpowered by the effects of h at close distances for large events. That is why the geometrical spreading models with different b_1 values result in very similar attenuation shapes for large events (Figure 3.4). This makes the modeling of ground motions ambiguous, particularly for large events. In this respect, close-distance observations from small events can be useful to determine the rate of geometrical spreading, because the residuals obtained from ground-motion simulations for small events are diagnostic of the actual b_1 value. We consider this criterion to select the regional value of the b_1 parameter, among the two alternative values. It is important to note that the alternative geometrical spreading models will require calibration to differing apparent source amplitude levels, to achieve the same net amplitude at a fixed observation point (Boore et al., 2010; Yenier and Atkinson, 2014).
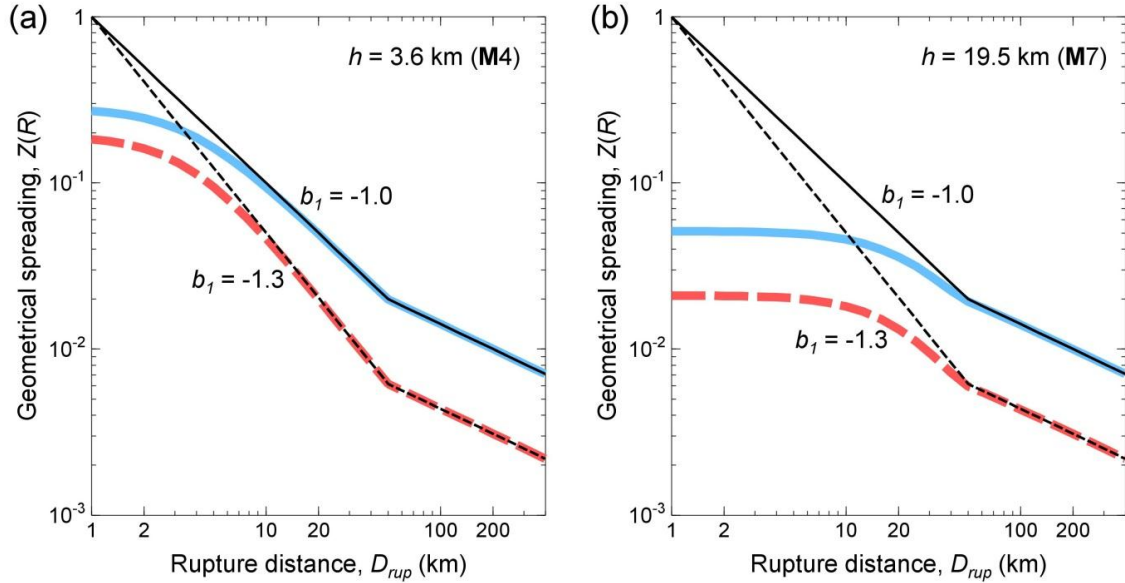
Figure 3.4 Illustration of geometrical spreading models for $b_1 = -1.0$ (solid lines) and $b_1 = -1.3$ (dashed lines). Thin lines represent the geometrical spreading with no close-distance saturation ($h = 0$). Heavy lines indicate the saturated geometrical spreading for (a) $h = 3.6$ km and (b) $h = 19.5$ km where pseudo-depths are determined based on Equation 3.5 for **M**4 and **M**7, respectively.

The anelastic attenuation is defined as a function of effective distance, R, and a frequency-dependent Quality factor, Q, in Equation 3.1. Q controls the decay of ground-motion amplitudes at large distances, particularly for high-frequencies. Therefore, it trades off with the geometrical spreading rate b_2, at far distances. Raoof et al. (1999) found $Q = 180 f^{0.45}$ for southern California, assuming $\beta = 3.5$ km/s and $b_2 = -0.5$. Because we make the same assumption for b_2, we adopt their Q model, after scaling it to an equivalent value for $\beta = 3.7$ km/s (our adopted value of β):

$$Q = \max(100, \ 170.3 f^{0.45}) \tag{3.7}$$

We assume a minimum value of $Q = 100$ based on the findings of Boore (1984) and Yenier and Atkinson (2014).

We simulate ground motions at NEHRP B/C site condition because all observed response spectra have been corrected to NEHRP B/C to simplify the problem. Atkinson and Boore

(2006) calculated Fourier amplitude crustal amplification factors for the NEHRP B/C site condition based on square-root-impedance method and a crustal velocity model as given by Frankel et al. (1996). We use these factors to model amplification through the crustal velocity gradient, to a standard B/C site condition, assuming that the near-surface high-frequency attenuation parameter is $\kappa_0 = 0.025$ s for this site class; the value of κ_0 is based on the findings of Yenier and Atkinson (2014). As noted earlier, any overall misfit of the assumed site model will map into source and path effects, as well as the constant calibration term. The trade-off between modeling parameters makes the ground-motion modeling ambiguous, obscuring the selection of the best-fitting parameter set (Babaie Mahani and Atkinson, 2012). In this study, therefore, we intend to determine a set of self-consistent modeling parameters that are well calibrated to observed ground motions in California for wide magnitude, distance and frequency ranges. We have chosen to make our best estimate of the model parameters wherever they can be objectively constrained, and cast the overall remaining misfit into a global calibration factor. It is important to recognize that a different self-consistent parameter set may result in a different stress model, and a slightly-different calibration factor. In particular, κ_0 trades off with the stress parameter, and there will also be interaction between the B/C crustal amplification function and the stress parameter. However, the impact of crustal amplification and κ_0 on the calibration factor would be relatively limited because the calibration factor is primarily controlled by low-frequency residuals (will be shown later) whereas the crustal amplification function and κ_0 mostly influence high-frequency amplitudes. Our chief aim in this paper is to derive a self-consistent parameter set that provides a reasonable model foundation; determining whether it is the optimal parameter set, or provides the best choice for each model component, is beyond our scope.

In stochastic simulations, the seismic energy defined by the *FAS* model (Equation 3.1) is combined with a random phase and distributed over a duration that is a function of magnitude and distance, in order to simulate the ground-motion time series (Boore, 2003). The ground-motion duration is given as the summation of source and path duration terms. In this study, we define the source duration as $1/f_0$, where f_0 is obtained from Equation 3.3. We use the path-duration model proposed by Boore and Thompson (2014), which is given as a function of rupture distance (D_{rup}). Note that we simulate

ground motions based on the effective distance (R). Therefore, we convert the nodal rupture distances of Boore and Thompson's path-duration model to effective distance, using the pseudo-depths (h) obtained from Equation 3.5 at each magnitude level, in order to express the path duration in terms of effective distance in simulations. This modification ensures that the synthetic time series attain ground-motion duration that is compatible with the path-duration model of Boore and Thompson (2014). In a recent study, Boore and Thompson (2015) re-evaluated their duration model using the effective distance metric and obtained a formulation similar to that adopted here. A summary of simulation parameters is presented in Table 3.1.

We perform equivalent point-source simulations for magnitudes from **M**3.0 to **M**7.5 and distances up to 400 km, in small increments of magnitude (Δ**M** = 0.05) and distance ($\Delta\log R$ = 0.05). For each magnitude-distance pair, we simulate ground motions for a number of $\Delta\sigma$ values ranging from 1 bar to 2000 bars. We generate 100 synthetic ground motions, using time-domain stochastic simulation method via SMSIM, for each combination of magnitude, distance and stress parameter. We calculate the geometric mean of *PSA* values from the simulated ground motions, for each combination. We follow the same procedure for both geometrical spreading rates: b_1 = -1.0 and b_1 = -1.3. We interpolate the simulated *PSA* values for the known magnitudes and distances of the selected records, in order to compare simulations against observed motions.

Table 3.1 Parameter values used for the equivalent point-source ground-motion simulation for California with SMSIM

Parameter	Value
Shear-wave velocity	$\beta = 3.7$ km/s
Density	$\rho = 2.8$ g/cm^3
Effective distance	$R = (D_{rup}^2 + h^2)^{0.5}$
Pseudo-depth	$\log h = \max(-0.05 + 0.15\mathbf{M}, -1.72 + 0.43\mathbf{M})$
Geometrical spreading	(i) $b_1 = -1.0$, $b_2 = -0.5$ and $R_t = 50$ km
	(ii) $b_1 = -1.3$, $b_2 = -0.5$ and $R_t = 50$ km
Quality factor	$Q = \max(100, 170.3f^{0.45})$
Site amplification (NEHRP B/C)	Table 4 of Atkinson and Boore (2006) Frequency-amplification pairs delimited by semicolons: 0.0001Hz-1; 0.1Hz-1.07; 0.24Hz-1.15; 0.45Hz-1.24; 0.79Hz-1.39; 1.38Hz-1.67; 1.93Hz-1.88; 2.85Hz-2.08; 4.03Hz-2.2; 6.34Hz-2.31; 12.5Hz-2.41; 21.2Hz-2.45; 33.4Hz-2.47; 82Hz-2.50
Kappa factor	$\kappa_0 = 0.025$ s
Source duration[*]	$1/f_0$ for the Brune model
Path duration[†]	Table 1 of Boore and Thompson (2014) Rupture distance-path duration pairs delimited by semicolons: 0km-0s; 7km-2.4s; 45km-8.4s; 125km-10.9s; 175km-17.4s; 270km-34.2s. Path duration increases with distance at a rate of 0.156s/km after the last nodal point.

[*] The source duration is defined as $0.5/f_a + 0.5/f_b$ for the double-corner frequency source model (Equation 3.11), where f_a and f_b are the corner frequencies.

[†] In simulations, the nodal rupture distances are converted to effective distance based on Equation 3.5 at each magnitude level.

3.4   Determination of stress parameter

The stress parameter, $\Delta\sigma$, (or the corner frequency, through Equation 3.3) is the key source parameter in stochastic point-source modeling. It controls the spectral shape at high frequencies (along with the site parameter κ_0). In this study, we fix κ_0 for NEHRP B/C sites at a commonly-determined value of $\kappa_0 = 0.025$ s (Yenier and Atkinson, 2014). This casts all remaining near-distance high-frequency shape effects into $\Delta\sigma$. Later, we check residuals to see if the frequency-dependence of spectral shape has been adequately captured.

Figure 3.5 shows the influence of stress and κ_0 parameters on the *FAS* models and the response spectra simulated from these models, for **M**4 and **M**6 events at $R = 10$ km. In this example, the ground-motion duration is fixed at 3.0 s and 5.5 s for **M**4 and **M**6 simulations, respectively, to isolate the effect of stress. As seen in Figure 3.5, spectral amplitudes are controlled by both magnitude and stress at high frequencies ($f > f_0$), as well as being influenced by κ_0. This provides great flexibility to vary high-frequency amplitudes in simulations. By modifying $\Delta\sigma$ for a specified seismic moment and κ_0, we can easily match the observed spectral amplitudes at high frequencies. However, there is no unique solution for the stress parameter because its value depends on the presumed attenuation model, due to the trade-off between earthquake source and attenuation (Boore et al., 2010; Yenier and Atkinson, 2014). This trade-off complicates the comparison of source spectra derived from different attenuation models or for different regions.

At low frequencies ($f < f_0$), the spectral amplitudes are primarily controlled by the seismic moment, which is pre-set through **M**. The stress parameter has no effect on the *FAS* model and has a limited effect on the response spectrum at low frequencies, as seen in Figure 3.5. This restricts the ability to calibrate simulated response spectrum at low frequencies by varying the stress parameter.
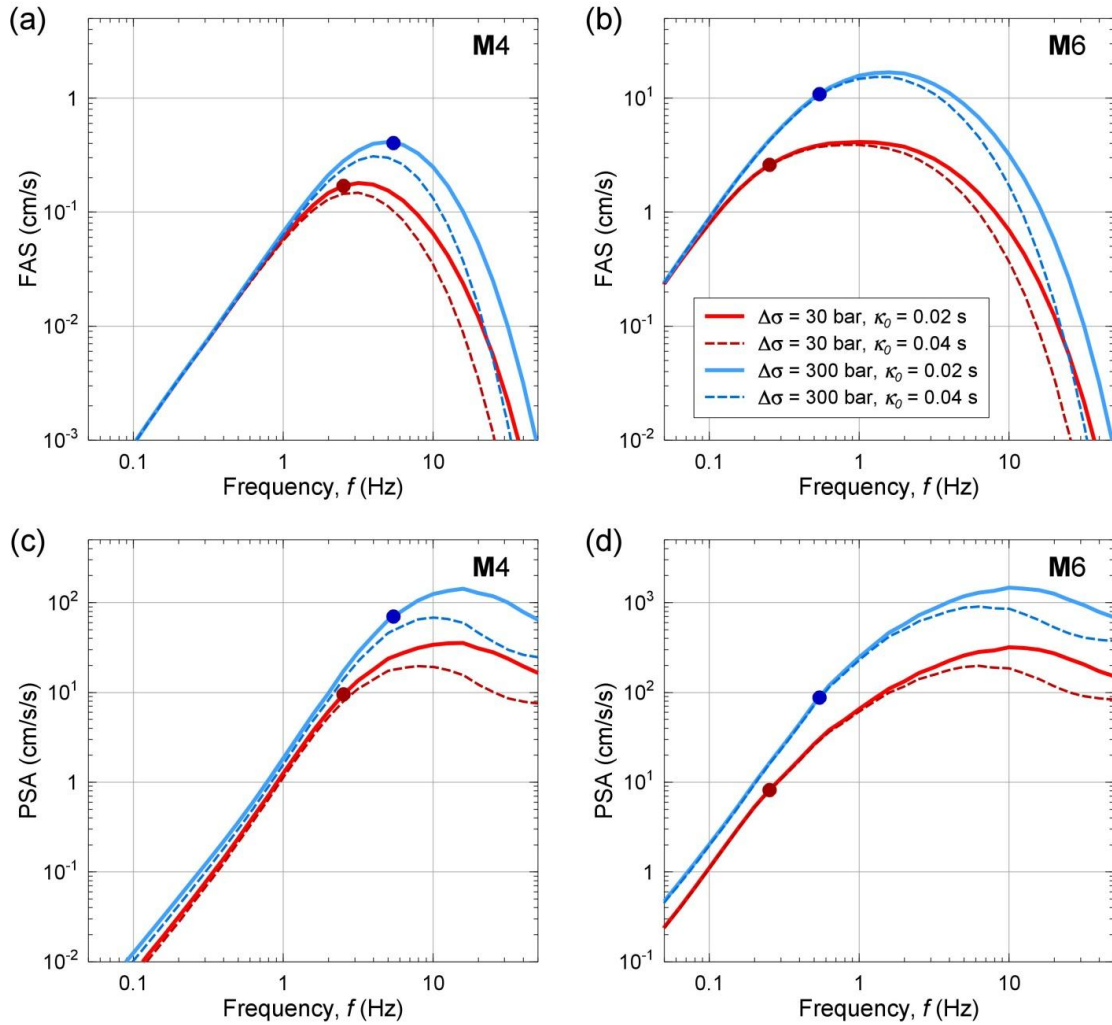
Figure 3.5 Influence of the stress ($\Delta\sigma$) and kappa (κ_0) parameters on Fourier and response spectra, for **M**4 (left) and **M**6 (right) earthquakes at $R = 10$ km. Top row shows the *FAS* models determined based on Equation 3.1 for $b_1 = -1.0$ and bottom row shows the geometric mean of pseudo-spectral accelerations (*PSA*) for 100 time-domain simulations based on the *FAS* models shown in the top row. Circles indicate corner frequencies of the associated Brune models.

To ensure a model calibration that is consistent over all frequencies we use spectral shape, rather than absolute spectral amplitude, to determine the stress parameter. This approach is equivalent to finding the corner frequencies of study events. Simulations with the shape-based stress parameter can be scaled by a constant factor (which is input to

SMSIM) to generate synthetic ground-motion time series that are compatible with the observed response spectra, over a wide frequency range, including at low frequencies. This scaling by a constant factor is equivalent to changing the value of C in Equation 3.2.

Figure 3.6 illustrates an example for the implementation of this approach for the 2004 **M**6.0 Parkfield earthquake. Residuals, defined as log(*PSAobs*/*PSAsim*), where *PSAobs* and *PSAsim* denote observed and simulated *PSA*, respectively, are plotted for simulations derived for b_1 = -1.3 and different $\Delta\sigma$ values (with the fixed κ_0 = 0.025 s and Q model). As seen in the figure, residuals decrease with increasing stress, but the effect is mostly prominent at high-frequencies. For $\Delta\sigma$ = 225 bars, simulations attain residuals around zero for f > 0.7 Hz, and the mean residual achieves a minimum. This stress corresponds to the value that would be generally inferred from high-frequency spectral amplitudes for the presumed attenuation model (b_1 = -1.3). However, it is critical to note that the simulations cannot be calibrated at f < 0.7 Hz by varying the stress parameter. Regardless of the selected stress, there is a mismatch in the amplitude over the low-frequency portion of the spectrum, which is controlled by the seismic moment. Thus the determined stress parameter is not compatible with the seismic moment, in terms of spectral shape.

A better characterization of the source is obtained by selecting the stress parameter such that the simulated and observed spectra attain similar shapes for a wide frequency range, then calibrating the overall amplitude level to match the moment constraint. To this end, we select $\Delta\sigma$ based on the minimum standard deviation of residuals, over a wide frequency range. In Figure 3.6, for example, we note that residual values have little trend in frequency for $\Delta\sigma \sim$ 20 bars. This stress provides the minimum standard deviation of residuals, among the trial $\Delta\sigma$ values, ensuring that the simulated and observed spectra have similar shapes at f > 0.1 Hz. However, there is a mean residual of 0.65 log units for this case. Thus, we must adjust the constant C in SMSIM by a factor of $10^{0.65}$ = 4.47, assuming a stress of $\Delta\sigma$ = 20 bar along with all other parameters listed in Table 3.1 (b_1 = -1.3), in order to simulate ground motions that are compatible with the observed response spectra, both in shape and amplitude, at frequencies f > 0.1 Hz (for this specific earthquake). The calibration factor applied to SMSIM (referred as C_{sim} hereafter) enables scaling of the entire Fourier spectrum by the same amount at all frequencies. This is

preferable to calibrating the amplitudes by varying the stress parameter, in our view, because the stress parameter has limited effect on spectral amplitudes at low frequencies.
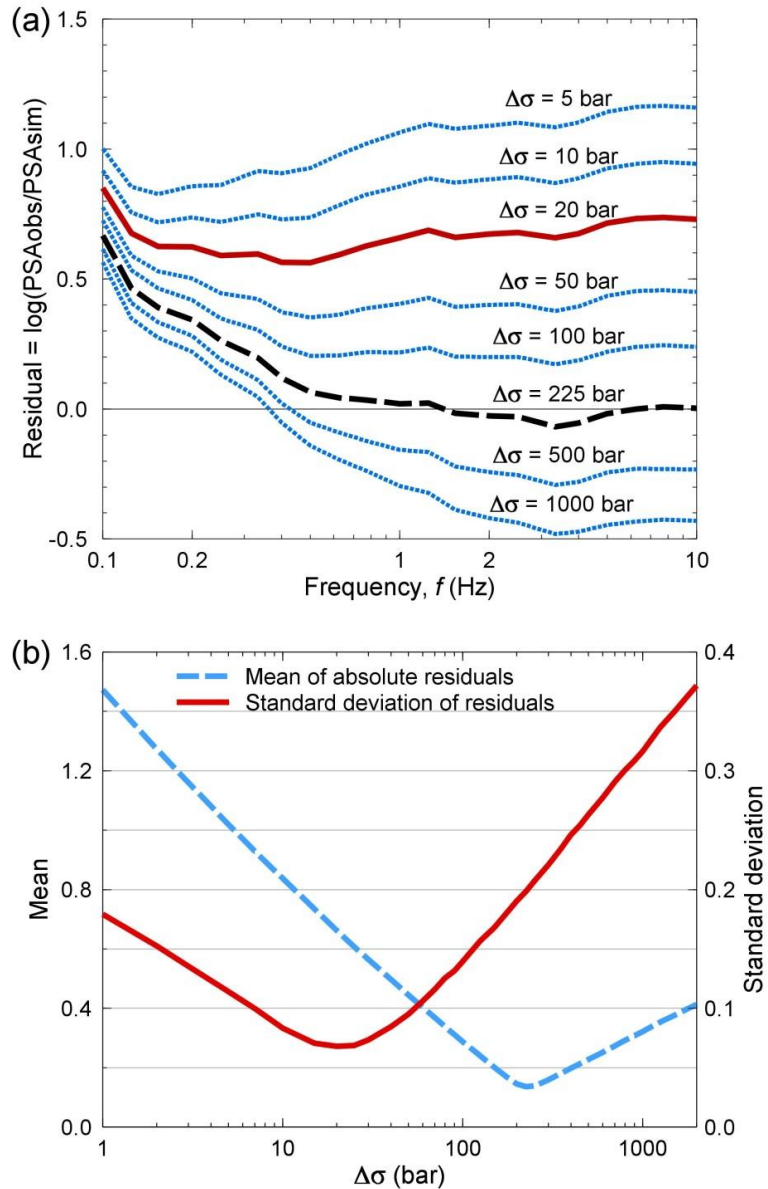
Figure 3.6 Determination of the stress parameter ($\Delta\sigma$) for the 2004 **M**6.0 Parkfield earthquake. Graph (a) shows residuals for simulated *PSA* ($b_1 = -1.3$), averaged over all distances at each frequency, for different values of $\Delta\sigma$. Graph (b) presents the standard deviation of residuals (solid line) and the mean of their absolute values (dashed line) as a function of $\Delta\sigma$.

Following this approach, we determine the stress parameter and calibration factor to match the observed spectral amplitudes for each study earthquake. Note that C_{sim} is primarily controlled by the low-frequency residuals, due to the limited effect of $\Delta\sigma$ at these frequencies. Therefore, noise-contamination that is common in low-frequency amplitudes can yield unreliably high calibration factors, particularly for small events. To reduce the impact of such effects, we consider the minimum usable frequencies (f_{min}) given in the NGA-West2 database for analysis. We also impose a lower boundary (f_{lb}) for the usable frequency band as:

$$log f_{lb} = \max[-1, \ (3 - \mathbf{M})/3] \qquad (3.8)$$

Equation 3.8 is defined such that it generally provides more conservative frequencies than f_{min} values listed in the NGA-West2 database for $\mathbf{M} < 5$, as seen in Figure 3.7. For each record, we consider the *larger* of f_{min} as given by the NGA-West2 database or f_{lb} obtained from Equation 3.8, to define the lower end of the frequency band used for analysis. We further constrain the frequency band used for analysis at an upper boundary of $f_{ub} = 10$ Hz, to limit the trade-off between the $\Delta\sigma$ and κ_0 parameters. These constraints are helpful in ensuring robust determination of the calibration constant. As seen in Figure 3.7, the selected frequency band is wide enough to capture the fundamental source characteristics for most earthquakes, as compared to the Brune corner frequencies (f_0) for a typical stress parameter of $\Delta\sigma = 100$ bar.

Figure 3.8 shows the $\Delta\sigma$ values determined from the study earthquakes as a function of focal depth (d) and magnitude, assuming $b_1 = -1.3$. The $\Delta\sigma$ values obtained for $b_1 = -1.0$ are nearly identical to those determined for $b_1 = -1.3$ for almost all events (and therefore are not shown). This is because the use of the observed spectral shape to define stress breaks the trade-off between the $\Delta\sigma$ and b_1 terms. It is interesting and satisfying that the use of spectral shape results in stress parameters that are consistent with widely-quoted values for California events from the classic literature on stochastic methodologies (e.g. Hanks and McGuire, 1981; Boore, 2003). However, we note that the trade-off between stress and geometric spreading now transforms to a C_{sim}-b_1 trade-off (discussed later, Figure 3.12). This is an advantageous change, because both the C_{sim} and b_1 terms affect

the ground-motion spectrum at all frequencies by the same amount, whereas $\Delta\sigma$ primarily affects high frequencies.
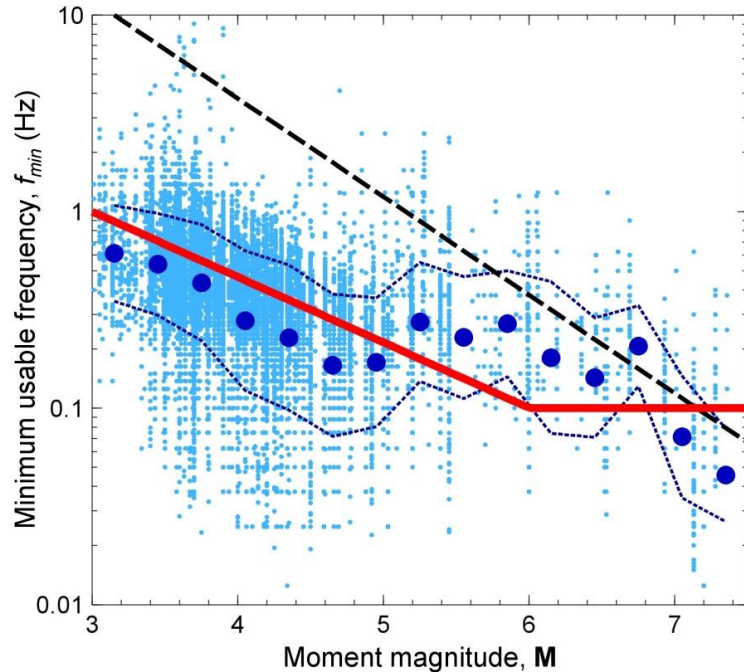
Figure 3.7 Minimum usable frequencies (f_{min}) reported in the NGA-West2 database for the selected records (small circles). Large circles show the geometric mean of f_{min} values for evenly-spaced magnitude bins and dotted lines indicate one standard deviation about the mean. Solid line depicts the lower boundary of usable frequency band (f_{lb}) considered for the analysis. For each record, we consider the larger of f_{min} or f_{lb} for analysis. The dashed line features the corner frequency of Brune model for $\Delta\sigma = 100$ bar.

In Figure 3.8, the stress parameter shows an increasing trend with focal depth, and this trend appears to be magnitude-dependent. For **M**3-**M**4, the mean stress increases from ~5 bars at depths $d < 5$ km to ~120 bars at depths $d > 10$ km. For **M** > 6, however, stress increases from ~50 bars at $d < 5$ km to ~160 bars at $d > 10$ km, on average. This suggests that the increasing trend of stress with depth weakens for large events (i.e., the stress parameter becomes less sensitive to the depth with increasing magnitude), possibly because the larger magnitude events are rupturing a significant crustal thickness. We parameterize the mean stress for California earthquakes as:

$$log\Delta\sigma = a_0 + \min[0, \ a_1(d-12)] \tag{3.9}$$

where d is the focal depth in km and a_0 and a_1 are model coefficients. In Equation 3.9, the hinge depth, beyond which $\Delta\sigma$ is assumed to be constant, is chosen as $d = 12$ km based on the inspection of $\Delta\sigma$ residuals for alternative hinge depths.
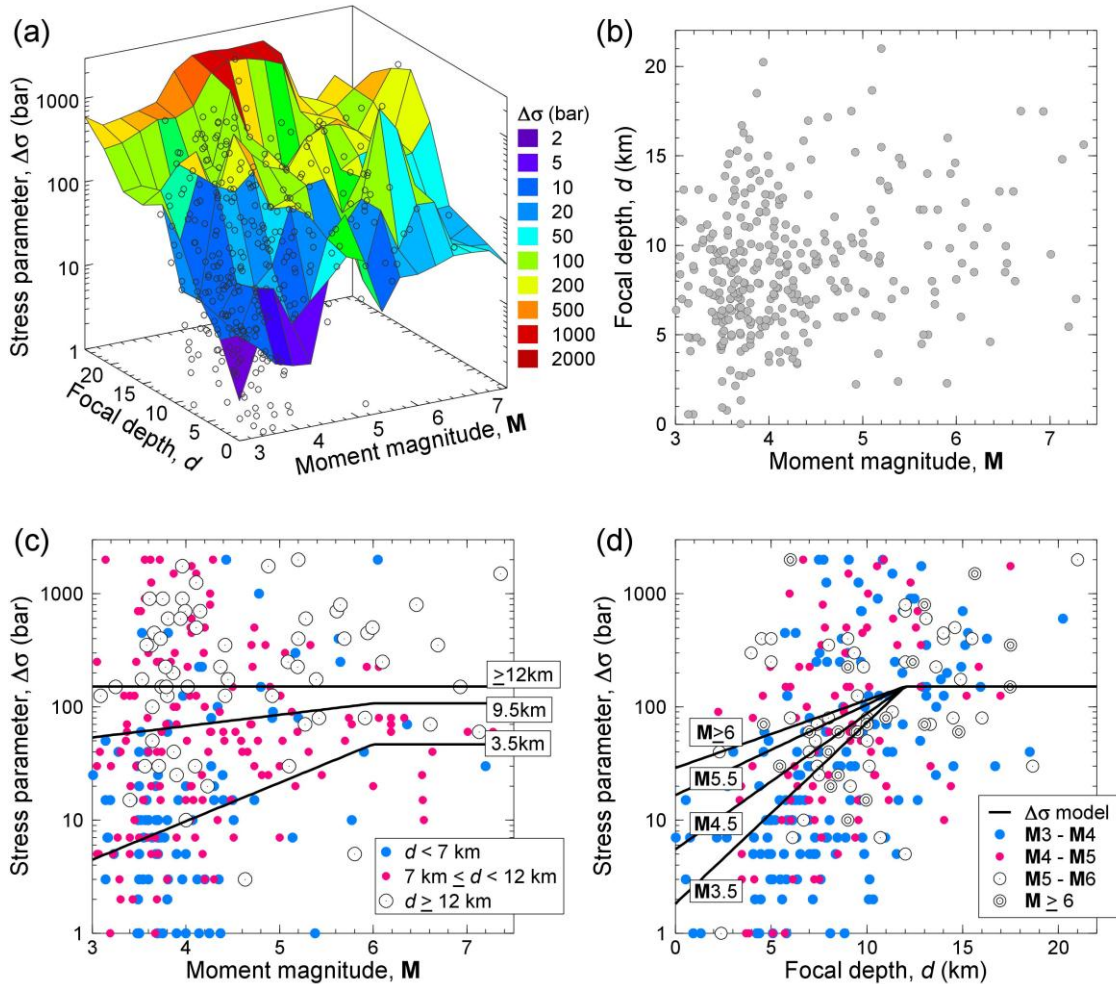
Figure 3.8 Dependence of the stress parameter ($b_1 = -1.3$) on magnitude and focal depth shown in 3-dimensions (a). Graphs (b) through (d) show the projection of this information in 2-dimensional space. Solid lines in (c) and (d) represent the stress model (Equation 3.9) evaluated for different magnitudes and focal depths (shown in boxes).

We cluster the stress parameters obtained from study events into four magnitude bins (**M**3-**M**4, **M**4-**M**5, **M**5-**M**6 and **M**6-**M**7.5), and determine a_0 and a_1 from regression analysis for each magnitude bin. Figure 3.9 shows the variation of model coefficients as a function of magnitude. The a_0 term is relatively independent of magnitude, attaining $a_0 =$ 2.18 (i.e., $\Delta\sigma$ = 150 bar) over all magnitudes, on average. There is a suggestion in Figure 3.9 that $\mathbf{M} \geq 6$ events attain slightly lower a_0 than that of **M**4-**M**6 events. This is in accord with the findings of Atkinson and Silva (1997) and Boore et al. (2014a) that $\Delta\sigma$ shows a decreasing trend with magnitude for $\mathbf{M} > 5.5$ in California. However, we ignore this effect in our $\Delta\sigma$ model (i.e., $a_0 = 2.18$ for all **M**) because the uncertainty in a_0 is larger than the variation of a_0 between different magnitude bins.

In Figure 3.9, the a_1 term shows a decreasing trend with increasing magnitude. This supports the observations made in Figure 3.8 that the depth dependency of stress parameter weakens with increasing magnitude. We define a_1 as:

$$a_1 = \max[0.06, \ 0.3 - 0.04\mathbf{M}] \tag{3.10}$$

The estimates of the derived $\Delta\sigma$ model are also shown in Figure 3.8. The mean residuals between the observed and estimated $\Delta\sigma$ values attain values around zero, as illustrated in Figure 3.10. Overall, the $\Delta\sigma$ model provides good agreement with the values determined from California events based on the inferred spectral shape.
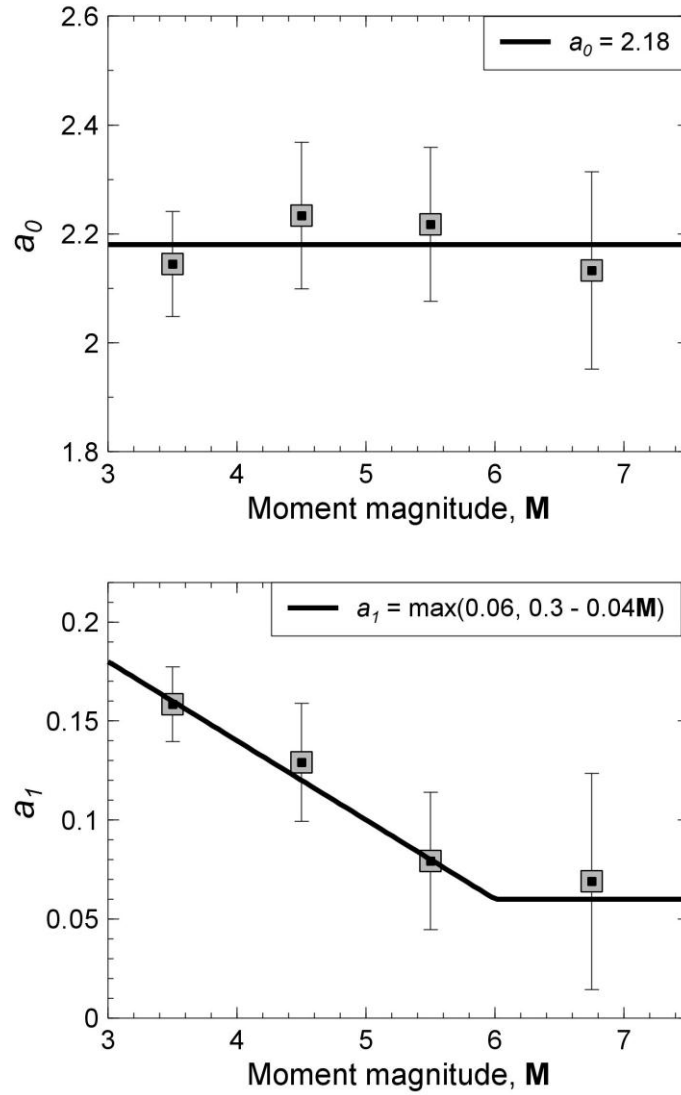
Figure 3.9 Coefficients a_0 and a_1 obtained from regression of the $\Delta\sigma$ values ($b_1 = -1.3$) based on Equation 3.9, for four magnitude bins (**M**3-**M**4, **M**4-**M**5, **M**5-**M**6 and **M**6-**M**7.5). Error bars indicate the standard error about the determined coefficients, which are plotted at the center magnitude of each bin.
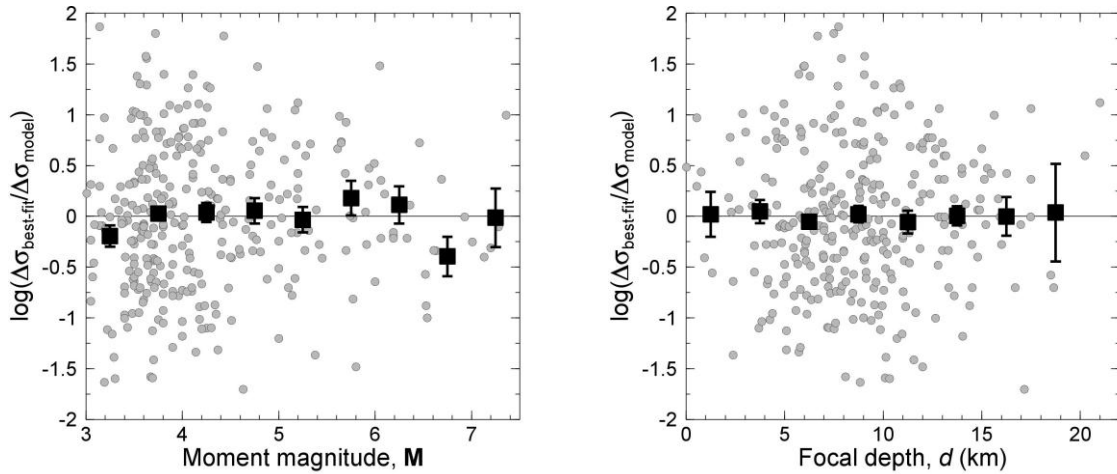
Figure 3.10 Residuals between the $\Delta\sigma$ values ($b_1 = -1.3$) obtained from California events and the estimates of the $\Delta\sigma$ model (Equation 3.9). Squares show mean of residuals determined for evenly-spaced magnitude and depth bins. Error bars represent the standard error about the mean residual.

Due to the broken trade-off between the $\Delta\sigma$ and b_1 terms, the stress model applies to both $b_1 = -1.0$ and $b_1 = -1.3$, but requires different values of C_{sim} to match the observed amplitudes. In other words, $\Delta\sigma$ is controlling only the spectral shape, while C_{sim} scales the absolute amplitudes. This contrasts with the formulation in Yenier and Atkinson (2014) in which stress was used as a scaling parameter in combination with b_1. Thus, the values for stress between the two studies cannot be directly compared, unless these differences are factored into the comparison.

Figure 3.11 shows corner frequencies (f_0) determined from Equation 3.3, using the stress parameters obtained from study events. For most of the study events, f_0 falls into the frequency band considered in the analysis. This indicates that the selected frequency band is wide enough to capture the source spectral shape both at low ($f < f_0$) and high ($f > f_0$) frequency ranges, except $\mathbf{M} > 7.0$ earthquakes, for which the stress parameter is primarily controlled by the high-frequency spectral shape. Note that deep events attain higher f_0 values than those of shallow events due to the increase of $\Delta\sigma$ with depth. This effect is well captured by the f_0 values determined from the $\Delta\sigma$ model. In Figure 3.11, the logf_0-vs.-$\mathbf{M}$ line attains a slope of -0.5 for $d \geq 12$ km. This implies that deep earthquakes in

California are self-similar, with constant mean stress (Δσ = 150 bar). The logf_0-vs.-**M** line attains milder slopes with decreasing focal depth because the Δσ model increases with magnitude up to **M**6 for d < 12 km, implying a break in self-similarity of small-to-moderate earthquakes at shallow depths. This is consistent with the findings of previous studies for eastern North America (e.g., Atkinson, 1993; Mereu et al., 2013).
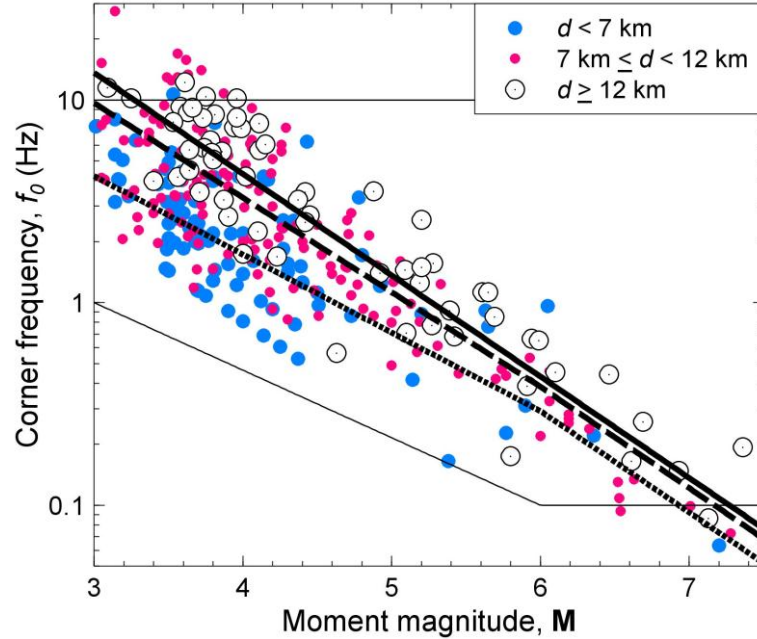
Figure 3.11 Corner frequencies (f_0) determined from the shape-based stress parameters for b_1 = -1.3 (circles). Heavy lines indicate f_0 obtained from the estimates of the stress model (Equation 3.9) for d = 3.5 km (dotted line), d = 9.5 km (dashed line), and $d \geq 10$ km (solid line). Thin lines indicate the lower and upper boundaries of the frequency band (f_{lb} and f_{ub}) considered in the analysis.

3.5 Simulation calibration factor, C_{sim}

For each earthquake, we determine the simulation calibration factor (C_{sim}) based on the average residual obtained for the associated stress parameter, as described in the previous section. Figure 3.12 plots the C_{sim} factors obtained for alternative geometrical spreading rates, as a function of magnitude. Although the calibration factors show a large scatter, the dependence of their values on the presumed attenuation rate (b_1) is apparent.

Importantly, the average calibration factors determined for evenly-spaced magnitude bins show no discernible magnitude-dependent trends for either value of b_1. Considering all study events, the average calibration factor (as a multiplicative factor on the constant C in Equation 3.2) is $C_{sim} = 1.08$ for $b_1 = -1.0$ and $C_{sim} = 3.16$ for $b_1 = -1.3$. This suggests that ground motions simulated based on the $1/R$ spreading match the observed spectral amplitudes well on average, requiring practically no additional calibration. This accords with the findings of Raoof et al. (1999), who suggested a geometrical spreading of $R^{-1.0}$ at distances < 40 km, in southern California. It is also consistent with previous point-source stochastic modeling in California by Atkinson and Silva (2000), and the recent findings of Boore et al. (2014a). By contrast, ground motions simulated based on the $b_1 = -1.3$ model, which is suggested by recent empirical studies (Babaie Mahani and Atkinson, 2012; Yenier and Atkinson, 2014; Atkinson et al., 2014), require a calibration factor of $C_{sim} = 3.16$ to match the observed spectral amplitudes. When the attenuation rate is changed from $b_1 = -1.0$ to $b_1 = -1.3$, the calibration factor increases from $C_{sim} = 1.08$ to $C_{sim} = 3.16$ to balance the average amplitude difference between the geometrical spreading functions (Figure 3.4), in order to match the observed spectral amplitudes at distance. Considering this, it is tempting to conclude that the $1/R$ spreading model must be more nearly correct. However, the geometrical spreading model can in reality be verified only by evaluation of distance-dependent trends in residuals. We address this in the next section.
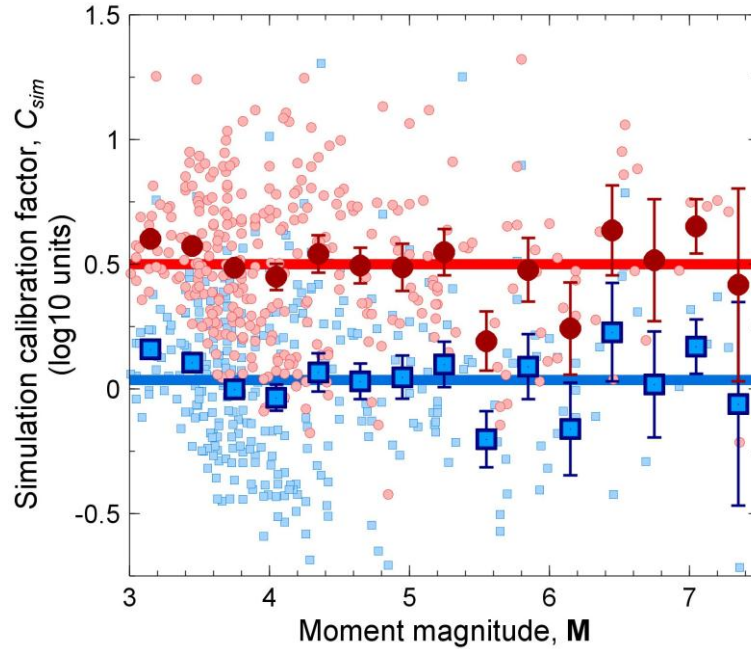
Figure 3.12 Simulation calibration factors (C_{sim}) determined for the study events based on average residuals obtained from simulated PSA, for $b_1 = -1.0$ (small squares) and $b_1 = -1.3$ (small circles). Large squares and circles represent the mean values of C_{sim} calculated for evenly-spaced magnitude bins, for $b_1 = -1.0$ and for $b_1 = -1.3$, respectively. Error bars indicate standard error about the mean values. The heavy lines indicate C_{sim} values averaged over all magnitudes.

3.6 Assessment of alternative geometrical spreading models

We assess the performance of the alternative geometrical spreading models in a forward modeling context. We assume the derived average stress model (Equation 3.9) and calibration factors ($C_{sim} = 1.08$ for $b_1 = -1.0$ and $C_{sim} = 3.16$ for $b_1 = -1.3$), with other parameters as listed in Table 3.1, to simulate ground motions for the known magnitudes and distances of all records. We inspect the residuals of simulated *PSA* for the two geometric spreading models, as a function of distance, for different magnitude ranges. Figure 3.13 shows the average residuals determined for logarithmically-spaced distance bins, for frequencies 0.5 Hz, 1 Hz and 5 Hz. For **M** < 5.5 earthquakes, the residuals increase with decreasing distance for $b_1 = -1.0$, particularly within the first 50 km.

However, the $b_1 = -1.3$ model shows little or no distance-dependent residual trends for the same magnitude and distance ranges. As an exception, the $b_1 = -1.0$ model results in better mean residuals than the $b_1 = -1.3$ model for **M**4.5-**M**5.5 events at distances less than 10 km. However, the $b_1 = -1.0$ model shows persistent distance-dependent residual trends at 10 km $< D_{rup} < 50$ km, particularly for low and intermediate frequencies. This observation strongly supports the $b_1 = -1.3$ model in preference to $b_1 = -1.0$. We find this compelling evidence in favor of $b_1 = -1.3$, because residuals at $D_{rup} < 50$ km are primarily controlled by the geometrical spreading rate, b_1, for small magnitude events.

As seen in Figure 3.13, the discrepancy in residual trends between the $b_1 = -1.0$ and $b_1 = -1.3$ models decreases with increasing magnitude, because the pseudo-depth (h) increases with magnitude, causing attenuation models with different b_1 values to attain similar shapes for large events (Figure 3.4; note that the amplitude difference between the saturated models maps into the calibration factor, C_{sim}, so has no effect on distance trends). This observation indicates that both $b_1 = -1.0$ and $b_1 = -1.3$ models could be used for **M** > 5.5 events, interchangeably. For smaller earthquakes, however, the $b_1 = -1.3$ model provides a better description of the observed amplitude decay.

We note in Figure 3.13 that the low-frequency residuals generally attain negative values for **M** > 5.5, regardless of the value of b_1. We surmise that this is due to the empirically-observed spectral sag in the apparent source spectra relative to the assumed single-corner-frequency (SCF) Brune model (Atkinson and Silva, 1997; 2000). The match of simulations to observations can be improved by replacing the SCF Brune source model by a double-corner-frequency source model that features a spectral sag at intermediate frequencies in the Fourier domain. In a recent study, Boore et al., (2014a) proposed a generalized additive double-corner-frequency (DCF) source model that is compatible with the Brune model at low and high frequencies but shows a magnitude-dependent spectral sag at intermediate frequencies.
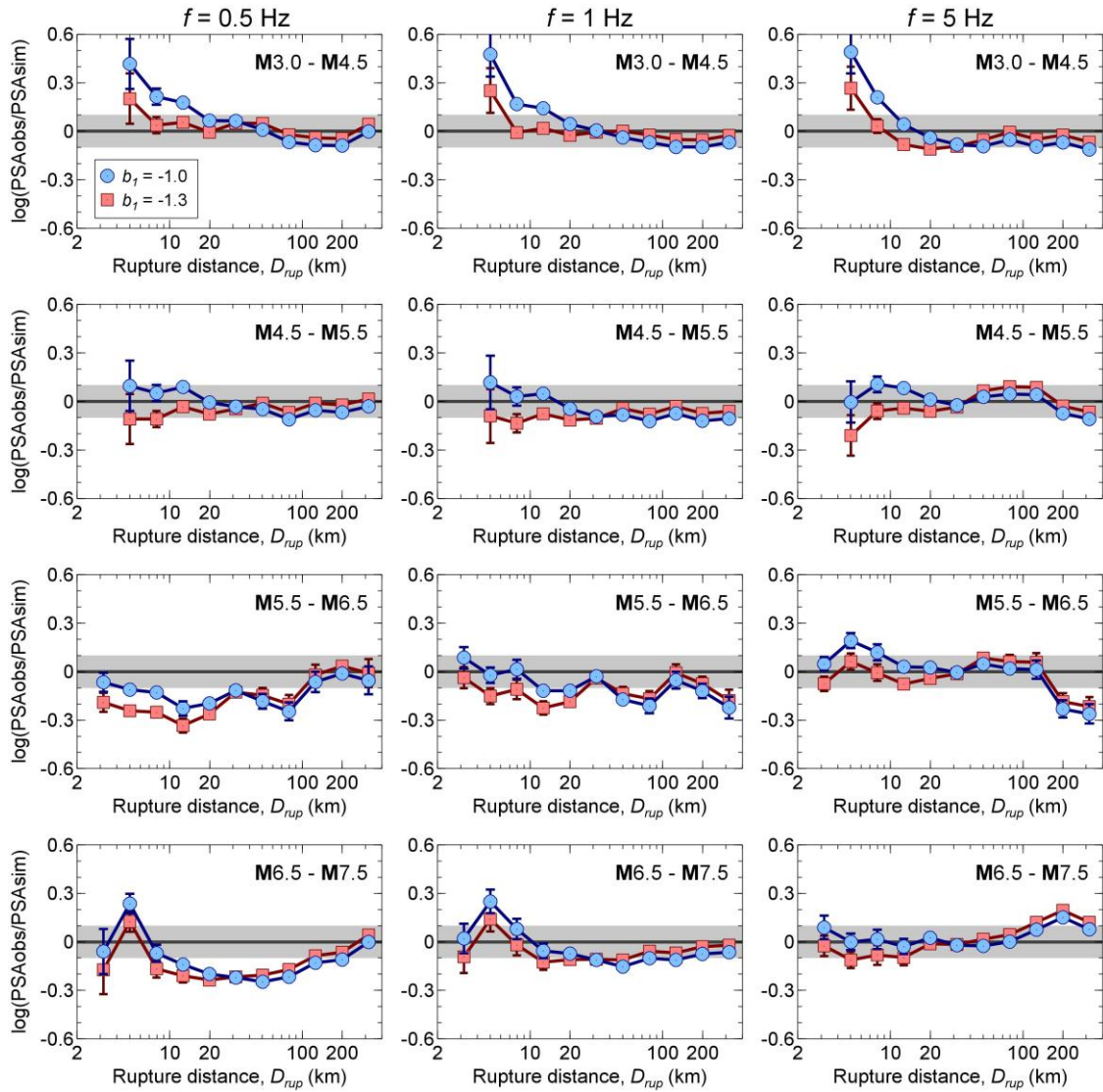
Figure 3.13 Residuals for simulated *PSA* based on the single-corner-frequency Brune source model (C_{sim} applied), for b_1= -1.0 (circles) and b_1 = -1.3 (squares), for different magnitude bins (rows). Symbols represent residuals averaged over logarithmically-spaced distance bins for frequencies 0.5 Hz (left), 1 Hz (middle) and 5 Hz (right). Error bars indicate standard error about the mean residuals. The shaded area illustrates ±0.1 log units about zero-residual line.

The DCF source model is given as (Boore et al., 2014a):

$$A_0(M_0, f) = CM_0(2\pi f)^2 \left[\frac{1 - \varepsilon}{1 + (f/f_a)^2} + \frac{\varepsilon}{1 + (f/f_b)^2} \right] \tag{3.11}$$

where f_a and f_b are the two corner frequencies and ε is a weighting parameter that controls the depth of the spectral sag between the corner frequencies. The corner frequencies are given as $\log f_a = 2.181 - 0.496\mathbf{M}$ (Atkinson and Silva, 2000) and $f_b = [(f_0^2 - (1 - \varepsilon)f_a^2)/\varepsilon]^{0.5}$ (Boore et al., 2014a), where f_0 is determined from Equation 3.3.

We develop an ε model for California earthquakes based on the residuals obtained from simulations. We define $\log\varepsilon$ as a linear function of magnitude and constrain its value at $\log\varepsilon = 0$ for $\mathbf{M} < 4$. We test alternative slopes for the $\mathbf{M}$-dependence of $\log\varepsilon$ and simulate ground motions using the DCF source model for each trial, with all other modeling parameters being fixed at the same values used for the SCF simulations. The optimal weighting parameter formulation is:

$$\log\varepsilon = \begin{cases} 0 & \mathbf{M} < 4 \\ 1.2 - 0.3\mathbf{M} & \mathbf{M} \geq 4 \end{cases} \tag{3.12}$$

in order to minimize bias for $\mathbf{M} > 5.5$ at low frequencies. The derived ε model is self-consistent with all other modeling parameters used in SCF simulations, including the $\Delta\sigma$ model (Equation 3.9). Figure 3.14 shows the effect of the DCF source model on the average residuals for different magnitude ranges. The residuals suggest that the DCF source model with ε as given in Equation 3.12 generally improves the performance of the equivalent point-source simulations, extending their applicability to larger events and lower frequencies. However, there is a significant (factor of 2.0 to 2.5) underprediction of amplitudes (even for the $b_1 = -1.3$ model) at low-to-intermediate frequencies at $D_{rup} \approx 5$ km for $\mathbf{M} > 6.5$ events. These residuals are primarily caused by the elevated ground-motion amplitudes of the 1994 $\mathbf{M}$6.7 Northridge earthquake at close distances. We believe that these enhanced amplitudes are due to other effects not considered in an equivalent point-source model, such as rupture directivity and hanging-wall effects. This is an unresolved limitation of the model.
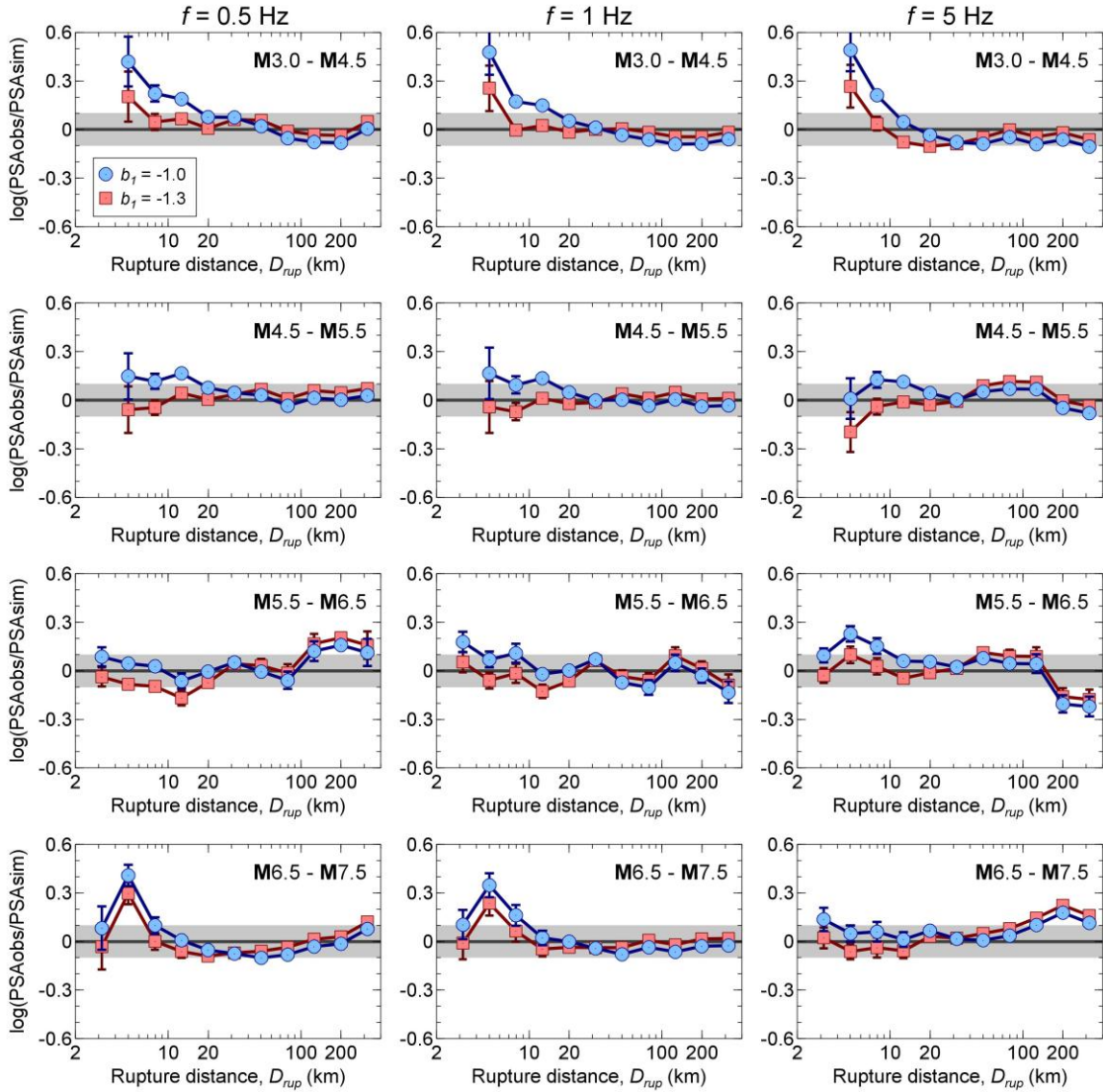
Figure 3.14 Residuals for simulated *PSA* based on the double-corner-frequency source model (C_{sim} applied), for b_1= -1.0 (circles) and b_1 = -1.3 (squares), for different magnitude bins (rows). Symbols represent residuals averaged over logarithmically-spaced distance bins for frequencies 0.5 Hz (left), 1 Hz (middle) and 5 Hz (right). Error bars indicate standard error about the mean values. The shaded area illustrates ±0.1 log units about zero-residual line.

It is worth noting that our ε model implies a sag that is less deep than that proposed by Atkinson and Silva (2000) and Boore et al. (2014a), although all three models were derived based on the analysis of California earthquakes. The discrepancy may be related

to the differences in the assumed path duration models between the studies. Both Atkinson and Silva (2000) and Boore et al. (2014a) modeled the path duration as $0.05R$, whereas we adopt the more recent path duration model proposed by Boore and Thompson (2014) in this study. The former gives significantly shorter duration than that suggested by Boore and Thompson (2014). If we used $0.05R$ to model the path duration, we would obtain higher spectral amplitudes in our SCF simulations, and our residuals would move towards more negative values. Therefore, we would require larger ε values to balance this increased discrepancy. This explains the difference in ε models between this study and others. It also suggests a further avenue that could be explored in optimizing the fit of simulations to observations. In this study, we have chosen to make our best estimate of the actual model parameters (e.g., pseudo-depth, Quality factor and duration) wherever they can be objectively constrained, and cast all remaining misfit into a global calibration constant. We believe this is the most transparent choice. However, an alternative approach would be to use duration as a possible calibration parameter.

We further investigate the adequacy of the alternative geometrical spreading models in order to put the observed distance-dependent residual trends on a statistical footing. In this respect, we perform a standard t-test for the significance of the residual trends obtained from the DCF simulations at each frequency, for evenly-spaced magnitude bins ($\Delta\mathbf{M} = 0.5$). Figure 3.15 plots the magnitude-frequency combinations that show a statistically-significant trend in residual slope (at probability level, $p < 0.01$) within the first 50 km, for $b_1 = -1.0$ and $b_1 = -1.3$. The $b_1 = -1.0$ model yields distance-dependent residual trends that are clearly significant at most $\mathbf{M}$-f combinations. By contrast, the $b_1 = -1.3$ model shows distance-dependent residual trends for a much smaller number of combinations, and is clearly superior for small events, which we consider most diagnostic due to the lack of trade-off with the saturation term.
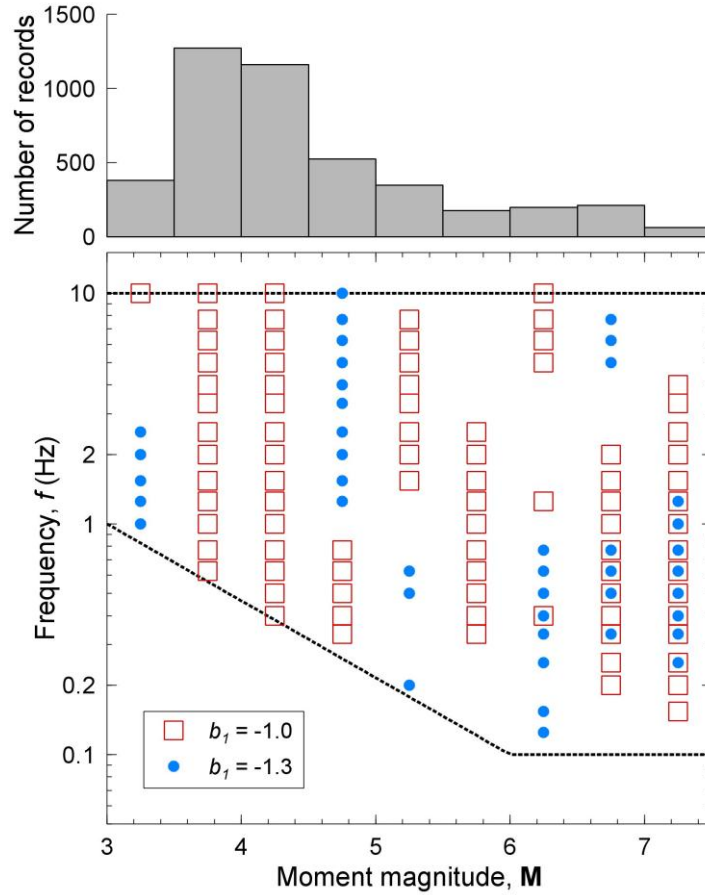
Figure 3.15 Magnitude-frequency pairs of residuals from DCF simulations that show statistically significant distance dependence (at probability level, $p < 0.01$) within the first 50 km, for $b_1 = -1.0$ (squares) and $b_1 = -1.3$ (circles). Dotted lines indicate the lower and upper boundaries of the frequency band (f_{lb} and f_{ub}) considered in analysis. The histogram of the usable ground motions ($f = 1$ Hz) within the first 50 km is shown in the top graph.

We determine a total score for each geometrical spreading model based on the weighted-sum of the **M**-f combinations that pass the statistical t-test, with weights being based on the number of observations in each **M**-f bin. We observed that the $b_1 = -1.0$ model passes the test 30% of the time at a probability level of $p < 0.01$, while the $b_1 = -1.3$ model passes the test 82% of the time for the same probability level. Similar observations are also made when the t-test is repeated for other probability levels (e.g., for $p < 0.05$, the $b_1 = -1.0$ and $b_1 = -1.3$ models pass the test 23% and 71% of the time, respectively). This conclusion is in accord with the observations made in Figures 3.13 and 3.14.

On balance, we conclude that the geometrical spreading in California is best modeled as $R^{-1.3}$ at distances less than 50 km, and $R^{-0.5}$ at further distances. This agrees with the findings of recent empirical studies (Babaie Mahani and Atkinson, 2012; Yenier and Atkinson, 2014; Atkinson et al. 2014). However, we acknowledge that a 1/R model at <50 km would also work relatively well, although it would result in significant underprediction of low-to-intermediate frequency amplitudes for $\mathbf{M} < 4.5$ events at $D_{rup} <$ 20 km (as much as a factor of three), as seen in Figure 3.14.

In Figure 3.16, we illustrate average residuals for simulated *PSA* based on both the SCF and DCF source models and $b_1 = -1.3$ (C_{sim} applied), as a function of frequency. The SCF source model exhibits frequency-dependent residual trends, especially for $\mathbf{M} > 5.5$. This suggests that the SCF source model is deficient in terms of replicating the observed spectral shape of ground motions in California, particularly for moderate-to-large magnitude earthquakes. The frequency-dependence of residuals reduces when the DCF source model is used (with the weighting parameter given in Equation 3.12). The residuals obtained from DCF simulations generally attain values within the ±0.1 log-units band at frequencies $f > 0.2$ Hz, but still show a slight frequency-dependent trend at high frequencies for some magnitude bins.
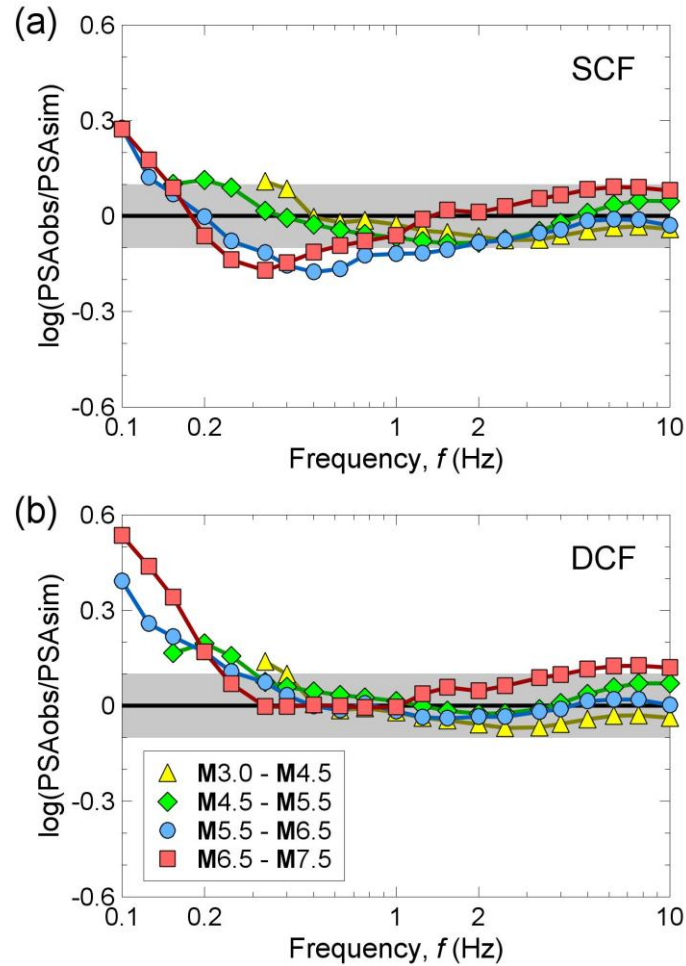
Figure 3.16 Residuals for simulated *PSA* based on the single- (top) and double-corner-frequency (bottom) source models (C_{sim} applied), for $b_1 = -1.3$. Symbols represent residuals averaged over all distances for different magnitude ranges. The shaded areas illustrate ±0.1 log units about zero-residual line.

For $f < 0.2$ Hz, DCF simulations result in residuals greater than 0.1 log-units, and the bias increases noticeably with decreasing frequency, regardless of the magnitude. To delve deeper into these effects, we examine the frequency-dependent attributes of residuals for different V_{S30} and distance ranges, as shown in Figure 3.17. Recall that we corrected observed motions to NEHRP B/C site class based on the site effects model of Boore et al. (2014b), and performed simulations for the same site class using site amplification factors of Atkinson and Boore (2006). In Figure 3.17, we observe that the residuals show frequency-dependent trends similar to those seen in Figure 3.16, regardless of the site

condition. This indicates that the residual trends are not originating from site effects. On the other hand, the distance range appears to have at least some effect on the frequency-dependence of the residuals at $f < 0.2$ Hz. At high frequencies, average residuals attain near zero values for all site conditions, but show a slight distance-dependent trend at $f > 5$ Hz. This suggests that the selected site amplification and κ_0 parameter (0.025 s) are reasonable; however, the Quality factor could be modified slightly to reduce the distance dependence of the high-frequency residuals at far distances. For example, an increase of the power of frequency in Equation 3.7 from 0.45 to 0.47 could reduce the residuals by 0.05 and 0.1 log-units at $f = 10$ Hz, for distances 150 km and 300 km, respectively. At low frequencies ($f < 0.2$ Hz for SCF model and $f < 0.4$ Hz for DCF model), average residuals increase with decreasing frequency for all distance ranges, with the trends being strongest at the largest distances. This may reflect inherent deficiencies in treating long-period motions, which may be quite coherent, as a stochastic process. The dependence of the strength of the effect on distance suggests that there is both a source and a path component to this problem. Note that the residuals obtained from SCF simulations show weaker frequency-dependent trends than do the DCF simulations at low frequencies in Figure 3.17, because the opposite signed-residuals (Figure 3.16.a) balance out when they are averaged over all magnitudes.
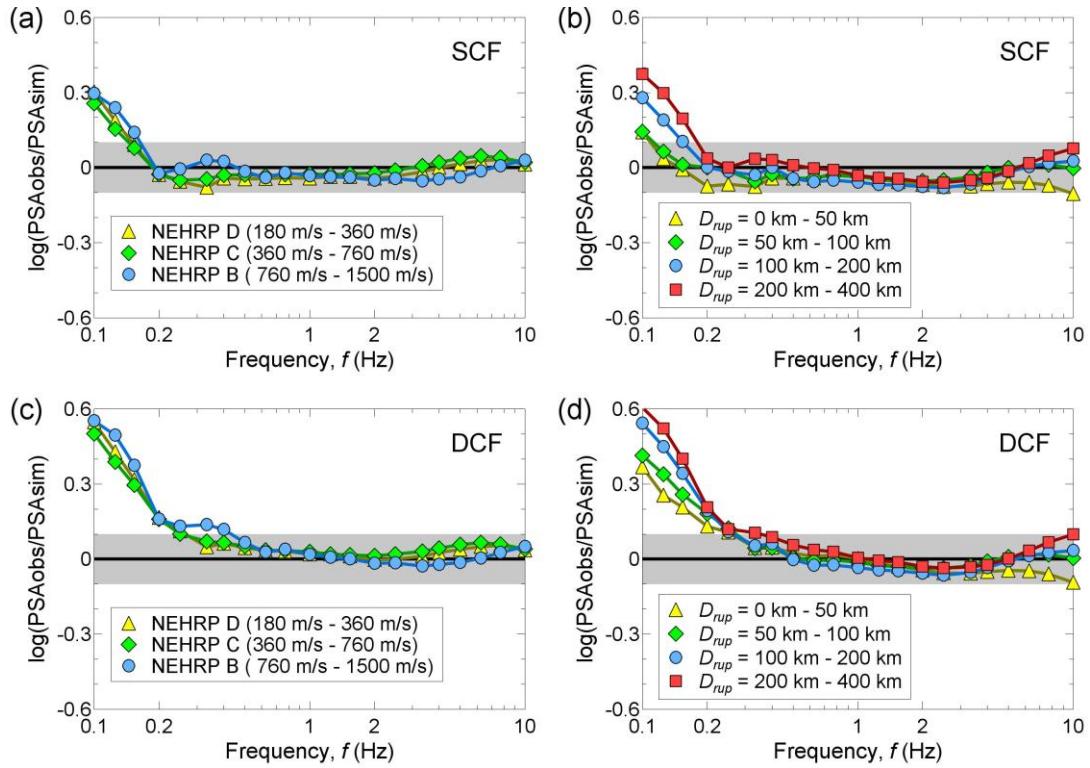
Figure 3.17 Residuals for simulated *PSA* based on the single- (top row) and double-corner frequency (bottom row) source models (C_{sim} applied), for b_1= -1.3. In graphs (a) and (c), symbols represent the station-weighted average of residuals at each frequency, for different site conditions. In graphs (b) and (d), symbols indicate residuals averaged over all magnitudes, for different distance ranges. The shaded areas illustrate ±0.1 log units about zero-residual line.

3.7 Comparison of ground-motion prediction from simulations and empirical GMPEs

We compare *PSA* predictions obtained from simulations and empirical GMPEs, as a function of magnitude in Figure 3.18, and as a function of distance in Figure 3.19. Simulations based on the SCF and DCF source models, for the proposed geometrical spreading model (b_1 = -1.3) are shown in the figures. For the empirical GMPEs, we evaluate the five NGA-West2 GMPEs (Abrahamson et al., 2014; Boore et al., 2014b; Campbell and Bozorgnia, 2014; Chiou and Youngs, 2014; Idriss, 2014) for California, assuming strike-slip events and NEHRP B/C site conditions. The simulations are in good

agreement with the GMPEs. This is true for both the SCF and DCF simulations. However the DCF simulations generally attain a closer match to the geometric mean of the GMPEs than do the SCF simulations. Overall, we conclude that the equivalent point-source DCF simulations with the proposed modeling parameters can predict average ground motions in California, generally within a ±25% error-band, for magnitudes up to **M**7.5, distances $D_{rup} < 400$ km and frequencies $f > 0.2$ Hz.

It is noteworthy that the pseudo-depth model given in Equation 3.5 yields over-saturation of response spectra at close distances to large events for high frequencies, as seen in Figure 3.18. The validity of the over-saturation is supported by the near-zero mean residuals attained at close distances for **M** > 5.5 events (Figure 3.14). However, if a user desires to prevent over-saturation of motions for forward prediction applications, the *h* model may be revised slightly as:

$$\log h = -0.405 + 0.235\mathbf{M} \tag{3.13}$$

This *h* model is derived by a trial and error procedure in such a way as to achieve an overall agreement with the empirically determined *h* values (see Figure 3.3) and to prevent the over-saturation of predicted amplitudes for large magnitudes. An example application of Equation 3.13 in GMPE development is given by Yenier and Atkinson (2015, Chapter 4).
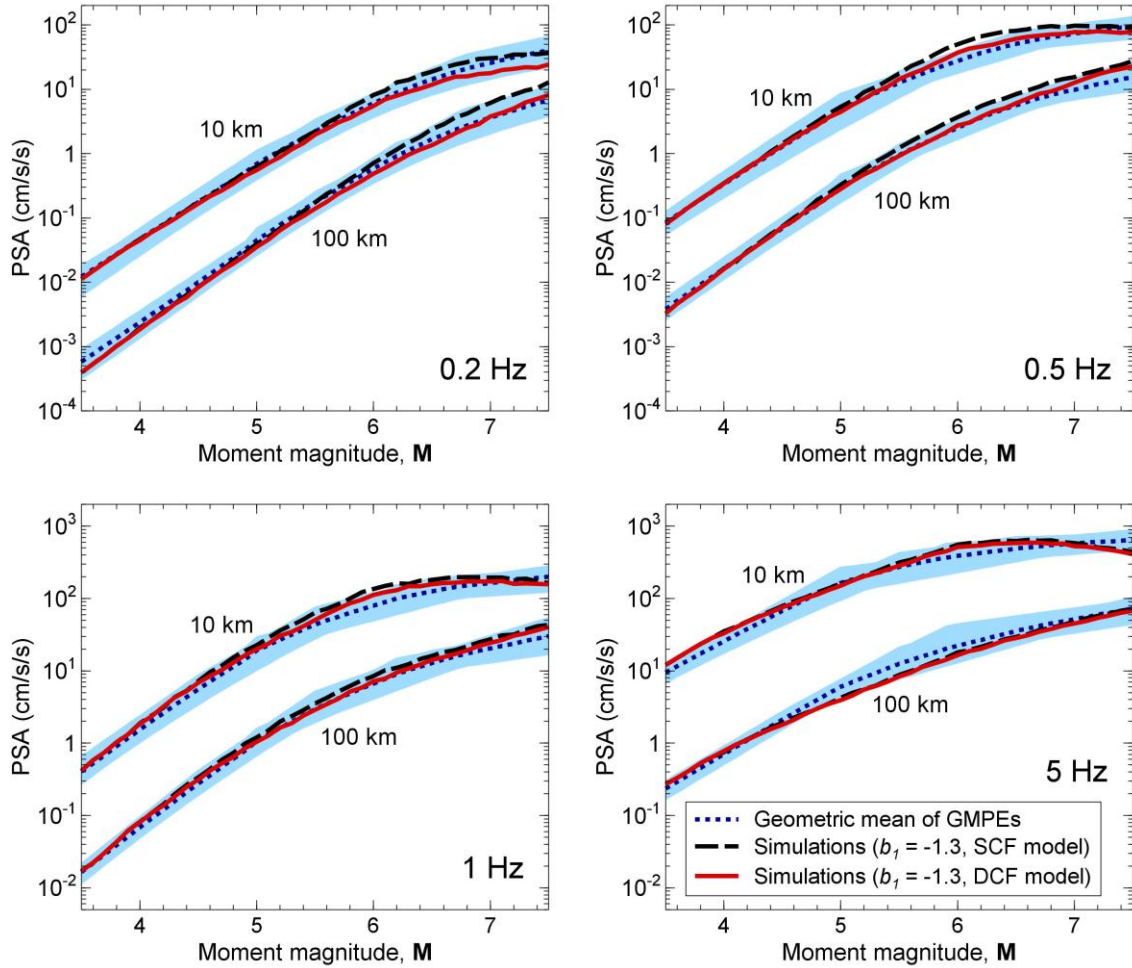
Figure 3.18 Simulated *PSA* obtained from the $b_1 = -1.3$ attenuation model ($C_{sim} = 3.16$), using the single- (SCF, dashed line) and double-corner-frequency (DCF, solid line) source models, as a function of magnitude. The dotted line represents the geometric mean of the predictions from the five NGA-West2 GMPEs and the shaded area indicates the region between $0.75PSA_{GMPE,min}(\mathbf{M}, D_{rup}, f)$ and $1.25PSA_{GMPE,max}(\mathbf{M}, D_{rup}, f)$, where $PSA_{GMPE,min}$ and $PSA_{GMPE,max}$ represent the minimum and maximum *PSA* obtained from the five GMPEs, for the given moment magnitude (**M**), rupture distance (D_{rup}) and frequency (*f*), respectively. Predictions from both simulations and GMPEs are determined for a fixed focal depth of $d = 7.5$ km.
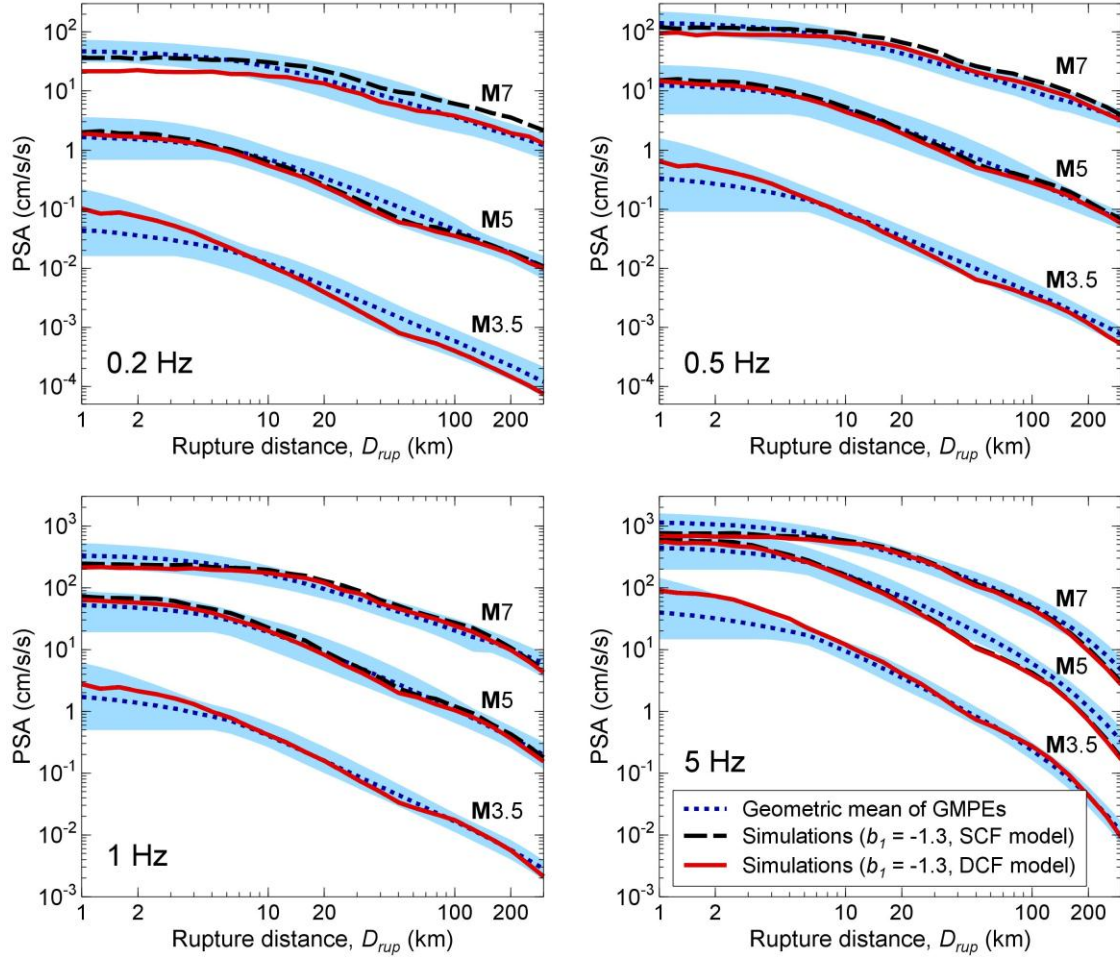
Figure 3.19 Simulated *PSA* obtained from the $b_1 = -1.3$ attenuation model ($C_{sim} = 3.16$), using the single- (SCF, dashed line) and double-corner-frequency (DCF, solid line) source models, as a function of distance. The dotted line represents the geometric mean of the predictions from the five NGA-West2 GMPEs. See the caption of Figure 18 for the definition of the shaded area. Predictions from both simulations and GMPEs are determined for a fixed focal depth of $d = 7.5$ km.

3.8   Possible sources of C_{sim}

We have shown that the simulation model, with our preferred $b_1 = -1.3$, successfully reproduces response spectral amplitudes. However, it is disconcerting that the model requires a large calibration factor ($C_{sim} = 3.16$). There are several possible factors that may contribute to the value of C_{sim}. One may be a discrepancy between the presumed

simple bilinear model (Equation 3.2) and the actual geometrical spreading, which may be more complex, with the complications mapping into C_{sim}. For example, if we introduced an additional hinge at close distances (~10 km or less) with a slower spreading rate, that could easily close the gap between the bilinear models with $b_1 = -1.0$ and $b_1 = -1.3$. More detailed treatment of effects due to radiation pattern and focal depths could also be helpful, as could frequency-dependent variability in the effective values of physical constants.

Another significant factor that may contribute to C_{sim} is that the descriptive parameters of the *FAS* model are generally derived from the S-wave window of the observed ground motions. However, the comparisons are done against observed response spectra which inherently include all phases, including both P-waves that impact short periods, and surface waves that impact long periods. The difference between these two could map into C_{sim}. In this regard, it is significant that a mismatch between *PSA* simulations and observations is commonplace in stochastic simulations, even when the underlying *FAS* model was based on the same set of observations. Finally, we acknowledge that although we prefer the $b_1 = -1.3$ spreading model due to its superiority in matching actual point-source decay of small-event amplitudes at longer periods, we cannot be entirely certain that the model is a better representation of the actual attenuation processes than the 1/R model on balance. It is possible that the 1/R model is more nearly correct, with the enhanced amplitudes that are observed at shorter distances being due to other factors such as directivity or radiation pattern.

3.9 A recipe for the development of a generic GMPE

We have shown that equivalent point-source simulations with the proposed source and attenuation models can be used to predict earthquake ground motions in California, for a wide range of magnitudes, distances and frequencies. One could use these simulations to develop a generic ground-motion prediction equation that can be adjusted for use in a different region, by modifying just the key source and attenuation modeling parameters. In such an approach, the calibrated simulations provide a robust basis for extending ground-motion predictions to magnitudes and distances where empirical data are sparse.

This is particularly important in regions such as eastern North America. Below, we propose a framework for developing this generic GMPE using the source and attenuation model derived for California.

Functional Form:

The generic GMPE should have a simple yet robust functional form that relates the key seismological parameters to the ground motion amplitude. The generic GMPE can be formulated based on Equation 3.1 as:

$$logPSA = F_E + F_Z + F_Q + F_S + C_{sim} \qquad (3.14)$$

where log*PSA* is the logarithm (base 10) of the pseudo-spectral acceleration (*PSA*); F_E, F_Z, F_Q and F_S represent effects for earthquake source, geometrical spreading, anelastic attenuation and site condition, respectively. The last term is the simulation calibration factor (C_{sim}) that accounts for the missing/different effects in simulations in comparison to ground motions observed in the target region.

The source effect (F_E) can be defined as the summation of magnitude (F_M) and stress parameter effects ($F_{\Delta\sigma}$):

$$F_E(\mathbf{M}, \Delta\sigma, f) = F_M\left(\mathbf{M}, f \,\middle|\, \frac{\Delta\sigma_{ref}}{\kappa_{0ref}}\right) + F_{\Delta\sigma}(\mathbf{M}, \Delta\sigma, f) \qquad (3.15)$$

The magnitude effect (F_M) models the influence of earthquake size on the spectral amplitudes obtained for the reference stress (e.g., $\Delta\sigma_{ref} = 100$ bar) and kappa (e.g., $\kappa_{0ref} = 0.025$ s) parameters, at the reference site conditions (NEHRP B/C). The stress parameter effect ($F_{\Delta\sigma}$) models the deviations from the reference model when $\Delta\sigma$ attains values different than the reference stress.

The total path effect (i.e., $F_Z + F_Q$) is modeled in an equivalent point-source sense based on Equation 3.4. The close-distance saturation effects can be modeled using the pseudo-depth model given in Equation 3.13, which prevents over-saturation of predicted amplitudes for large events (e.g., Yenier and Atkinson, 2015). The geometrical spreading effect (F_Z) is defined as:

$$F_Z = \log(Z) + F_{Z,RS-FS} \tag{3.16}$$

where $\log(Z)$ is the logarithm of Equation 3.6 and the second term ($F_{Z,RS-FS}$) represents the difference in spreading rates between the response and Fourier spectral amplitudes. The geometric spreading rates of Fourier amplitudes are $b_1 = -1.3$ and $b_2 = -0.5$ with a transition distance at $R_t = 50$ km, for the California reference model. This model has also been shown to apply in eastern North America (Atkinson and Boore, 2014). The anelastic attenuation effect (F_Q) is modeled as:

$$F_Q\big(C_Q, R, f\big) = C_Q(f)R \tag{3.17}$$

where C_Q is the frequency-dependent anelastic attenuation coefficient. This effect can be easily adjusted to model regions of either higher or lower Q than California.

The site effect (F_S) can be defined as the summation of linear site effects (F_{Lin}), nonlinear site effects (F_{Nonlin}) and kappa effects ($F_{\kappa0}$). The linear and nonlinear site effects can be either adopted from other empirical/theoretical studies (e.g., Boore and Joyner, 1997; Boore et al., 2014b) or derived from synthetic ground motions simulated for different site conditions (e.g., Akkar and Yenier, 2009). For the second alternative, the nonlinear site effects can be taken into account by performing site response analysis, using synthetic time series generated at the reference rock site as input motions. The kappa effect ($F_{\kappa0}$) could be used to adjust the generic GMPE relative to the reference kappa effect (κ_{0ref}) adopted in the base model, if sufficient evidence existed to modify this parameter.

Determination of Modeling Parameters

The parameters of the generic GMPE can be determined from regression of either SCF or DCF simulations for the proposed source and attenuation models. Here, we assume the DCF source and attenuation model determined for California, with the site effect (F_S) as defined relative to the NEHRP B/C site condition (i.e., $F_{Lin} = F_{Nonlin} = 1$ for $V_{S30} = 760$ m/s) by adopting the linear and nonlinear site effects model of Boore et al. (2014b). This forms a base-case model.

Regionally Adjustable Parameters

Here, we provide some guidelines for adjusting the generic GMPE by making the minimum required adjustments for its use in a different region. Changes should only be made to the extent they can be calibrated with the regional data. This could involve changes to the stress parameter and anelastic attenuation to reflect known differences relative to California, followed by checks for residual trends. It is recommended that changes to the geometrical spreading model only be made if there is compelling evidence in support of an alternative model. We note that calibration to a regional dataset over a reasonable magnitude-distance range is essential to ensure that the model is appropriately centered.

3.10 Conclusions

We develop a stochastic equivalent point-source simulation model that reproduces spectral amplitudes of earthquakes of up to **M**7.5 in California at distances of 1 km to 400 km, over frequencies from 0.2 Hz to 10 Hz. The main conclusions of this study are:

- Based on the agreement of the simulated and observed spectral shapes over a wide frequency range, we model the stress parameter as a function of magnitude and focal depth (Equation 3.9).

- Geometrical spreading in California can be modeled as $R^{-1.3}$ at distances less than 50 km and $R^{-0.5}$ at further distances. This model is statistically-preferred over the $1/R$ spreading model at distances < 50 km, for **M** < 5.5 events. For larger events, both geometrical spreading models are applicable because the apparent geometric attenuation is overpowered by the pseudo-depth term used to model near-distance saturation effects.

- An overall calibration factor of $C_{sim} = 3.16$ is required to match the observed spectral amplitudes, for all magnitudes, for our preferred $b_1 = -1.3$ model.

- A double-corner frequency (DCF) source model provides a better match to observations in comparison to the SCF simulations, particularly for moderate-to-large magnitude events (**M** > 5.5) at lower frequencies.

- There is a trade-off between the weighting parameter (ε) of the DCF source model and the path-duration model adopted in simulations. We propose an ε model (Equation 3.12) that is compatible with the path-duration model of Boore and Thompson (2014).

- Overall, we conclude that the equivalent point-source DCF simulations with the proposed modeling parameters can predict average ground motions in California, generally within a ±25% error-band, for magnitudes up to **M**7.5, distances $D_{rup} <$ 400 km and frequencies $f > 0.2$ Hz.

- In light of these observations, we propose a framework for developing a simulation-based generic GMPE that can be adjusted for source and attenuation attributes in different regions by modifying its key source and attenuation modeling parameters.

3.11 Data and resources

We compiled the response spectra of ground motions for California earthquakes from the NGA-West2 flatfile that is publicly available at http://peer.berkeley.edu/ngawest2/databases/ (last accessed in July 2014). Ground-motion simulations were performed using the SMSIM v3.8 software that is available at http://www.daveboore.com/software_online.html (last accessed in July 2014). The predictions of NGA-West2 GMPEs were determined by using the NGAW2_GMPE_Spreadsheets_v5.5_060514.xls Excel file created by Dr. Emel Seyhan (http://peer.berkeley.edu/ngawest2/databases/, last accessed in July 2014). All graphics were produced using CoPlot software (www.cohort.com, last accessed July 2014).

3.12 Acknowledgements

3.13 References

Abrahamson, N. A., W. J. Silva, and R. Kamai (2014). Summary of the ASK14 ground motion relation for active crustal regions, *Earthquake Spectra* **30**, 1025–1055.

Anderson, J. G. (2000). Expected shape of regressions for ground-motion parameters on rock, *Bull. Seismol. Soc. Am.* **90**, S43–S52.

Akkar, S., and E. Yenier, (2009). Assessment of point-source stochastic simulations using recently derived ground-motion prediction equations, *Bull. Seismol. Soc. Am.* **99**, 3172–3191.

Anderson, J. G., and S. E. Hough (1984). A model for the shape of the Fourier amplitude spectrum of acceleration at high frequencies, *Bull. Seismol. Soc. Am.* **74**, 1969–1993.

Atkinson, G. M. (1993). Earthquake source spectra in eastern North America, *Bull. Seismol. Soc. Am.* **83**, 1778–1798.

Atkinson, G. M. (2004). Empirical attenuation of ground-motion spectral amplitudes in southeastern Canada and the northeastern United States, *Bull. Seismol. Soc. Am.* **94**, 1079–1095.

Atkinson, G. M. (2012). Evaluation of attenuation models for the northeastern United States/southeastern Canada, *Seismol. Res. Lett.* **83**, 166–178.

Atkinson, G. M., and D. M. Boore (1995). Ground-motion relations for eastern North America, *Bull. Seismol. Soc. Am.* **85**, 17–30.

Atkinson, G. M., and D. M. Boore (2006). Earthquake ground-motion prediction equations for eastern North America, *Bull. Seismol. Soc. Am.* **96**, 2181–2205.

Atkinson, G. M., and D. M. Boore (2014). The attenuation of Fourier amplitudes for rock sites in eastern North America, *Bull. Seismol. Soc. Am.* **104**, 513–528.

Atkinson, G. M., and W. Silva (1997). An empirical study of earthquake source spectra for California earthquakes, *Bull. Seismol. Soc. Am.* **87**, 97–113.

Atkinson, G. M., and W. Silva (2000). Stochastic modeling of California ground motions, *Bull. Seismol. Soc. Am.* **90**, 255–274.

Atkinson, G. M., W. Greig, and E. Yenier (2014). Estimation of moment magnitude (**M**) for small events (**M**<4) on local networks, *Seismol. Res. Lett.* **85**, 1116–1124.

Babaie Mahani, A., and G. M. Atkinson (2012). Evaluation of functional forms for the attenuation of small-to-moderate-earthquake response spectral amplitudes in North America, *Bull. Seismol. Soc. Am.* **102**, 2714–2726.

Boore, D. M. (1983). Stochastic simulation of high-frequency ground motions based on seismological models of the radiated spectra, *Bull. Seismol. Soc. Am.* **73**, 1865–1894.

Boore, D. M. (1984). Use of seismoscope records to determine M_L and peak velocities, *Bull. Seism. Soc. Am.* **74**, 315-324.

Boore, D. M. (2003). Simulation of ground motion using the stochastic method, *Pure and Applied Geophysics*, **160**, 635-376.

Boore, D. M. (2005). SMSIM---Fortran programs for simulating ground motions from earthquakes: Version 2.3---A revision of OFR 96-80-A, U.S. Geological Survey Open-File Report, *U. S. Geological Survey Open-File Report* **00-509**, revised 15 August 2005, 55 pp.

Boore, D. M. (2009). Comparing stochastic point-source and finite-source ground motion simulations: SMSIM and EXSIM, *Bull. Seismol. Soc. Am.* **99**, 3202–3216.

Boore, D.M. (2010). Orientation-independent, non geometric-mean measures of seismic intensity from two horizontal components of motion, *Bull. Seismol. Soc. Am.* **100**, 1830–1835.

Boore, D. M., and W. B. Joyner (1997). Site amplifications for generic rock sites, *Bull. Seismol. Soc. Am.* **87**, 327–341.

Boore, D. M., and E. M. Thompson (2014). Path durations for use in the stochastic-method simulation of ground motions, *Bull. Seismol. Soc. Am.* **104**, 2541–2552.

Boore, D. M., and E. M. Thompson (2015). Revisions to some parameters used in stochastic-method simulations of ground motion, *Bull. Seismol. Soc. Am.* **105**, (in press).

Boore, D. M., K. W. Campbell, and G. M. Atkinson (2010). Determination of stress parameters for eight well-recorded earthquakes in eastern North America, *Bull. Seism. Soc. Am.* **100**, 1632–1645.

Boore, D. M., C. Di Alessandro, and N. A. Abrahamson (2014a). A generalization of the double-corner-frequency source spectral model and its use in the SCEC BBP Validation Exercise, *Bull. Seismol. Soc. Am.* **104**, 2387–2398.

Boore, D. M., J. P. Stewart, E. Seyhan, and G. M. Atkinson (2014b). NGA-West2 equations for predicting PGA, PGV, and 5% damped PSA for shallow crustal earthquakes, *Earthquake Spectra* **30**, 1057–1085.

Brune, J. N. (1970). Tectonic stress and the spectra of seismic shear waves from earthquakes, *J. Geophys. Res.* **75**, 4997–5009.

Burger, R. W., P. G. Somerville, J. S. Barker, R. B. Herrmann, and D. V. Helmberger (1987). The effect of crustal structure on strong ground motion attenuation relations in eastern North America, *Bull. Seismol. Soc. Am.* **77**, 420–439.

Campbell, K. W. (2003). Prediction of strong ground motion using the hybrid empirical method and its use in the development of ground-motion (attenuation) relations in eastern North America, *Bull. Seismol. Soc. Am.* **93**, 1012–1033.

Campbell, K. W. and Y. Bozorgnia (2014). NGA-West2 ground motion model for the average horizontal components of PGA, PGV, and 5% damped linear acceleration response spectra, *Earthquake Spectra* **30**, 1087–1115.

Chapman, M. C., and R. W. Godbee (2012). Modeling geometrical spreading and the relative amplitudes of vertical and horizontal high-frequency ground motions in eastern North America, *Bull. Seismol. Soc. Am.* **102**, 1957–1975.

Chapman, M. C. (2013). On the rupture process of the 23 August 2011 Virginia earthquake, *Bull. Seismol. Soc. Am.* **103**, 613–628.

Chiou, B-S. J. and R. R. Youngs (2014). Update of the Chiou and Youngs NGA model for the average horizontal component of peak ground motion and response spectra, *Earthquake Spectra* **30**, 1117–1153.

Frankel, A., C. Mueller, T. Barnhard, D. Perkins, E. Leyendecker, N. Dickman, S. Hanson, and M. Hopper (1996). National seismic hazard maps: documentation June 1996, *U.S. Geol. Surv. Open-File Rept. 96-532*, 69 pp.

Goulet, C. A., N. A. Abrahamson, P. G. Somerville, and K. E. Wooddell (2015). The SCEC Broadband Platform validation exercise: methodology for code validation in the context of seismic hazard analyses, *Seismol. Res. Letters* **86**, 17–26.

Hanks, T. C., and H. Kanamori (1979). A moment magnitude scale, *J. Geophys. Res.* **84**, 2348–2350.

Hanks, T. C., and R. K. McGuire (1981). The character of high-frequency strong ground motion, *Bull. Seismol. Soc. Am.* **71**, 2071–2095.

Idriss, I. M. (2014). An NGA-West2 empirical model for estimating the horizontal spectral values generated by shallow crustal earthquakes, *Earthquake Spectra* **30**, 1155–1177.

Mereu, R. F, S. Dineva, and G. M. Atkinson (2013). The application of velocity spectral stacking to extract information on source and path effects for small-to-moderate earthquakes in southern Ontario with evidence for constant-width faulting, *Seism. Res. Lett.* 84, 899–916.

Motazedian, D., and G. M. Atkinson (2005). Stochastic finite-fault modeling based on a dynamic corner frequency, *Bull. Seismol. Soc. Am.* **95**, 995–1010.

Ojo, S., and R. Mereu (1986). The effect of random velocity functions on the travel times and amplitudes of seismic waves, *Geophysical Journal of the Royal Astronomical Society* **84**, 607–618.

Ou, G.-B., and R. B. Herrmann (1990). A statistical model for ground motion produced by earthquakes at local and regional distances, *Bull. Seismol. Soc. Am.* **80**, 1397–1417.

Pezeshk, S., A. Zandieh, and B. Tavakoli (2011). Hybrid empirical ground-motion prediction equations for eastern North America using NGA models and updated seismological parameters, *Bull. Seismol. Soc. Am.* **101**, 1859–1870.

Raoof, M., R. B. Herrmann, and L. Malagnini, (1999). Attenuation and excitation of three-component ground motion in southern California, *Bull. Seismol. Soc. Am.* **89**, 888–902.

Rogers, A. M., and D. M. Perkins (1996). Monte Carlo simulation of peak acceleration attenuation using a finite-fault uniform-patch model including isochron and extremal characteristics, *Bull. Seismol. Soc. Am.* **86**, 79–92.

Silva,W. J., N. Abrahamson, G. Toro, and C. Costantino (1996). Description and validation of the stochastic ground motion model, Report to Brookhaven National Laboratory, Associated Universities, Inc., Upton, New York.

Somerville, P., J. McLaren, C. Saikia, and D. Helmberger (1990). The 25 November 1988 Saguenay, Quebec earthquake: Source parameters and the attenuation of strong ground motion, *Bull. Seismol. Soc. Am.* **80**, 1118–1143.

Toro, G., N. Abrahamson, and J. Schneider (1997). Model of strong ground motion in eastern and central North America: best estimates and uncertainties, *Seism. Res. Lett.* **68**, 41–57.

Yenier, E., and G. M. Atkinson (2014). Equivalent point-source modeling of moderate-to-large magnitude earthquakes and associated ground-motion saturation effects, *Bull. Seismol. Soc. Am.* **104**, 1458–1478.

Yenier, E., and G. M. Atkinson (2015). Regionally-adjustable generic ground-motion prediction equation based on equivalent point-source simulations: Application to central and eastern North America, *Bull. Seismol. Soc. Am.* (in review).

Yenier, E., and G. M. Atkinson (manuscript in preparation). Modeling source and attenuation attributes of the 2010-2012 Christchurch, New Zealand earthquakes based on equivalent point-source modeling technique.

Chapter 4

4 Regionally-adjustable generic GMPE based on equivalent point-source simulations: Application to central and eastern North America[3]

4.1 Introduction

Reliable estimates of ground motions that may be produced by future earthquakes require robust modeling of the earthquake source and attenuation attributes in the region of interest. Ground-motion observations from past events provide a valuable empirical basis to develop ground-motion prediction equations (GMPEs) that describe amplitudes as a function of variables such as magnitude, distance and site condition. However, with the exception of well-monitored active regions such as California and Japan, empirical ground-motion data are generally sparse in the magnitude-distance range of engineering interest. Thus, there are insufficient data for development of reliable GMPEs in many regions, with central and eastern North America (CENA) being a classic example.

There are several alternative methods used for derivation of GMPEs in data-poor regions. A widely-used method is the simulation-based approach, in which synthetic ground motions are generated over a wide magnitude and distance range, and the GMPE is developed based on the simulated amplitude data. The simulations are based on a seismological model of the source, path and site effects, with the parameters being calibrated using the available empirical data for the region. Simulations can be performed using a variety of techniques ranging from simple stochastic point-source methods to more sophisticated finite-source broadband simulations (e.g., Atkinson and Boore, 1995, 2006; Toro et al., 1997; Silva et al., 2002; Somerville et al., 2001, 2009; Frankel, 2009).

[3] A version of this chapter has been submitted for publication. Yenier, E., and G. M. Atkinson (2015). Regionally-adjustable generic ground-motion prediction equation based on equivalent point-source simulations: Application to central and eastern North America, *Bull. Seismol. Soc. Am.*

Another common approach is the hybrid empirical method (Campbell, 2002, 2003). This method calibrates an empirically well-constrained GMPE in a data-rich host region (e.g., western North America, WNA) for use in a data-poor target region (e.g., CENA) based on adjustment factors obtained from response-spectral ratios of stochastic simulations in the host and target regions (e.g., Campbell, 2002, 2003; Scherbaum et al., 2005; Pezeshk et al., 2011). A third method is the referenced empirical approach introduced by Atkinson, (2008). It is similar to the hybrid empirical method in concept but adjustment factors are determined empirically using spectral ratios of observed motions in the target region to predictions of an empirical GMPE in the host region (e.g., Atkinson, 2008, 2010; Atkinson and Boore, 2011, Atkinson and Motazedian, 2013; Hassani and Atkinson, 2014).

Both the hybrid empirical method and the referenced empirical approach anchor their predictions to magnitude scaling and saturation effects observed in data-rich regions, assuming that these effects are transferable. Although the magnitude scaling is assumed to be similar between regions, no such assumption is made regarding the overall level of ground-motion amplitudes. Differences in overall amplitude level and distance scaling between regions are attributed to regional differences in fundamental source and attenuation parameters. The hybrid empirical method requires sound knowledge of these parameters in both host and target regions in order to determine host-to-target adjustment factors via simulations reliably. This may restrict the applicability of the method (Campbell, 2003). The referenced empirical approach resolves this issue by determining the adjustment factors empirically, avoiding the need for assumptions of the source and attenuation parameters for the host and target regions. An important limitation of the referenced empirical approach, however, is that the available ground-motion data in the target region may not sufficiently represent all important regional characteristics (Atkinson, 2008).

In this study, we take advantage of key concepts from both the hybrid empirical and referenced empirical approaches to develop a robust simulation-based generic GMPE. The generic GMPE can be adjusted for use in any region by modifying a few key modeling parameters, and calibrated for regional use from limited empirical data. The

basic idea is that we first develop a well-calibrated simulation-based GMPE for active tectonic regions, using the NGA-West2 database (Ancheta et al., 2014). We parameterize this generic GMPE so as to isolate the effects of the basic source and attenuation parameters on peak ground motions and response spectra. This provides effective and transparent control over the transferable factors between regions. The fundamental seismological parameters that are used as predictive variables in the generic GMPE include magnitude, distance, stress parameter, geometrical spreading rate and the anelastic attenuation coefficient. This provides an adjustable predictive model that is readily calibrated with minimal regional data. In the generic GMPE, we also consider an empirical calibration factor to account for residual effects that are different and/or missing in simulations compared to empirical data. This closes any remaining gap between simulated and observed motions.

We provide a recipe for the adjustment of the generic GMPE to a specific region. As an example implementation of the generic model, we use it to develop a GMPE for CENA by adjusting the stress and anelastic attenuation, and calibrate the model using the NGA-East database. During the calibration exercise, we infer a magnitude- and depth-dependent stress parameter model based on the values obtained from study events. We provide median predictions of ground motions in CENA for average horizontal-component peak ground motions and 5%-damped pseudo spectral acceleration (periods up to T = 10 s), for wide ranges of magnitude (**M**3-**M**8) and distance (< 600 km).

4.2   Functional form of the generic GMPE

A regionally-adjustable generic prediction equation requires a robust yet simple functional form that successfully decouples the effects of fundamental source and attenuation parameters on ground-motion amplitudes. We define the generic GMPE as

$$\ln Y = F_E + F_Z + F_\gamma + F_S + C \tag{4.1}$$

where $\ln Y$ is the natural logarithm of a ground-motion intensity measure. F_E, F_Z, F_γ and F_S represent functions for earthquake source, geometrical spreading, anelastic attenuation and site effects, respectively. The C term is an empirical calibration factor that accounts

for the residual differences between simulations and empirical data. We formulate the source and geometrical spreading effects (F_E and F_Z) in an equivalent point-source sense, using ground-motion simulations with parameters calibrated to observations in California, obtained from the NGA-West2 database (Ancheta et al., 2014). The anelastic attenuation (F_γ) is adjusted to optimize observed frequency-dependent attenuation effects. In this study, we provide predictions for the orientation-independent horizontal component of peak ground acceleration (PGA), peak ground velocity (PGV) and 5%-damped pseudo-spectral acceleration (PSA), where PGA and PSA are given in units of g and PGV is in cm/s.

The source function (F_E) describes the effects of magnitude and stress parameter on ground-motion amplitudes as:

$$F_E = F_M + F_{\Delta\sigma} \tag{4.2}$$

where F_M represents the magnitude effect on ground-motion amplitudes that would be observed at the source, if there were no distance-saturation effects. It is defined for the reference stress ($\Delta\sigma$), κ_0 parameter, and site condition. We choose $\Delta\sigma = 100$ bar and $\kappa_0 = 0.025$ s as the reference modeling parameters based on the findings of Yenier and Atkinson (2015, Chapter 3) for California earthquakes. In Equation 4.2, $F_{\Delta\sigma}$ represents the stress adjustment factor that is needed when $\Delta\sigma$ is different than 100 bars.

The F_M term is defined as a function of moment magnitude (**M**), using a hinged-quadratic function:

$$F_M = \begin{cases} e_0 + e_1(\mathbf{M} - \mathbf{M}_h) + e_2(\mathbf{M} - \mathbf{M}_h)^2 & \mathbf{M} \leq \mathbf{M}_h \\ e_0 + e_3(\mathbf{M} - \mathbf{M}_h) & \mathbf{M} > \mathbf{M}_h \end{cases} \tag{4.3}$$

where the hinge magnitude, $\mathbf{M}_h$, and model coefficients, e_0 to e_3, are period-dependent. This mimics the functional form of magnitude scaling used by Boore et al. (2014b) in their NGA-West2 empirical GMPE.

The stress adjustment term is defined as:

$$F_{\Delta\sigma} = e_{\Delta\sigma}\ln(\Delta\sigma/100) \tag{4.4}$$

where $e_{\Delta\sigma}$ describes the rate of the ground-motion scaling with $\Delta\sigma$. Equation 4.4 describes the relationship between stress parameter and response spectral amplitudes, facilitating the determination of $\Delta\sigma$ from PSA data in the target region.

We model the geometrical spreading effects based on the equivalent point-source method. Seismic waves are assumed to radiate from a virtual point source placed at an overall effective distance from the site, such that the empirically-observed saturation effects are successfully reproduced. The effective distance (R) is given as

$$R = \sqrt{{D_{rup}}^2 + h^2} \qquad (4.5)$$

where D_{rup} is the closest distance from the site to the fault-rupture surface and h is a pseudo-depth term that accounts for distance saturation effects. The pseudo-depth is generally defined as a function of magnitude to account for the extension of distance-saturation effects to larger distances with increasing magnitude. In this study, we define the pseudo-depth as

$$h = 10^{-0.405 + 0.235\mathbf{M}} \qquad (4.6)$$

Equation 4.6 is derived by a trial and error procedure in such a way as to achieve an overall agreement with the empirically determined h values and to prevent the over-saturation of predicted amplitudes for large magnitudes (Yenier and Atkinson, 2015).

We define the geometrical spreading function (F_Z) as

$$F_Z = \ln(Z) + (b_3 + b_4\mathbf{M}) \ln\left(R/R_{ref}\right) \qquad (4.7)$$

where Z represents the geometrical attenuation of Fourier amplitudes, while the multiplicative component, $(b_3+b_4\mathbf{M})\ln(R/R_{ref})$, accounts for the change in the apparent attenuation that occurs when ground motions are modeled in the response spectral domain rather than the Fourier domain. The coefficients b_3 and b_4 are period-dependent, and R_{ref} is the reference effective distance, given as $R_{ref} = \sqrt{1 + h^2}$.

In ground-motion modeling, Z is generally considered as a piecewise continuous function that describes the distance-dependent attributes of geometrical spreading, considering the contributions of direct waves at close distances, and multiple reflections and refractions at larger distances. Babaie Mahani and Atkinson (2012) evaluated the ability of various functional forms to describe the geometrical attenuation in North America, and concluded that a bilinear model provides a good balance between simplicity and ability to capture the key attenuation attributes over a broad distance range. In this study, we define Z using a hinged bilinear model that provides for a transition from direct-wave spreading to surface-wave spreading of reflected and refracted waves:

$$Z = \begin{cases} R^{b_1} & R \leq R_t \\ R_t^{b_1}(R/R_t)^{b_2} & R > R_t \end{cases} \qquad (4.8)$$

where R_t represents the transition distance, and b_1 and b_2 are the geometrical attenuation rates of Fourier amplitudes at $R \leq R_t$ and $R > R_t$, respectively. In the generic GMPE, we fix the transition distance at $R_t = 50$ km based on the findings of Yenier and Atkinson (2014, Chapter 2).

The geometrical spreading rate at close distances is often assumed to be given by $b_1 = -1.0$, based on the homogeneous whole-space approximation. However, theoretical waveform simulations suggest faster spreading rates, about $b_1 \approx -1.3$, for typical layered earth models (Ojo and Mereu 1986; Burger et al., 1987; Ou and Herrmann, 1990; Somerville et al., 1990; Chapman and Godbee, 2012, Chapman 2013). Empirical modeling of ground motions in various regions, including WNA, CENA and Australia also support this finding (Atkinson, 2004; Allen, 2007; Babaie Mahani and Atkinson, 2012; Yenier and Atkinson, 2014, 2015). Therefore, we define the geometrical spreading rate at $R \leq 50$ km as $b_1 = -1.3$ in the generic model. The geometrical spreading rate at $R > 50$ km is fixed at the widely-used value of $b_2 = -0.5$, which is consistent with attenuation of surface waves in a half-space (Ou and Herrmann 1990; Atkinson 2012).

Equation 4.7 effectively decouples the geometrical spreading of Fourier amplitudes (Z) and the change in observed decay of amplitudes when convolved by the response transfer function. Although the descriptive parameters of Z are fixed at their generic values in the

model, Equation 4.7 allows modification of the shape and rates of Z if there is compelling evidence supporting such a change. In such a case, the preferred model as given in Equation 4.8 can be replaced with an alternative geometrical spreading model that is compatible with the decay of the Fourier amplitudes in the target region.

The anelastic attenuation function (F_γ) is given as:

$$F_\gamma = \gamma D_{rup} \tag{4.9}$$

where γ is a period-dependent anelastic attenuation coefficient that is empirically determined from regional ground-motion data.

In the generic GMPE, we describe site effects relative to a reference condition of NEHRP (National Earthquake Hazards Reduction Program) B/C boundary, for which the travel-time weighted average shear-wave velocity over the top 30 m is $V_{S30} = 760$ m/s. In this study, we adopt the site effects model of BSSA14 (Boore et al., 2014b):

$$F_S = F_{lin} + F_{nl} \tag{4.10}$$

where F_{lin} represents the linear site effects, and F_{nl} represents the nonlinear site effects. The linear site response is defined as a function of V_{S30}:

$$F_{lin} = \begin{cases} c \ln(V_{S30}/760) & V_{S30} \leq V_c \\ c \ln(V_c/760) & V_{S30} > V_c \end{cases} \tag{4.11}$$

where c describes the V_{S30}-scaling and V_c is the limiting velocity beyond which ground motions no longer scale with V_{S30}. The nonlinear site response is given as

$$F_{nl} = f_1 + f_2 \ln \left[\frac{PGA_r + f_3}{f_3} \right] \tag{4.12}$$

where f_2 represents the degree of nonlinearity as a function of V_{S30}:

$$f_2 = f_4 [\exp\{f_5(\min(V_{S30}, 760) - 360)\} - \exp\{f_5(760 - 360)\}] \tag{4.13}$$

In Equations 4.11 to 4.13, parameters c, V_c, f_1, f_3, f_4 and f_5 are model coefficients given in BSSA14 (Boore et al., 2014b) and PGA_r is the median peak horizontal acceleration predicted for the reference condition ($V_{S30} = 760$ m/s).

4.3   Determination of model coefficients

We calculate model coefficients of the magnitude effect (F_M), geometrical spreading function (F_Z) and stress adjustment factor ($F_{\Delta\sigma}$) from amplitude data generated from ground-motion simulations. The simulations are based on the equivalent point-source stochastic method with modeling parameters calibrated to observed motions in California as described by Yenier and Atkinson (2015); model parameters are summarized in Table 4.1. Briefly, we use the additive double-corner-frequency source model of Boore et al. (2014a) with a spectral-sag parameter (ε) suggested by Yenier and Atkinson (2015). In simulations, the geometrical decay of Fourier amplitudes (Z) is defined in terms of effective distance, as given in Equation 4.8 ($b_1 = -1.3$, $b_2 = -0.5$ and $R_t = 50$ km). We use the pseudo-depth model given in Equation 4.6 to account for near-distance saturation effects. We constrained the pseudo-depth function to avoid oversaturation of predicted amplitudes at large magnitudes (shown later). The simulations do not include anelastic attenuation, because we will determine these effects empirically from regional ground-motion data (shown later). We simulate ground motions at NEHRP B/C site conditions assuming the generic crustal amplification factors given by Atkinson and Boore (2006). We assume that the near-surface high-frequency attenuation parameter is $\kappa_0 = 0.025$ s for this site class. Yenier and Atkinson (2015) showed that equivalent point-source simulations with these modeling parameters (but also including regional anelastic attenuation effects) can reproduce average observed spectral amplitudes of earthquakes in California, within ±25% error band, for magnitudes up to **M**7.5 and distances less than 400 km. Any inadequacies or misfits between the simulations and empirical data will map into unresolved residuals, which will be taken into account through the calibration factor, C.

Table 4.1 Parameter values used in stochastic equivalent point-source simulations (from

Yenier and Atkinson, 2015)

Parameter	Value
Shear-wave velocity	$\beta = 3.7$ km/s
Density	$\rho = 2.8$ g/cm^3
Source model	Generalized additive double-corner-frequency source model of Boore et al. (2014a)
Spectral sag	$\varepsilon = min[1, 10^{1.2 - 0.3\mathbf{M}}]$
Effective distance	$R = (D_{rup}^2 + h^2)^{0.5}$
Pseudo-depth	$h = 10^{-0.405 + 0.235\mathbf{M}}$
Geometrical attenuation	$R^{-1.3}$ for $R \leq 50$ km, and $50^{-1.3}(R/50)^{-0.5}$ for $R > 50$ km
Anelastic attenuation	Not considered in simulations (determined empirically)
Site amplification (NEHRP B/C)	Table 4 of Atkinson and Boore (2006) Frequency-amplification pairs delimited by semicolons: 0.0001Hz-1; 0.1Hz-1.07; 0.24Hz-1.15; 0.45Hz-1.24; 0.79Hz-1.39; 1.38Hz-1.67; 1.93Hz-1.88; 2.85Hz-2.08; 4.03Hz-2.2; 6.34Hz-2.31; 12.5Hz-2.41; 21.2Hz-2.45; 33.4Hz-2.47; 82Hz-2.50
Kappa factor	$\kappa_0 = 0.025$ s
Source duration	$0.5/f_a + 0.5/f_b$ where f_a and f_b are the corner frequencies
Path duration[*]	Table 1 of Boore and Thompson (2014) Rupture distance-path duration pairs delimited by semicolons: 0km-0s; 7km-2.4s; 45km-8.4s; 125km-10.9s; 175km-17.4s; 270km-34.2s. Path duration increases with distance at a rate of 0.156s/km after the last nodal point.
Simulation calibration factor for California[†]	$C_{sim} = 3.16$

[*] In simulations, the nodal rupture distances are converted to effective distance based on Equation 4.6 at each magnitude level.
[†] Factor applied to simulations for matching simulations to observed response spectra in California with zero bias. (Reader is referred to Yenier and Atkinson (2015) for more information regarding the C_{sim} parameter)

We perform time-domain equivalent point-source stochastic simulations using the widely-cited SMSIM software (Boore, 2003, 2005), for magnitudes from $\mathbf{M}$3 to $\mathbf{M}$8 (with increments of 0.1 $\mathbf{M}$ units) and distances from 1 km to 400 km (with increments of 0.1 log$_{10}$ units), for a fixed stress parameter of $\Delta\sigma = 100$ bar. We generate 100 synthetic

ground motions for each combination of $\mathbf{M}$, and D_{rup}. For each simulated time series we calculate PGA, PGV and PSA at 31 periods from 0.01 s to 10 s, then take the geometric mean for each parameter over the 100 simulations.

The coefficients of the magnitude-scaling term F_M are computed from the regression of simulations obtained at $D_{rup} = 1$ km ($Y_{\mathrm{sim,1km}}$). Recall that F_M represents the magnitude scaling of ground motions that would be observed at the source if there were no saturation effects. Therefore, we need to remove the saturation effects that we imposed in the simulations at 1 km to extract the unsaturated magnitude effects, F_M. This is easily done:

$$\ln Y_{\mathrm{sim,1km}} = F_M - 1.3\ln\left(\sqrt{1 + h^2}\right) \tag{4.14}$$

where the last term accounts for the saturation effects imposed in the simulations (i.e. F_Z at $D_{rup} = 1$ km). We use a grid search to determine the hinge magnitude ($\mathbf{M_h}$), where we determine the coefficients e_0 to e_3 by regression of the amplitudes at 1 km, for each trial value of $\mathbf{M_h}$. We select the best-fitting $\mathbf{M_h}$ and the associated coefficients (e_0 to e_3) based on minimizing the residuals of the simulated amplitudes with respect to the model equation. Figure 4.1 compares ground motions simulated at $D_{rup} = 1$ km and the fitted model (Equation 4.14) as a function of magnitude, for peak ground motions and response spectra. As seen in the figure, the fitted functional form captures the magnitude scaling and saturation effects implied by simulations very well.

We determined the model coefficients of the geometrical spreading function from regression of simulated amplitudes at variable distances, after removing the magnitude effects (i.e. $\ln Y_{\mathrm{sim}} - F_M$). We use the form:

$$\ln Y_{\mathrm{sim}} - F_M = \ln(Z) + (b_3 + b_4\mathbf{M})\ln\left(R/R_{ref}\right) \tag{4.15}$$

In this regression, we constrain the Z to the decay shape used in the simulations (i.e., $b_1 = -1.3$, $b_2 = -0.5$ and $R_t = 50$ km). This forces the differences between the decay rates of Fourier and response spectral amplitudes to map into $(b_3+b_4\mathbf{M})\ln(R/R_{ref})$. In Figure 4.2, we compare the generic GMPE (i.e., $F_M + F_Z$) against simulations to assess the

performance of the fitted F_Z model. This shows that the generic GMPE is in good agreement with the behavior of the simulated amplitudes. The values of model coefficients for F_M and F_Z are listed in Table A.1. This specifies the generic GMPE for California for the reference stress parameter (100 bars) and the reference site condition (B/C), but without anelastic attenuation or overall amplitude calibration factor. These factors can be determined empirically, as described further later.
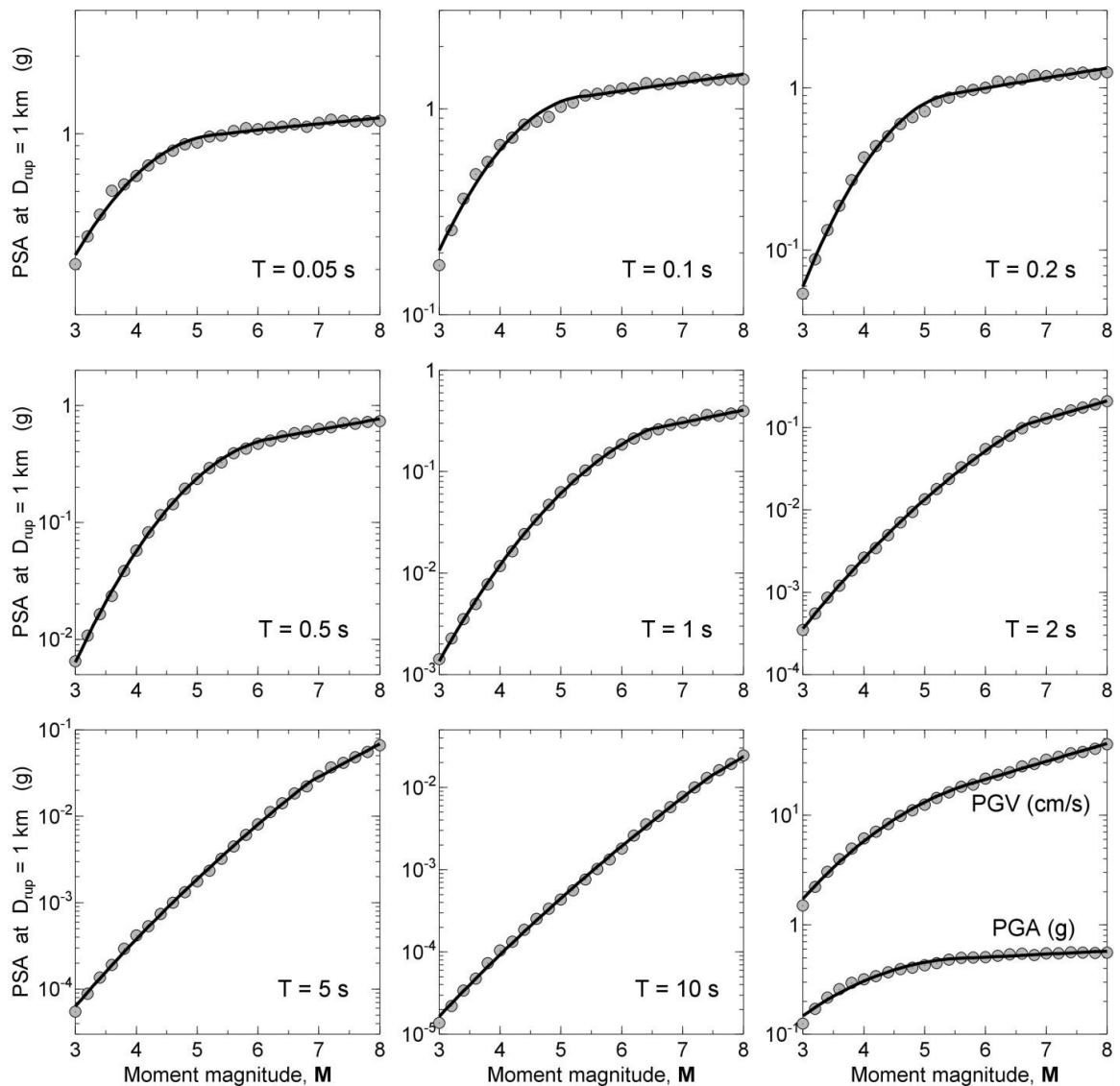
Figure 4.1 Ground motions simulated at $D_{rup} = 1$ km (circles), and the fitted model (lines) as a function of magnitude.
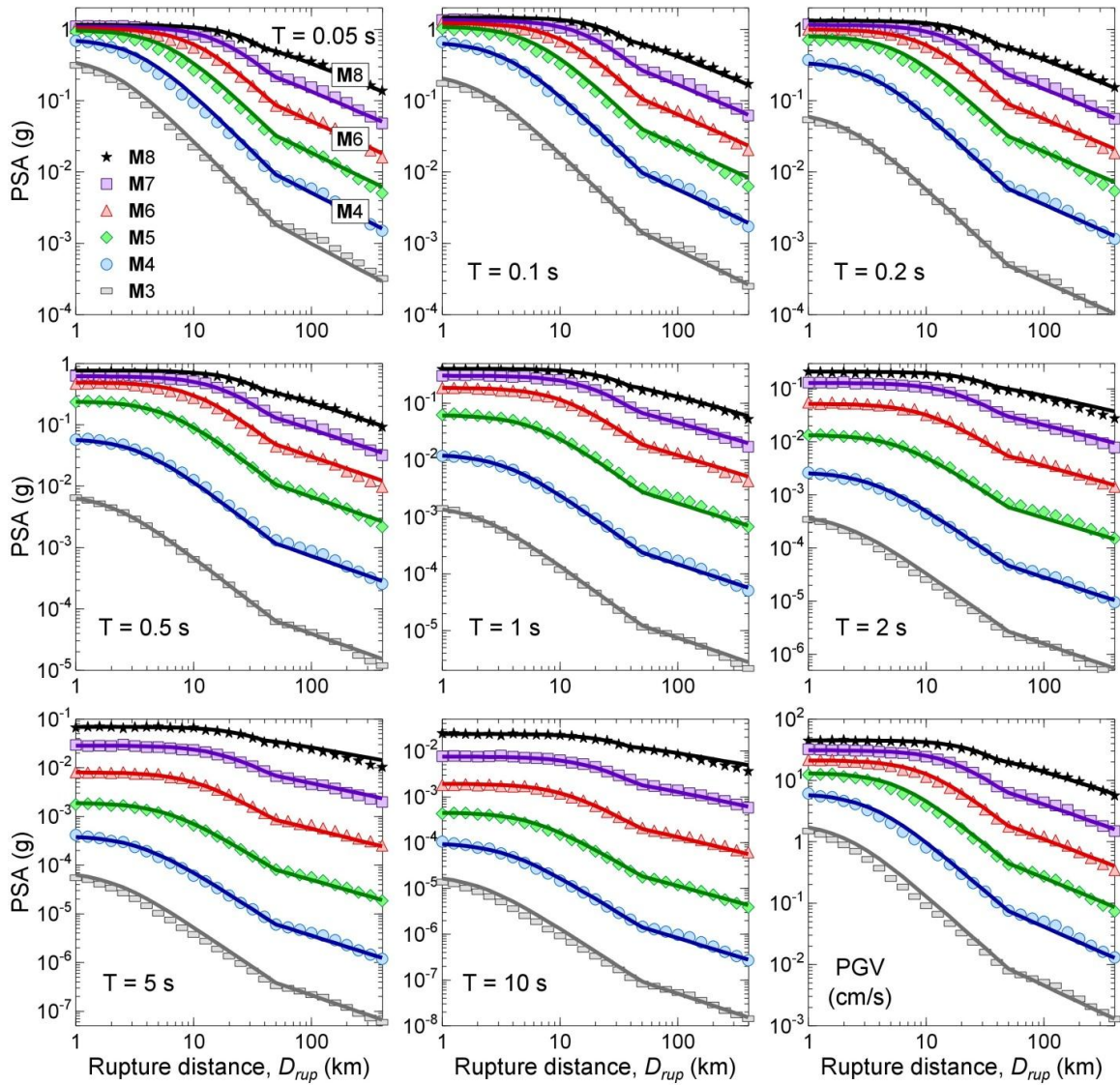
Figure 4.2 Simulations (symbols) in comparison to predictions of the generic GMPE (lines), as a function of rupture distance, for magnitudes M3 to M8 ($\Delta\sigma = 100$ bar, $V_{S30} = 760$ m/s). Note that no anelastic attenuation is included in either simulations or the generic GMPE because this effect is determined empirically.

We generate another set of simulations to calculate the stress adjustment factor. In this new set, we simulate ground motions for the same magnitude range (**M**3-**M**8) but for a fixed distance $D_{rup} = 1$ km and variable stress parameters (10 bar $\leq \Delta\sigma \leq 1000$ bar). Similar to the first set, 100 synthetic motions are generated for each combination of **M**,

D_{rup} and $\Delta\sigma$, and the geometric mean of the peak motions and response spectra are calculated.

The stress adjustment factor, $F_{\Delta\sigma}$, models the expected change in amplitudes when $\Delta\sigma$ is different than 100 bars. We determine $F_{\Delta\sigma}$ using simulations obtained at D_{rup} = 1 km, as:

$$F_{\Delta\sigma} = \ln Y_{\text{sim,1km}}(\mathbf{M}, \Delta\sigma) - \ln Y_{\text{sim,1km}}(\mathbf{M}, 100\text{bar}) \qquad (4.16)$$

where $Y_{\text{sim,1km}}(\mathbf{M}, \Delta\sigma)$ is the ground motion simulated at D_{rup} = 1 km for a given magnitude and stress, and $Y_{\text{sim,1km}}(\mathbf{M}, 100\text{bar})$ represents the ground motion simulated at D_{rup} = 1 km for the same magnitude, but for the reference stress ($\Delta\sigma$ = 100 bar). Figure 4.3 shows the required stress adjustment factors as a function of $\Delta\sigma$, for various magnitudes and periods. This factor has an increasing trend with the stress, where $F_{\Delta\sigma} = 0$ at $\Delta\sigma$ = 100 bar, by definition. The slope of $F_{\Delta\sigma}$, which is defined by coefficient $e_{\Delta\sigma}$ in Equation 4.4, represents the strength of the ground-motion scaling with the stress parameter. The steeper the slope, the larger the influence of stress on ground motions. As seen in Figure 4.3, $\Delta\sigma$ has significant influence at short periods (T < 0.2 s), regardless of magnitude. However, its effects weaken with increasing period, particularly for small-to-moderate magnitude events ($\mathbf{M}$ < 6). For large magnitudes, the $\Delta\sigma$-effects extend to longer periods due to the shifting of the two corner frequencies with magnitude.

We regress the values of $e_{\Delta\sigma}$ (calculated for each magnitude and period from the values of $F_{\Delta\sigma}$ using Equation 4.4) to the functional form:

$$e_{\Delta\sigma} = \begin{cases} s_0 + s_1\mathbf{M} + s_2\mathbf{M}^2 + s_3\mathbf{M}^3 + s_4\mathbf{M}^4 & \Delta\sigma \le 100 \text{ bar} \\ s_5 + s_6\mathbf{M} + s_7\mathbf{M}^2 + s_8\mathbf{M}^3 + s_9\mathbf{M}^4 & \Delta\sigma > 100 \text{ bar} \end{cases} \qquad (4.17)$$

where s_0 to s_9 are period-dependent model coefficients. We use two polynomials, because we require a different shape for the $e_{\Delta\sigma}$ values for $\Delta\sigma \le 100$ bar and $\Delta\sigma > 100$ bar; we constrain the regressions to attain $F_{\Delta\sigma} = 0$ at $\Delta\sigma$ = 100 bar. Figure 4.4 shows how the values of $e_{\Delta\sigma}$ vary with magnitude and period. The net effect of the stress parameter is complicated because of interactions between scaling of the high-frequency source amplitudes, shifting of the two corner frequencies, and changes in spectral sag between the corner frequencies. Additionally, the stress parameter affects the source duration,

which in turn influences the response spectral amplitudes. Coupling of all these factors in the response spectrum domain requires a high-order polynomial to satisfactorily model Δσ-scaling over a wide period range. The values of model coefficients for the stress adjustment factor are listed in Table A.2.
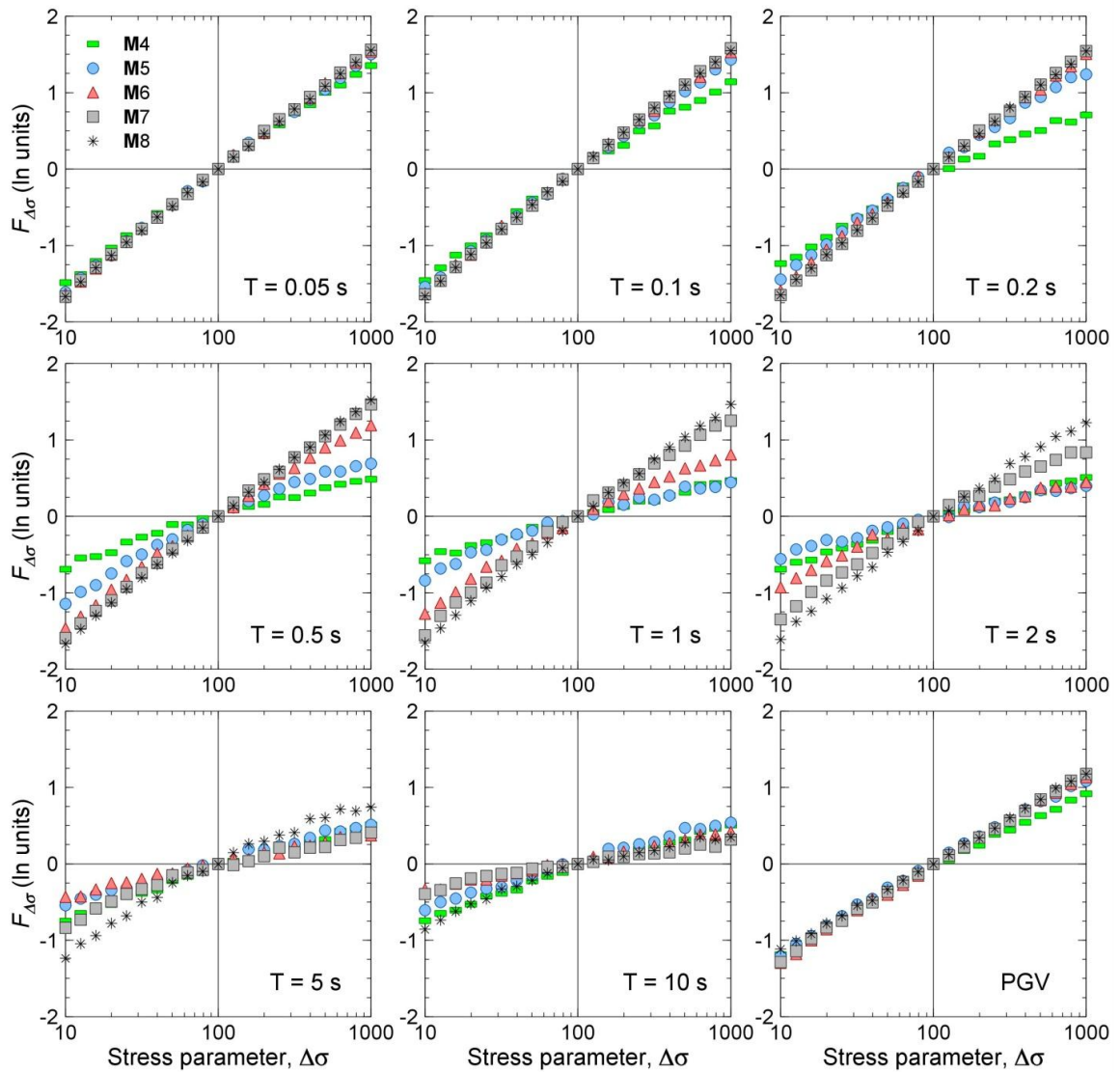
Figure 4.3 Stress adjustment factors ($F_{\Delta\sigma}$) determined from simulations.
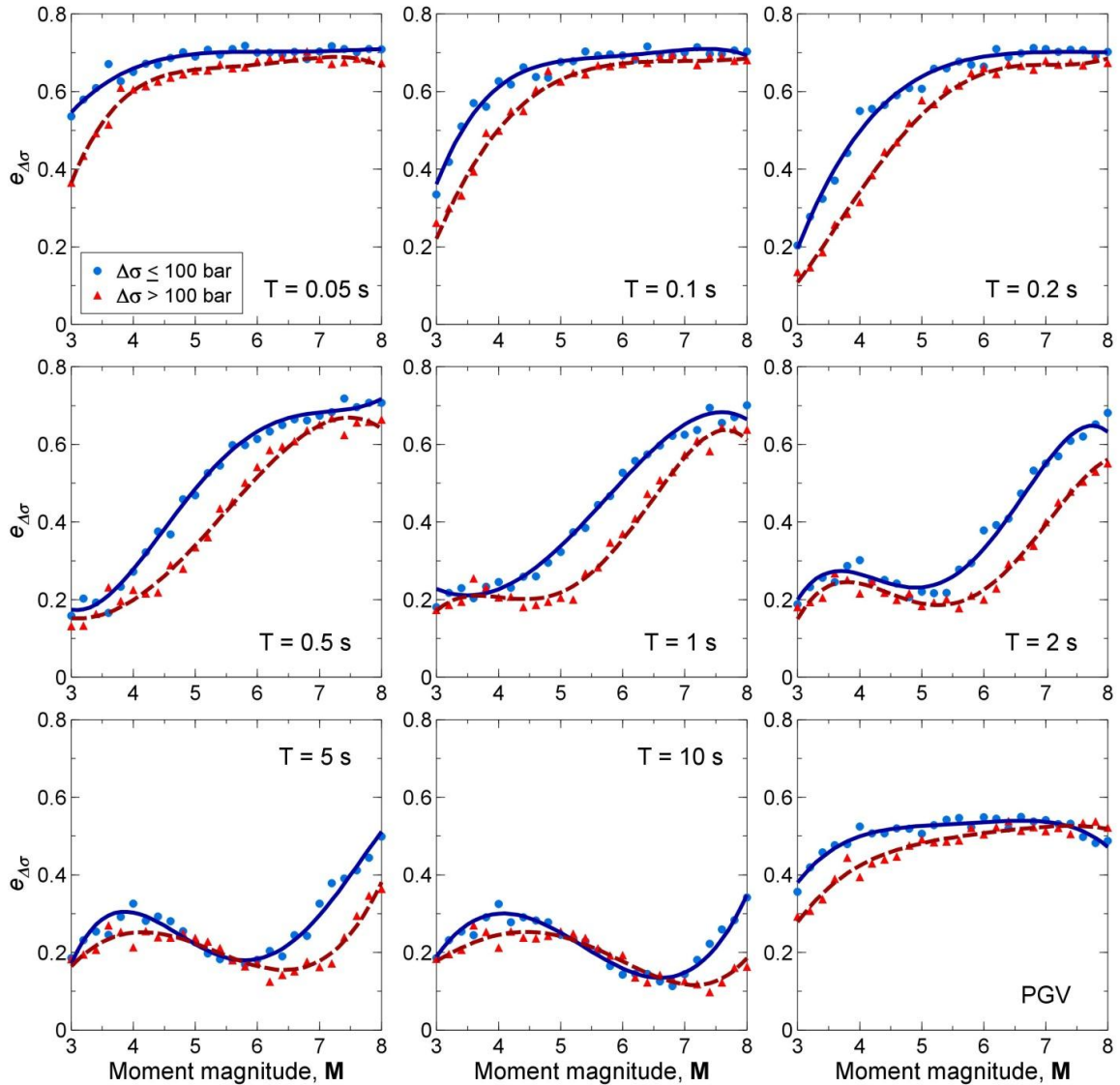
Figure 4.4 Stress-scaling coefficients ($e_{\Delta\sigma}$) obtained from simulations (symbols) and the fitted model (Equation 4.17).

4.4 Adjustment of the generic GMPE for a target region

The generic GMPE provides several advantages for the derivation of region-specific predictive models, particularly for data-poor regions. First, the generic GMPE effectively decouples the influence of basic source and attenuation parameters on ground-motion amplitudes. This allows the determination of regional values of modeling parameters from observed response spectral data in the target region. The generic GMPE is a self-

adjusting model, and is readily calibrated to the target region once the regional parameter values are plugged into the model. Thus, it does not require performing ground-motion simulations to determine of regional adjustment factors. Additionally, the generic values of source and attenuation parameters that are implicitly carried into the generic model are known. Therefore, the modeling parameters that require modification for regional use can easily be determined, if the source and attenuation attributes of earthquakes are known for the target region. This provides effective and transparent control over the transferable factors between regions. Finally, the generic GMPE can be used to create a set of alternative predictive models for the region of interest, by considering a range of possible parameter values that might be reasonable for the region. This allows modeling of the epistemic uncertainty in predicted amplitudes for probabilistic seismic hazard analysis applications in the target region.

Adjustment of the generic model to a specific region includes any required modifications to the source and attenuation parameters, as well as determination of an empirical calibration factor that accounts for residual effects that are missing and/or different in the simulations compared to the observed motions. In this study, we assume that the magnitude (F_M) and saturation (h) effects determined from simulations are transferable to other regions. However, the stress parameter may vary regionally; the generic GMPE is directly adjusted for this effect when the regional value of stress parameter is plugged into $F_{\Delta\sigma}$. The required modifications for regional attenuation can be done by means of Z and γ. We recommend keeping the presumed Z model (geometric spreading) as it is defined in the generic model, unless there is compelling evidence for its modification. The anelastic attenuation coefficient, γ, is determined using empirical data at regional distances for the region of interest; such data can be obtained from weak-motion studies. The calibration factor, C, is calculated through the analysis of residuals between observed motions in the target region and the GMPE, after application of the regional values of $\Delta\sigma$, Z and γ.

4.5 An example application: Adjustment of the generic GMPE for CENA

As an example implementation of the method, we adjust the generic GMPE for the central and eastern North America (CENA) using ground motions obtained in the region. We use the database of PGA, PGV and 5%-damped PSA from the NGA-East flatfile (see Data and Resources), for CENA earthquakes of $\mathbf{M} \geq 3.0$ that were recorded by at least three stations within 600 km. We consider both natural and induced earthquakes in the region. However, ground motions recorded in the Gulf Coast regions are excluded due to considerably different attenuation attributes in this region (EPRI, 2004). We use the average orientation-independent horizontal-component ground motions calculated based on the RotD50 measure (Boore, 2010), as provided in NGA-East flatfile; this is approximately equivalent to geometric mean motions as provided in the simulations. Figure 4.5 shows the magnitude-distance distribution of the selected records. Figure 4.6 shows a map of the epicenters of the study events and Figure 4.7 is a map of stations and their site condition.
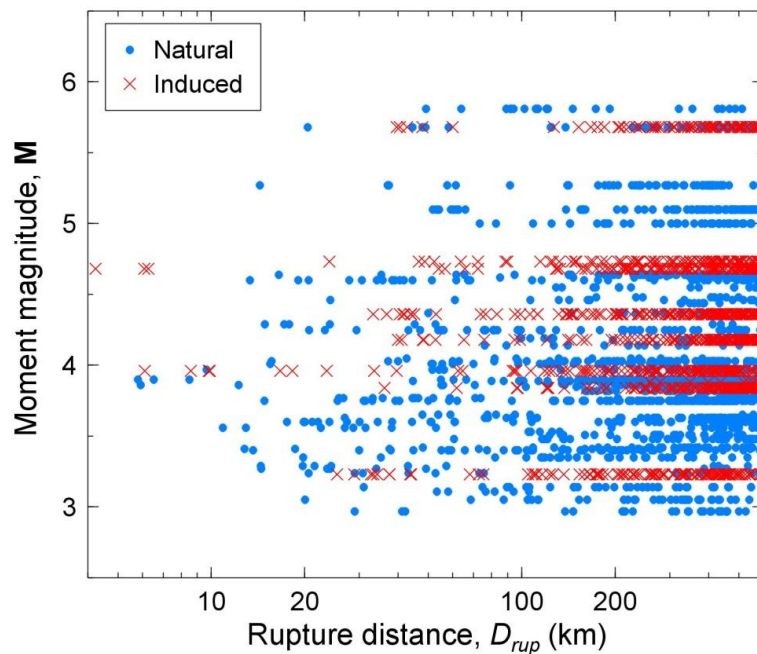
Figure 4.5 Magnitude-distance distribution of the selected ground motions in CENA. Ground motions recorded beyond 600 km are not considered.
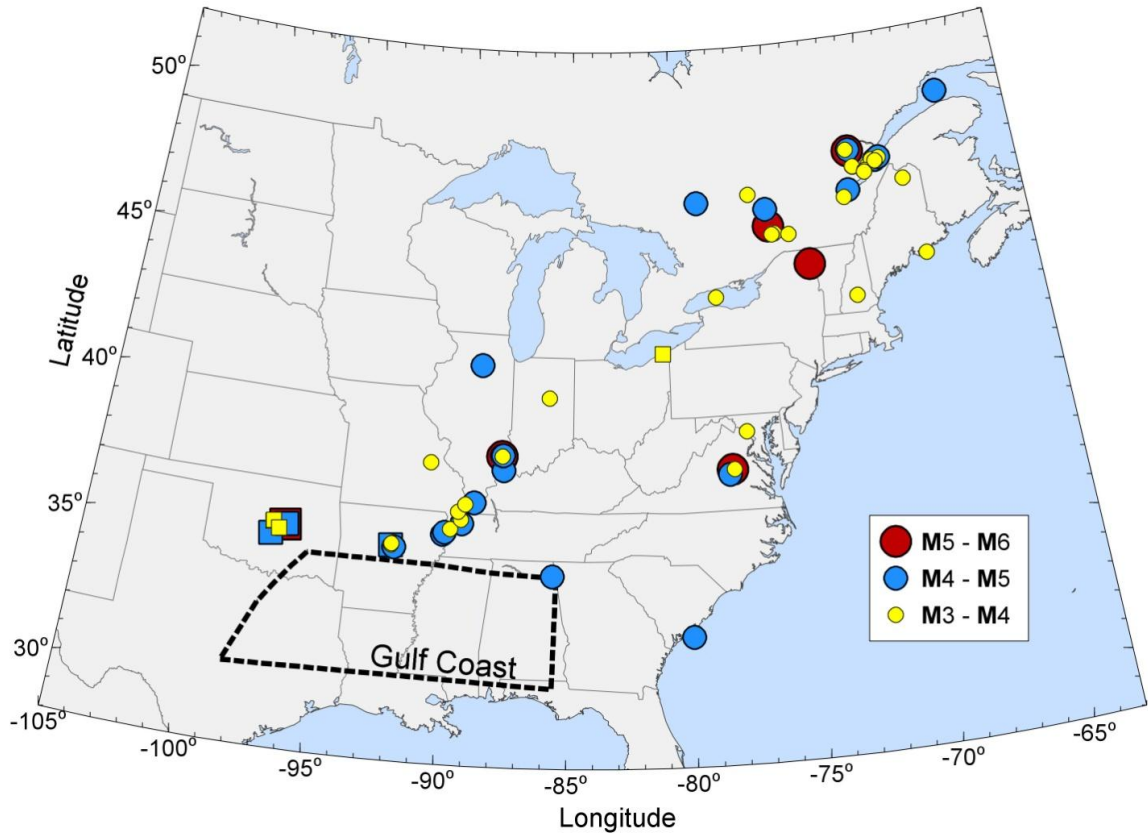
Figure 4.6 Epicenters of study events in central and eastern North America (CENA). Circles show epicenter locations of naturally-occurring earthquakes and squares indicate events that have been flagged as potentially induced in the NGA-East flatfile. Dashed line marks the Gulf Coast region.
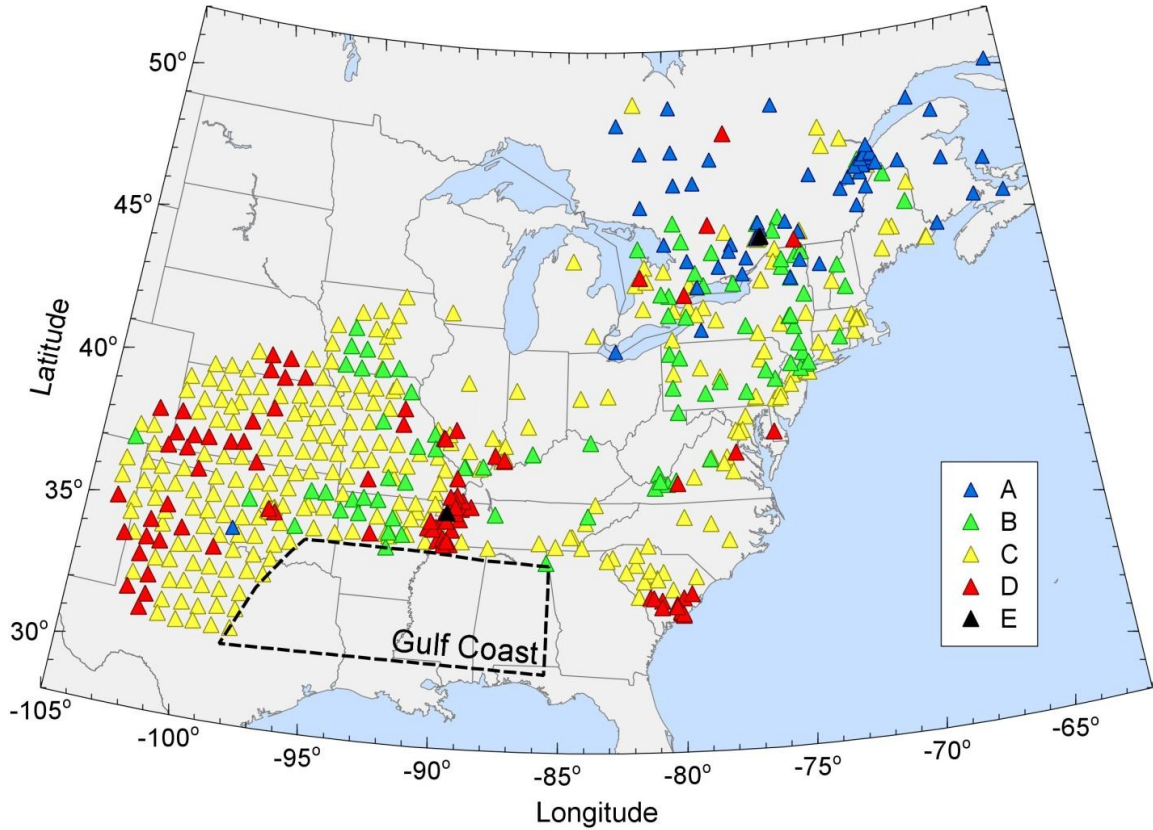
Figure 4.7 Locations of recording stations and their NEHRP (National Earthquake Hazards Reduction Program) site classification: A: $V_{S30} > 1500$ m/s, B: 760 m/s $< V_{S30} \leq 1500$ m/s, C: 360 m/s $< V_{S30} \leq 760$ m/s, D: 180 m/s $< V_{S30} \leq 360$ m/s and E: $V_{S30} \leq 180$ m/s (NEHRP, 2000). We excluded stations located in the Gulf Coast region (dashed line).

In the analysis, we consider response spectra up to a maximum usable period to reduce the impact of long-period noise on the adjusted GMPE. For a given ground-motion record, the maximum usable period, T_{max}, is defined as

$$T_{max} = \frac{1}{\max[(1.25 f_{lc}), (f_{min})]} \tag{4.18}$$

where f_{lc} is the low-cut filter frequency of the record reported in the NGA-East flatfile and f_{min} is the limiting frequency below which spectral amplitudes are assumed to be noise-dominated. We describe f_{min} as

$$f_{min} = max[(0.1), (10^{0.75-\mathbf{M}/3})] \tag{4.19}$$

Equation 4.19 is defined such that it provides an overall agreement with the geometric mean of the factored filter frequencies (i.e., $1.25f_{lc}$), as seen in Figure 4.8. For **M** < 6, the f_{min} model given for CENA is relatively less conservative than that was used for California by Yenier and Atkinson (2015) because ground motions attenuate more slowly in CENA, providing useable signal to greater distances.
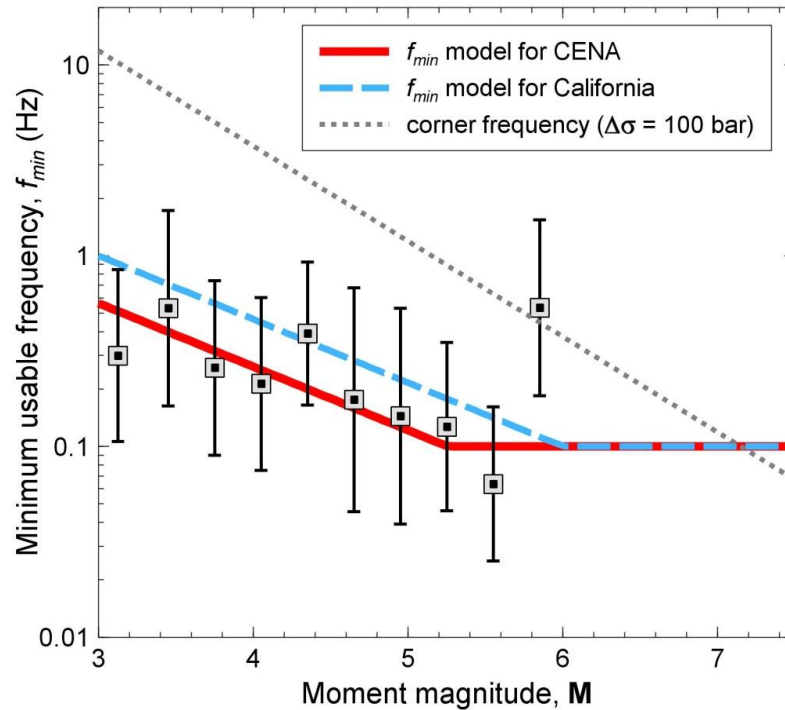
Figure 4.8 Minimum usable frequency (f_{min}) model considered for records in CENA (solid line). Squares indicate the geometric mean of the factored low-cut filter frequencies (i.e., $1.25f_{lc}$) determined for evenly-spaced magnitude bins. The error bars represent one standard deviation about the mean values. The dashed line indicates the f_{min} model used for California by Yenier and Atkinson (2015). The dotted line shows the corner frequency of the Brune (1970) source model for $\Delta\sigma = 100$ bar.

We correct the recorded ground-motion amplitudes to the equivalent values for NEHRP B/C site conditions ($V_{S30} = 760$ m/s) using the F_S function adopted from BSSA14. This function is based on the values of V_{S30} and PGA_r for each record, where the V_{S30} values are given in the NGA-East flatfile, and we assume that PGA_r can be reasonably estimated

from BSSA14 as an approximation. We deliberately use BSSA14 rather than a CENA GMPE for this purpose, as we do not wish the higher frequency content in CENA to impose greater nonlinearity.

Regional Attenuation

Empirical studies suggest that the geometrical spreading of Fourier amplitudes in CENA can be adequately described as $R^{-1.3}$ within 50 km and $R^{-0.5}$ at further distances (Atkinson and Boore, 2014; Babaie Mahani and Atkinson, 2012). We therefore use the generic bilinear Z model (b_1 = -1.3, b_2 = -0.5 and R_t = 50 km) without modification. The only attenuation adjustment needed is for the regional anelastic attenuation. As described in the methodology presented earlier, we determine the regional anelastic attenuation (γ_{CENA}) from the empirical data using:

$$\ln Y_{B/C,ij} - \left(F_{M,i} + F_{Z,ij} \right) = E_i + \gamma_{CENA} D_{rup,ij} \tag{4.20}$$

where $Y_{B/C,ij}$ represents the B/C-corrected motion for event i and station j. $F_{M,i}$ and $F_{Z,ij}$ are the magnitude and geometrical spreading functions evaluated for the known magnitude and distance ($D_{rup,ij}$) of the record, respectively. The E_i term is an event term, which provides the average adjustment required to match observed amplitudes from event i. Its value can be attributed to two main factors: (i) the difference between the reference stress implicitly carried by the F_M function (100 bars) and its true value for the ith event (modeled by $F_{\Delta\sigma}$), and (ii) the overall difference between synthetics and observed motions in CENA (modeled by C). We calculate the regional anelastic attenuation coefficient (γ_{CENA}) and event terms (E_i) for each oscillator period and ground motion parameter; the values of the γ_{CENA} term are listed Table A.3.

Regional Stress Parameter

The stress parameter is often determined by matching the predicted and observed spectral amplitudes at short periods for the specified moment. However, this approach results in a non-unique solution for $\Delta\sigma$ due to the trade-off between earthquake source and attenuation (Boore et al., 2010; Yenier and Atkinson, 2014). Moreover, $\Delta\sigma$ has little

effect on the response spectrum at long periods (Figures 4.3), especially for small-to-moderate events, restricting our ability to calibrate the response spectral amplitudes at long periods. To ensure a model calibration that is consistent over a wide period range, we determine the stress parameter by matching the observed spectral shape for the known moment (i.e. the corner frequency), rather than spectral amplitudes. This breaks the trade-off between source and attenuation parameters, transferring the overall amplitude difference to the calibration factor C (Yenier and Atkinson, 2015). Following this technique, we use a grid search to determine $\Delta\sigma$ for each event separately. We select the best-fitting $\Delta\sigma$ based on the minimum standard deviation of residuals between E_i and $F_{\Delta\sigma}$, over a wide period range (0.01 s $\leq$ T $\leq$ 10 s); by minimizing the standard deviation of residuals, we are effectively finding the best shape, rather than the best level.

Figure 4.9 shows the shape-based $\Delta\sigma$ values obtained from CENA events as a function of focal depth (d). The mean stress determined for evenly-spaced focal depth bins shows an increasing trend from $\Delta\sigma \approx 30$ bar at $d = 2.5$ km to $\Delta\sigma \approx 250$ bar at $d = 10$ km; it remains relatively constant at greater depths. Figure 4.10 shows the best-fitting $\Delta\sigma$ as a function of magnitude. For $\mathbf{M} < 5$, the stress parameter shows large variability. Despite the large variation of $\Delta\sigma$ values at small magnitudes, the depth effect is clearly visible by the distinct separation of depth-clustered stresses. For $\mathbf{M} > 5$, the stress parameter attains a value of $\Delta\sigma \approx 300$ bar, on average; we note that this is about two times the corresponding value for California events.

We regress the best-fitting $\Delta\sigma$ values to develop a regional stress model for CENA. Based on the observations made in Figures 4.9 and 4.10, we constrain the model to attain $\Delta\sigma = 300$ bar for $\mathbf{M} \geq 5$ and $d \geq 10$ km. The mean value of the stress parameter for earthquakes in CENA is expressed as:

$$\ln\Delta\sigma_{CENA} = 5.704 + \min[0,\ 0.29(d - 10)] + \min[0,\ 0.229(\mathbf{M} - 5)] \qquad (4.21)$$

The estimates of Equation 4.21 for different magnitudes and depths are shown in Figures 4.9 and 4.10. The mean residuals between the observed and predicted $\Delta\sigma$ values attain values around zero, as illustrated in Figure 4.11. Overall, the proposed $\Delta\sigma$ model

provides a good agreement with the Δσ values determined from CENA events based on the inferred spectral shape.
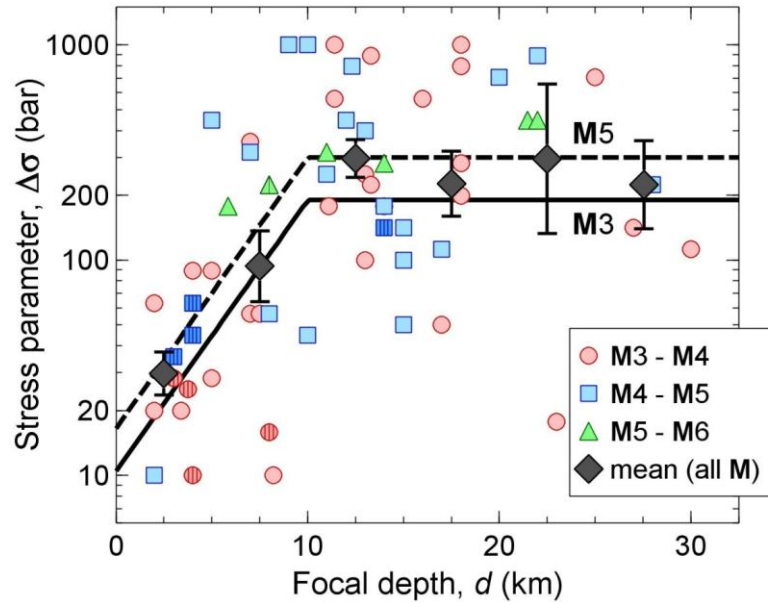
Figure 4.9 Best-fitting stress parameters (Δσ) determined for CENA events as a function of focal depth (*d*). Δσ values are clustered into different magnitude bins as shown in the legend. Hatched symbols indicate Δσ values obtained from the induced events. Diamonds represent the mean Δσ calculated for evenly-spaced focal depth bins over all magnitudes, and the error bars show standard error about the mean stress. Lines indicate the derived Δσ model (Equation 4.21) evaluated for M3 (solid) and M5 (dashed).
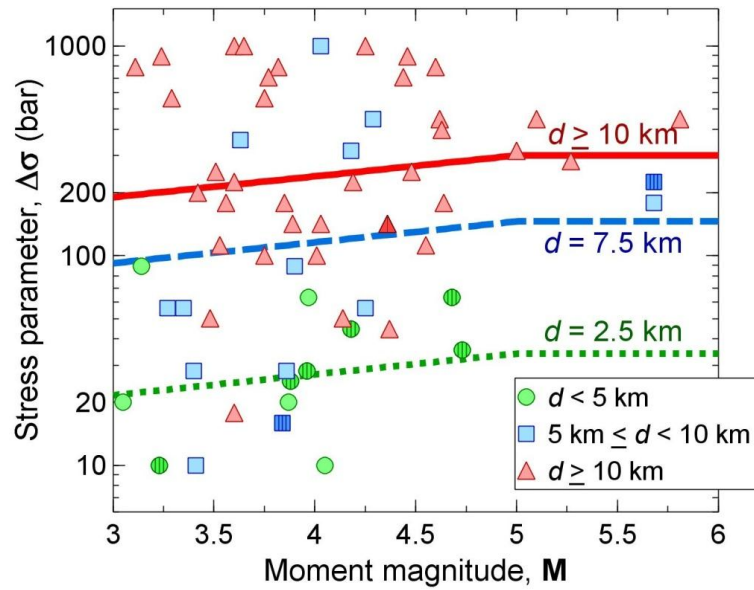
Figure 4.10 Best-fitting stress parameters ($\Delta\sigma$) determined based on matching the observed response spectral shape for CENA events, as a function of magnitude. $\Delta\sigma$ values are clustered into different focal depth (d) bins as shown in the legend. Hatched symbols show $\Delta\sigma$ values obtained from the induced events. Lines indicate the derived $\Delta\sigma$ model (Equation 4.21) evaluated for $d = 2.5$ km (dotted) $d = 7.5$ km (dashed) and $d \geq 10$ km (solid).
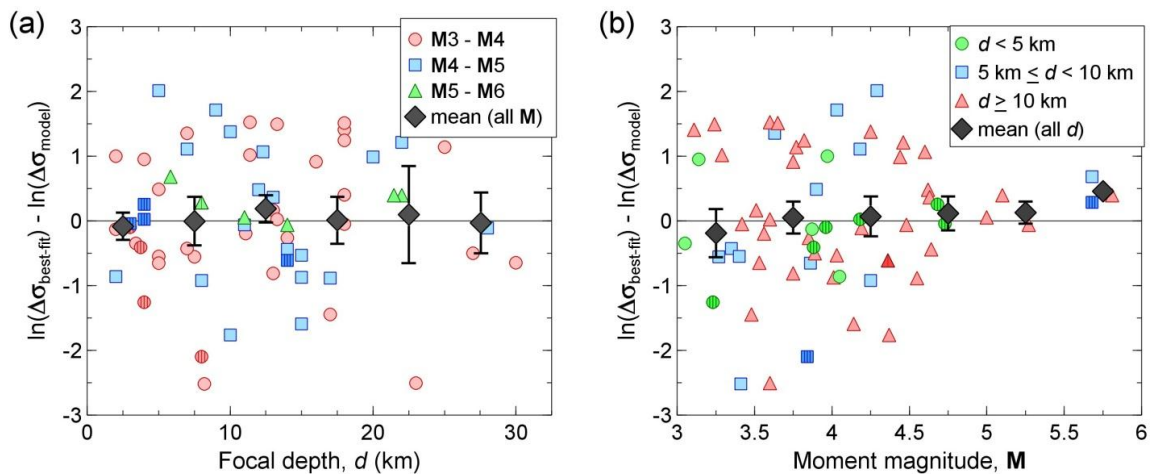
Figure 4.11 Residuals between the best-fitting $\Delta\sigma$ values obtained from CENA events and the estimates of the $\Delta\sigma$ model (Equation 4.21) evaluated for the known magnitudes and focal depths of the study events.

Calibration Factor

An overall calibration factor is needed to reconcile the predictions with observed amplitudes in the target region, accounting for effects missing and/or different in simulations (e.g., discrepancies between the assumed and true values of crustal properties, site amplification, κ_0 and path duration). We calculate the calibration factor based on the analysis of residuals:

$$\delta_{ij} = \ln Y_{B/C,ij} - \left(F_{M,i} + F_{\Delta\sigma CENA,i} + F_{Z,ij} + \gamma_{CENA} D_{rup,ij} \right) \tag{4.22}$$

where δ_{ij} represents the residual for the ground motion obtained from event i at station j, for a given spectral period or peak motion. $F_{\Delta\sigma CENA,i}$ is the stress adjustment factor evaluated for $\Delta\sigma$ from Equation 4.21 for the known magnitude and focal depth of event i. The last term accounts for the regional anelastic attenuation determined earlier.

Figure 4.12 shows the event residuals ($\delta_i = \sum \delta_{ij}/n_i$, where n_i is the number of records obtained from event i; $n_i \geq 3$ at a given period) as a function of magnitude. δ_i generally attains negative values and appears to be randomly distributed, showing no distinct attributes for natural and induced events. The mean δ_i values determined at evenly-spaced magnitude bins shows no magnitude-dependent trends, in general. This suggests that the magnitude scaling of ground motions in CENA is well captured by the F_M function, at least for the available data. Based on these observations, we calculate an event-based calibration factor ($C_{e,CENA}$) as the average of δ_i values over all magnitudes, for each spectral period/peak motion. The $C_{e,CENA}$ term fluctuates with period between 0 and -0.5 (ln units) for periods $T < 3$ s and attains positive values with an increasing trend at larger periods, as shown in Figure 4.13. This increasing trend at long periods may be due to the fact that stochastic simulations are inherently limited in their ability to generate the coherent motions seen at long periods. We describe $C_{e,CENA}$ as:

$$C_{e,CENA} = \begin{cases} -0.25 + \max[0, \ 0.39\ln(T/2)] & T \leq 10 \text{ s} \\ -0.25 & \text{for PGA} \\ -0.21 & \text{for PGV} \end{cases} \tag{4.23}$$
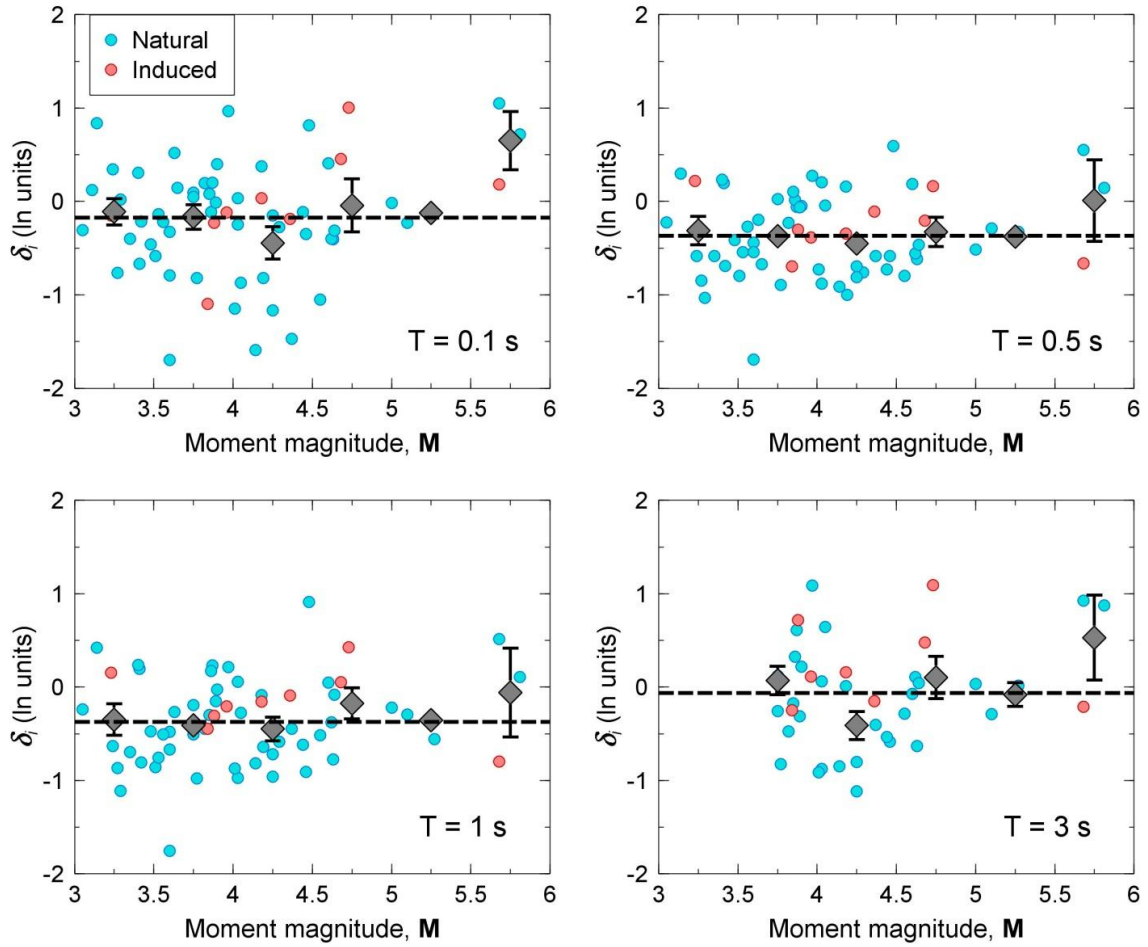
Figure 4.12 Average of residuals determined for each event that have at least 3 observations at a given period (δ_i, circles). Diamonds show mean of δ_i values determined for evenly-spaced magnitude bins, and error bars represent the standard error about the mean. Dashed lines indicate the event-based calibration factors (C_e) that is defined as the average of δ_i values over all magnitudes, at a given period.
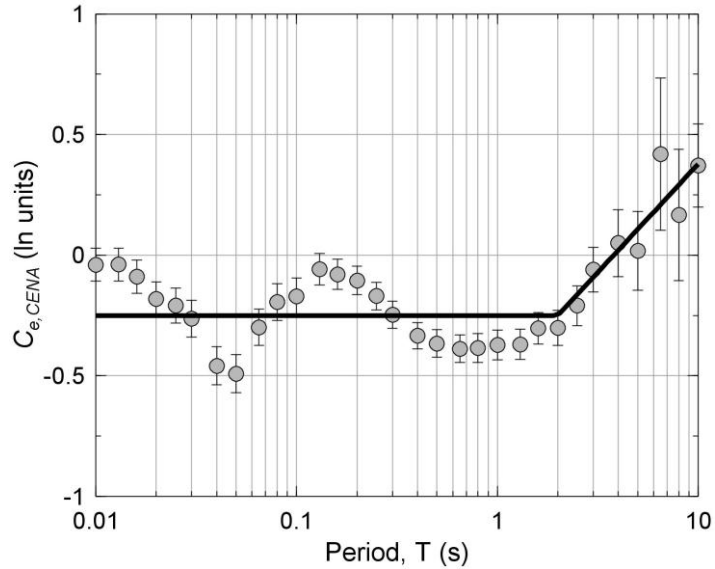
Figure 4.13 Event-based calibration factor for CENA (solid line). Circles indicate average $C_{e,CENA}$ values determined for all events at each period, and error bars represent the standard error about the mean.

We subtract the event-based δ_i term from the individual residuals to calculate the average residual at each station (i.e., $\delta_j = \sum(\delta_{ij} - \delta_i)/n_j$, where n_j is the number of observations at station j; $n_j \geq 3$ at a given period). Figure 4.14 illustrates the variation of δ_j as a function of V_{S30}. The mean δ_j determined for NEHRP C sites attain near zero value, in general, suggesting that the BSSA14 site amplification model is reasonable for this site class. However, ground motions on NEHRP B sites are underpredicted by ~15% and ground motions at NEHRP D sites are overpredicted by ~20%, on average. The mean δ_j determined for NEHRP A sites is near zero, expect for short periods. For T < 0.1 s, ground motions at NEHRP A sites are underpredicted by ~20%, on average.
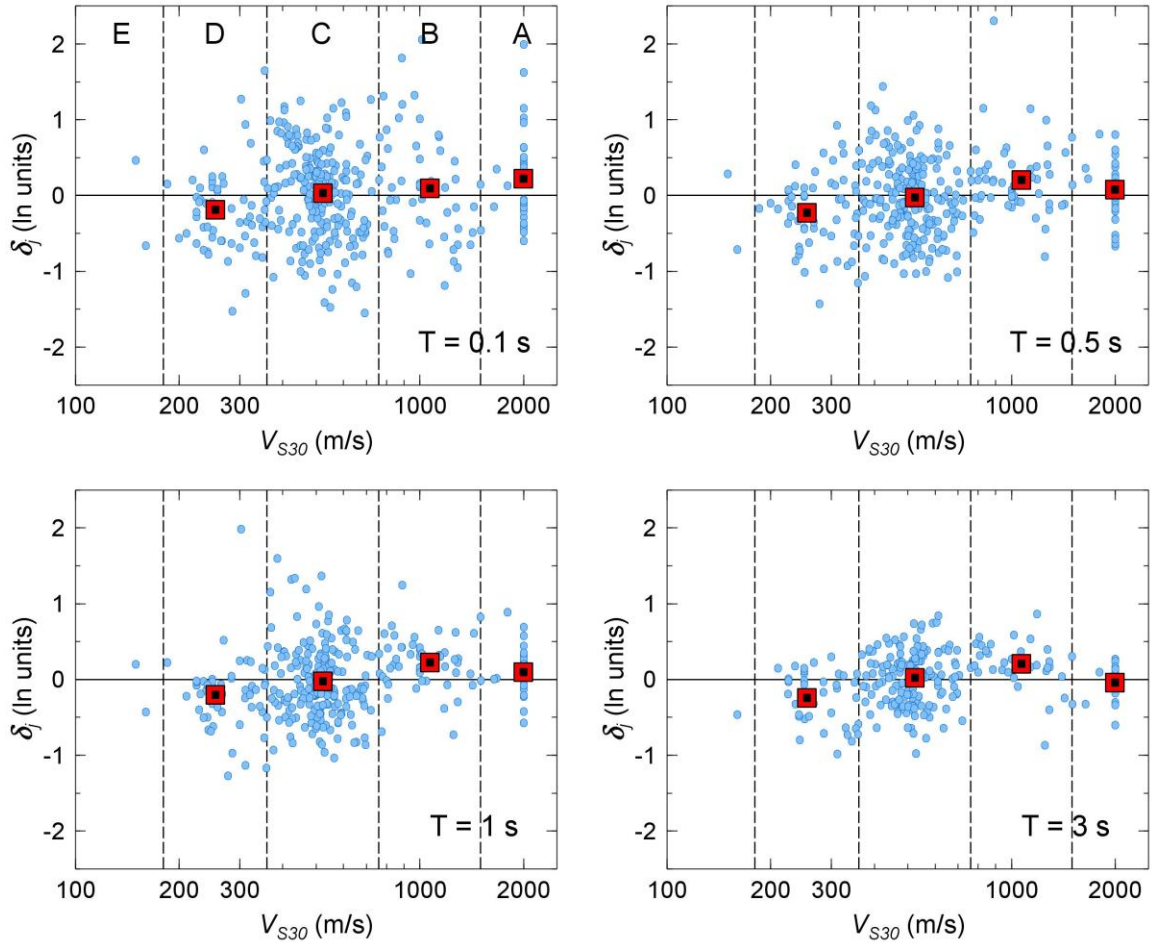
Figure 4.14 Event-corrected average residuals for each station (δ_j, circles) as a function of V_{S30}. Mean of δ_j values for NEHRP site classes are shown by squares (standard errors for the mean values are smaller than the symbols).

Finally, we correct the individual residuals for the event and station terms (i.e., $\delta'_{ij} = \delta_{ij} - \delta_i - \delta_j$) to assess the performance of the assumed geometrical spreading function. Figure 4.15 compares the δ'_{ij} values as a function of rupture distance. The mean δ'_{ij} determined for log-spaced distance bins attains near zero values at $D_{rup} > 150$ km, suggesting that γ_{CENA} parameter can successfully represent the overall attenuation at far distances. However, the mean δ'_{ij} deviates from the horizontal zero-line and decreases with distance for $D_{rup} < 150$ km, as shown in the figure. This discrepancy might be attributable to the path-duration model. In the simulations, we used a path-duration model derived primarily from observed motions in WNA. Boore and Thompson (2015) recently reported that the

path duration in ENA is much longer than that in WNA, particularly at distances less than 150 km. This difference could result in some overestimation of CENA motions for $D_{rup} <$ 150 km because the presumed WNA path-duration model is implicitly carried via the F_Z function to CENA.
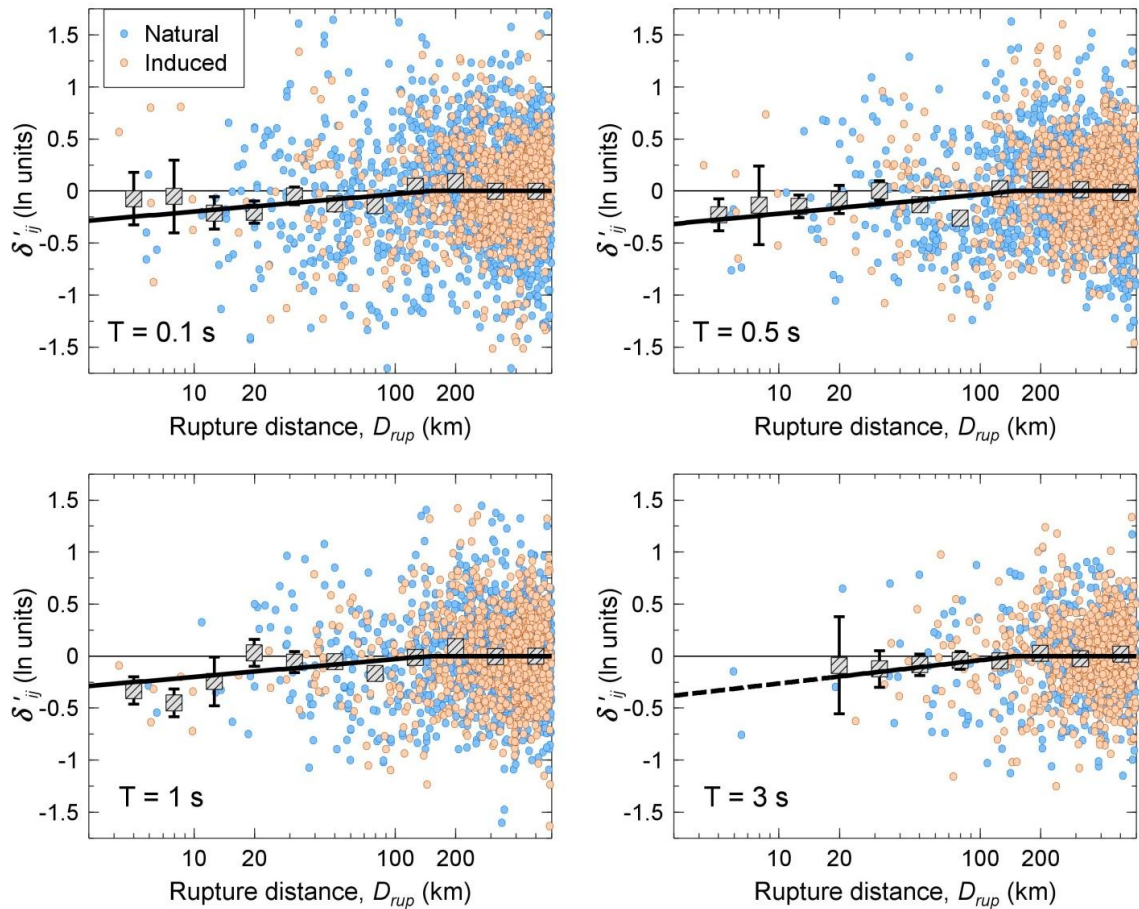
Figure 4.15 Event- and site-corrected residuals (δ'_{ij}) as a function of distance, for ground motions obtained from natural and induced events. Squares show the mean δ'_{ij} values determined for logarithmically-spaced distance bins and error bars indicate the standard error about the mean. Solid line represents the fitted path-related calibration model (C_p).

We consider an additional minor calibration term for regional differences in the path duration. We describe this path-related calibration ($C_{p,CENA}$) as:

$$C_{p,CENA} = \begin{cases} \Delta b_3 \ln(R/150) & R \leq 150 \; km \\ 0 & R > 150 \; km \end{cases} \tag{4.24}$$

where Δb_3 represents a calibration for the geometrical attenuation rate in response spectrum domain. We determine the Δb_3 term from the regression of δ'_{ij} based on Equation 4.24 at each period and peak motion separately. Figure 4.16 shows the variation of Δb_3 coefficients as a function of period. Its value could be determined only up to T = 3 s due to the limited data at $D_{rup} < 100$ km for longer periods. We smooth Δb_3 values as:

$$\Delta b_3 = \begin{cases} \min\{0.095, \; 0.030 + \max[0, \; 0.095\ln(T/0.065)]\} & T \leq 10 \; s \\ 0.030 & \text{for PGA} \\ 0.052 & \text{for PGV} \end{cases} \tag{4.25}$$
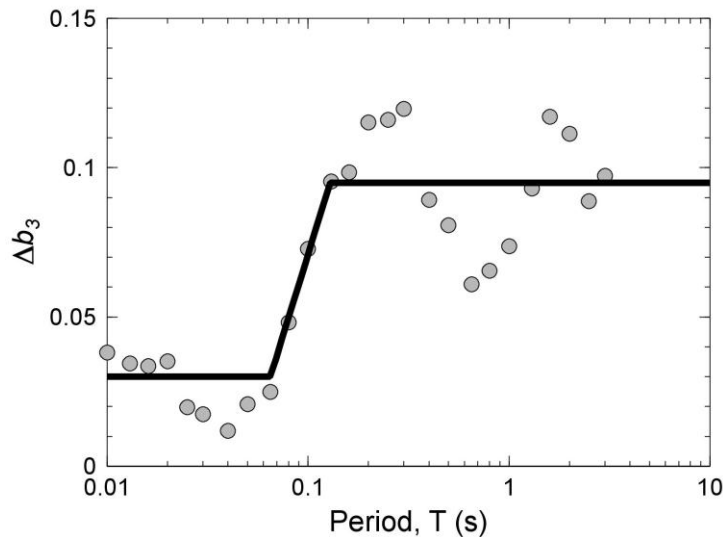
Figure 4.16 Δb_3 values determined from regression analysis (cicles) and the smoothed Δb_3 model for CENA (Equation 4.25, solid line).

The total calibration needed for the CENA-adjusted GMPE is the summation of $C_{e,CENA}$ and $C_{p,CENA}$ terms. This closes the systematic gaps between simulation-based predictions and observed motions in CENA. The resultant CENA-adjusted prediction equation is given as:

$$\ln Y_{CENA} = F_M + F_{\Delta\sigma CENA} + F_Z + \gamma_{CENA}D_{rup} + F_S + C_{e,CENA} + C_{p,CENA} \qquad (4.26)$$

Figure 4.17 illustrates PSA values predicted from Equation 4.26 for magnitudes **M**4 to **M**8 as a function of rupture distance, for NEHRP B/C site condition (V_{S30} = 760 m/s). The B/C-corrected ground motions obtained from earthquakes in CENA are also shown in the figure, for two magnitude ranges: **M**3.5-**M**4.5 and **M**4.5-**M**5.5. The CENA-adjusted GMPE is in good agreement with the empirical data, where available, and provides seismologically-informed predictions of average ground motions for moderate-to-large magnitudes (**M** > 6).
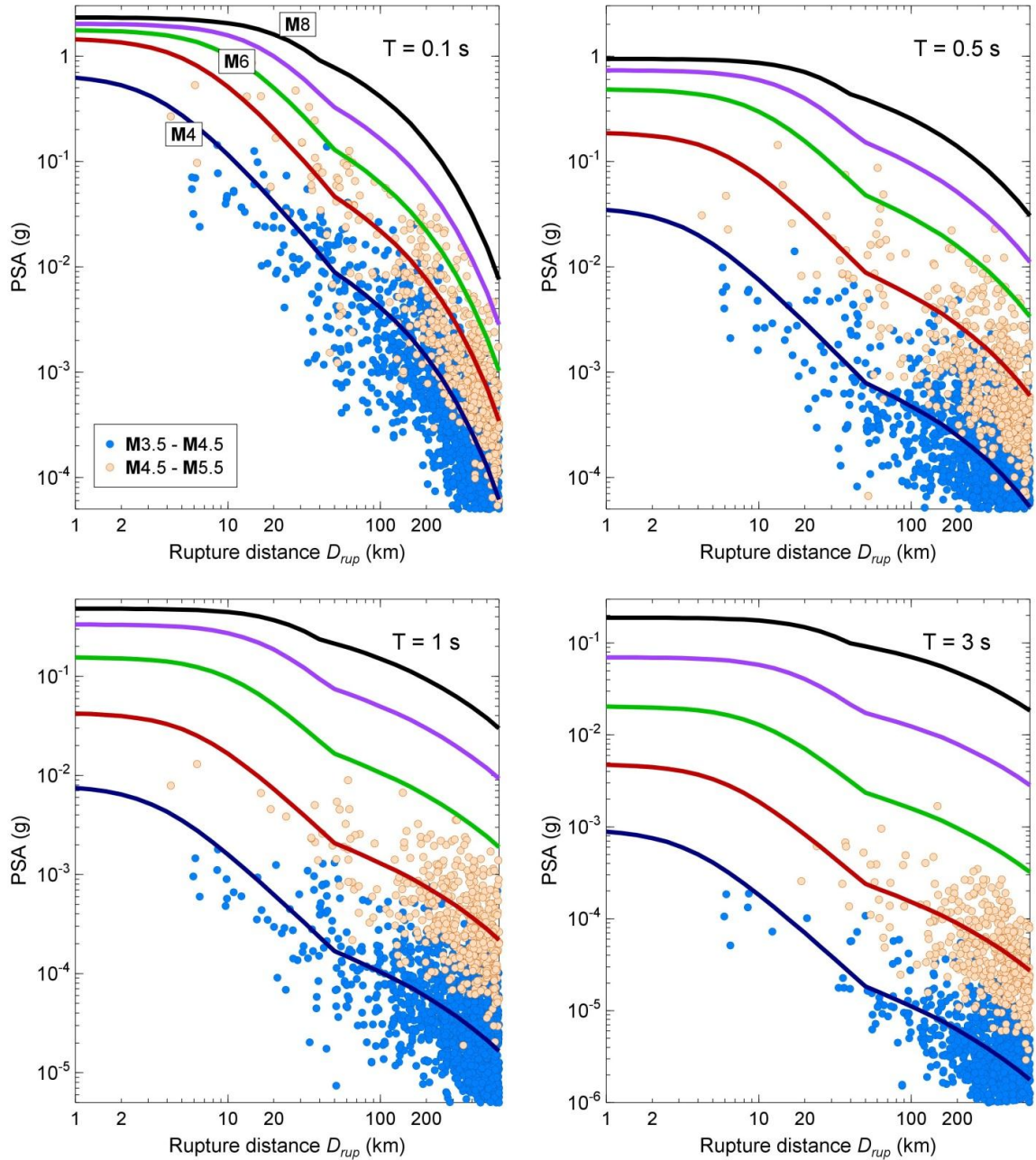
Figure 4.17 PSA predictions from the CENA-adjusted GMPE (Equation 4.26) for magnitudes **M**4 to **M**8 (focal depth, $d = 10$ km), for $V_{S30} = 760$ m/s (lines). Circles represent the B/C-corrected ground motions obtained from earthquakes in CENA for two magnitude ranges: **M**3.5-**M**4.5 and **M**4.5-**M**5.5.

We determine the anelastic attenuation coefficient and calibration factor for California in order to enable the comparison the CENA-adjusted model with the California predictions. We followed the methodology described above, using the observed ground motions in California that were selected from NGA-West2 database by Yenier and Atkinson (2015). The prediction equation for California is given as:

$$\ln Y_{California} = F_M + F_{\Delta\sigma,California} + F_Z + \gamma_{California}D_{rup} + F_S + C_{California} \quad (4.27)$$

where $F_{\Delta\sigma,California}$ is the stress adjustment factor evaluated for the mean stress in California ($\Delta\sigma_{California}$). Yenier and Atkinson (2015) defined $\Delta\sigma_{California}$ as a function of magnitude and focal depth (in km):

$$\ln\Delta\sigma_{California} = [2.18 + \min\{0, \ \max[0.06, \ 0.3 - 0.04\mathbf{M}](d - 12)\}]\ln 10 \quad (4.28)$$

The anelastic attenuation coefficients for California ($\gamma_{California}$) are provided in Table A.3. We define the overall calibration factor for California ($C_{California}$) as:

$$C_{California} = \begin{cases} \max[-0.25, \ -0.25 + 0.36\ln(T/0.1)] & T \leq 0.2 \text{ s} \\ \max[0, \ 0.39\ln(T/1.5)] & 0.2 \text{ s} < T \leq 10 \text{ s} \\ -0.25 & \text{for PGA} \\ -0.15 & \text{for PGV} \end{cases} \quad (4.29)$$

Note that the California model does not require calibration for the path effects (i.e., $C_{p,California} = 0$) because simulations that were used for the derivation of the generic GMPE were generated based on the WNA-compatible duration model of Boore and Thompson (2014). Figures 4.18 and 4.19 illustrate the comparison of PSA predictions for CENA and California as a function of distance and period, respectively. The effects of differences in regional stress parameter and anelastic attenuation between California and CENA are apparent in these figures.
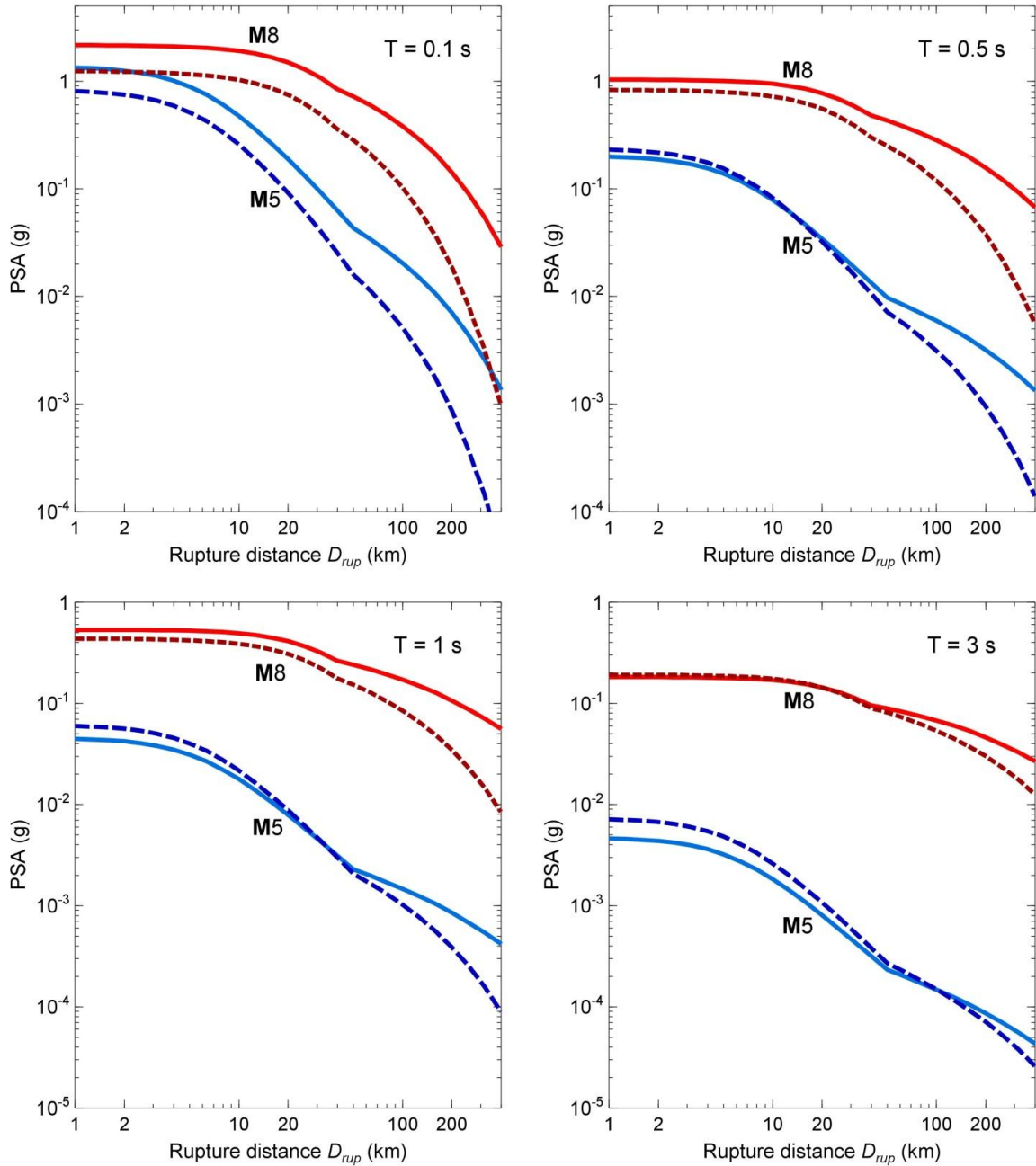
Figure 4.18 Comparison of PSA predictions for CENA (Equation 4.26, solid line) and California (Equation 4.27, dashed line) for **M**5 and **M**8 (focal depth, d = 10 km), for V_{S30} = 760 m/s.
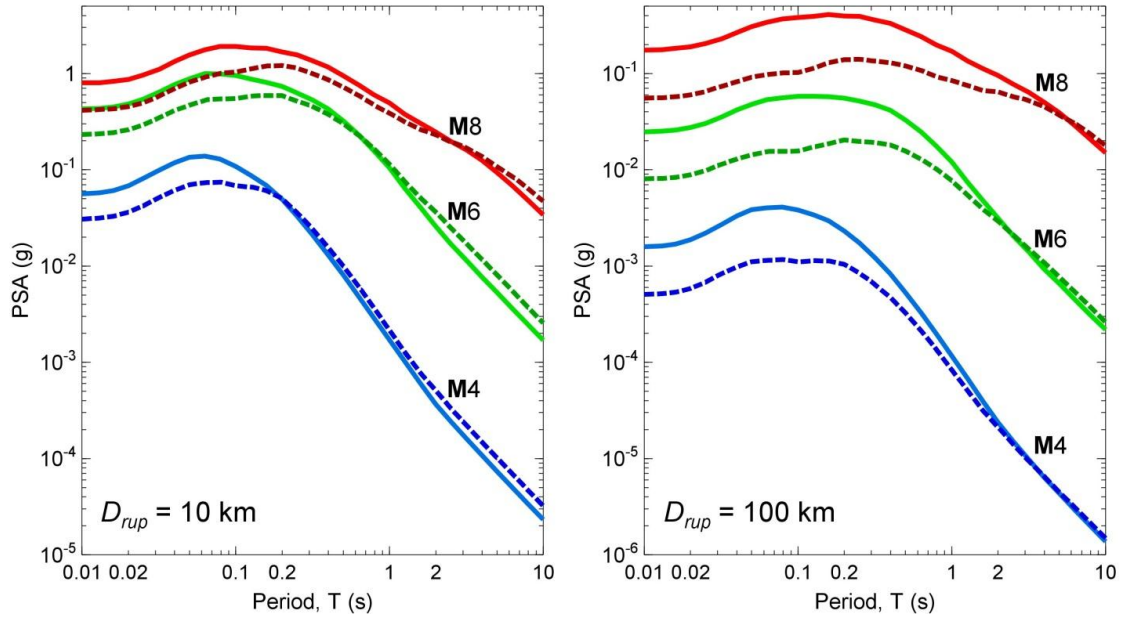
Figure 4.19 Comparison of predicted response spectra for CENA (Equation 4.26, solid line) and California (Equation 4.27, dashed line) at D_{rup} = 10 km and D_{rup} = 100 km, for **M**4 to **M**8 (focal depth, d = 10 km). The response spectra are computed for NEHRP B/C site condition (i.e., V_{S30} = 760 m/s.)

We conclude that the generic GMPE approach provides a calibrated model of predicted ground motions in CENA that agrees with average motions from the NGA-East database, and is constrained by simulation-based scaling principles that have been demonstrated to work in California over a wide range of magnitudes and distances. We have provided calibrated median predictions of ground motions in CENA for average horizontal-component peak ground motions and 5%-damped response spectra (up to T = 10 s), for magnitudes **M**3 to **M**8 and distances < 600 km. The approach that we have taken, in casting our model into a framework that is parameterized by the basic seismological parameters of moment, stress, and attenuation, has both conceptual and practical advantages. We can easily create understandable and documentable alternative GMPEs, by considering a range of possible parameter values that might be reasonable for the region (or a subset of the region). For each parameter set, we may use the empirical data to derive a new calibration factor for each frequency, such that the overall residuals are

minimized for the given model. Analysis of the residual trends and their variability under the alternative models then provides information on the limitations of the alternative parameter sets.

4.6   Data and resources

We compiled the response spectra of ground motions for CENA earthquakes from the NGA-East flatfile provided by Christine A. Goulet (written commun., 2014). Ground-motion simulations were performed using the SMSIM v3.8 software that is available at http://www.daveboore.com/software_online.html (last accessed in October 2014). All graphics were produced using CoPlot software (www.cohort.com, last accessed in February 2015).

4.7   Acknowledgements

4.8   References

Allen, T., P. Cummins, T. Dhu, and J. Schneider (2007). Attenuation of ground-motion spectral amplitudes in southeastern Australia, *Bull. Seismol. Soc. Am.* **97**, 1279–1292.

Ancheta, T., R. Darragh, J. Stewart, E. Seyhan, W. Silva, B. Chiou, K. Wooddell, R. Graves, A. Kottke, D. Boore, T. Kishida, and J. Donahue (2014). PEER NGAWest2 database, *Earthquake Spectra*, **30**, 989-1006.

Atkinson, G. M. (2004). Empirical attenuation of ground-motion spectral amplitudes in southeastern Canada and the northeastern United States, *Bull. Seismol. Soc. Am.* **94**, 1079–1095.

Atkinson, G. M. (2008). Ground motion prediction equations for eastern North America from a referenced empirical approach: Implications for epistemic uncertainty, *Bull. Seismol. Soc. Am.* **98**, 1304–1318.

Atkinson, G. M. (2010). Ground-motion prediction equations for Hawaii from a referenced empirical approach, *Bull. Seismol. Soc. Am.* **101**, 1304–1318.

Atkinson, G. M. (2012). Evaluation of attenuation models for the northeastern United States/southeastern Canada, *Seismol. Res. Lett.* **83**, 166–178.

Atkinson, G. M., and D. M. Boore (1995). Ground-motion relations for eastern North America, *Bull. Seismol. Soc. Am.* **85**, 17–30.

Atkinson, G. M., and D. M. Boore (2006). Earthquake ground-motion prediction equations for eastern North America, *Bull. Seismol. Soc. Am.* **96**, 2181–2205.

Atkinson, G. M., and D. M. Boore (2011). Modification to existing ground-motion prediction equations in light of new data, *Bull. Seismol. Soc. Am.* **101**, 1121–1135.

Atkinson, G. M., and D. Motazedian (2013). Ground-motion amplitudes for earthquakes in Puerto Rico, *Bull. Seismol. Soc. Am.* 103, 1846–1859.

Atkinson, G. M., and W. Silva (2000). Stochastic modeling of California ground motions, *Bull. Seismol. Soc. Am.* **90**, 255–274.

Babaie Mahani, A., and G. M. Atkinson (2012). Evaluation of functional forms for the attenuation of small-to-moderate-earthquake response spectral amplitudes in North America, *Bull. Seismol. Soc. Am.* **102**, 2714–2726.

Boore, D. M. (2003). Simulation of ground motion using the stochastic method, *Pure and Applied Geophysics*, **160**, 635-376.

Boore, D. M. (2005). SMSIM---Fortran programs for simulating ground motions from earthquakes: Version 2.3---A revision of OFR 96-80-A, U.S. Geological Survey Open-File Report, *U. S. Geological Survey Open-File Report* 00-509.

Boore, D.M. (2010). Orientation-independent, non geometric-mean measures of seismic intensity from two horizontal components of motion, *Bull. Seismol. Soc. Am.* **100**, 1830–1835.

Boore, D. M. and E. M. Thompson (2014). Path durations for use in the stochastic-method simulation of ground motions, *Bull. Seismol. Soc. Am.* **104**, 2541–2552.

Boore, D. M. and E. M. Thompson (2015). Revisions to some parameters used in stochastic-method simulations of ground motion, *Bull. Seismol. Soc. Am.* **105**, (in review).

Boore, D. M., K. W. Campbell, and G. M. Atkinson (2010). Determination of stress parameters for eight well-recorded earthquakes in eastern North America, *Bull. Seism. Soc. Am.* **100**, 1632–1645

Boore, D. M., C. Di Alessandro, and N. A. Abrahamson (2014a). A generalization of the double-corner-frequency source spectral model and its use in the SCEC BBP Validation Exercise, *Bull. Seismol. Soc. Am.* **104**, 2387–2398.

Boore, D. M., J. P. Stewart, E. Seyhan, and G. M. Atkinson (2014b). NGA-West2 equations for predicting response spectral accelerations for shallow crustal earthquakes, *Earthquake Spectra*, **30**, 1057-1085.

Brune, J. N. (1970). Tectonic stress and the spectra of seismic shear waves from earthquakes, *J. Geophys. Res.* **75**, 4997–5009.

Burger, R. W., P. G. Somerville, J. S. Barker, R. B. Herrmann, and D. V. Helmberger (1987). The effect of crustal structure on strong ground motion attenuation relations in eastern North America, *Bull. Seismol. Soc. Am.* **77**, 420–439.

Campbell, K. W. (2002). Development of semi-empirical attenuation relationships for the CEUS, Report to U.S. Geological Survey, NEHRP Award No.01HQGR0011.

Campbell, K. W. (2003). Prediction of strong ground motion using the hybrid empirical method and its use in the development of ground-motion (attenuation) relations in eastern North America, *Bull. Seismol. Soc. Am.* **93**, 1012–1033.

Chapman, M. C., and R. W. Godbee (2012). Modeling geometrical spreading and the relative amplitudes of vertical and horizontal high-frequency ground motions in eastern North America, *Bull. Seismol. Soc. Am.* **102**, 1957–1975.

Chapman, M. C. (2013). On the rupture process of the 23 August 2011 Virginia earthquake, *Bull. Seismol. Soc. Am.* **103**, 613–628.

EPRI (2004). CEUS ground motion project final report. Technical Report 1009684. Electric Power Research Institute, Dominion Energy, Glen Allen, VA, Entergy Nuclear, Jackson, MS, and Exelon Generation Company, Kennett Square, PA. Palo Alto, Calif.

Frankel, A. (2009). A constant stress-drop model for producing broadband synthetic seismograms: Comparison with the Next Generation Attenuation Relations. Bull. Seism. Soc. Am., **99**, 664-681.

Hassani, B., and G. M. Atkinson (2014). Referenced empirical ground-motion model for eastern North America, *Seismol. Res. Letters* (in review).

NEHRP (2000). *NEHRP Recommended provisions for seismic regulations for new buildings and other structures, Part 1, Provisions, FEMA 368*, Federal Emergency Management Agency, Washington, D.C.

Ojo, S., and R. Mereu (1986). The effect of random velocity functions on the travel times and amplitudes of seismic waves, *Geophysical Journal of the Royal Astronomical Society* **84**, 607–618.

Ou, G.-B., and R. B. Herrmann (1990). A statistical model for ground motion produced by earthquakes at local and regional distances, *Bull. Seismol. Soc. Am.* **80**, 1397–1417.

Pezeshk, S., A. Zandieh, and B. Tavakoli (2011). Hybrid empirical ground-motion prediction equations for eastern North America using NGA models and updated seismological parameters, *Bull. Seismol. Soc. Am.* **101**, 1859–1870.

Scherbaum, F., J. J. Bommer, H. Bungum, F. Cotton, and N. A. Abrahamson (2005). Composite ground motion models and logic trees: Methodology, sensitivities, and uncertainties, *Bull. Seismol. Soc. Am.* **95**, 1575–1593.

Silva, W., N. Gregor, R. Darragh (2002). Development of regional hard rock attenuation relations for central and eastern North America, Report to Pacific Engineering and Analysis.

Somerville, P., J. McLaren, C. Saikia, and D. Helmberger (1990). The 25 November 1988 Saguenay, Quebec earthquake: Source parameters and the attenuation of strong ground motion, *Bull. Seismol. Soc. Am.* **80**, 1118–1143.

Somerville, P., N. Collins, N. Abrahamson, R. Graves, and C. Saikia (2001). Ground motion attenuation relations for the central and eastern United States, Report to U.S. Geological Survey, NEHRP Award No. 99HQGR0098.

Somerville, P., R. Graves, N. Collins, S. G. Song, S. Ni, P. Cummins (2009). Source and ground motion models of Australian earthquakes, *Proceedings of the 2009 Annual Conference of the Australian Earthquake Engineering Society*.

Toro, G., N. Abrahamson, and J. Schneider (1997). Model of strong ground motion in eastern and central North America: best estimates and uncertainties, *Seism. Res. Lett.* **68**, 41–57.

Yenier, E., and G. M. Atkinson (2014). Equivalent point-source modeling of moderate-to-large magnitude earthquakes and associated ground-motion saturation effects, *Bull. Seismol. Soc. Am.* **104**, 1458–1478.

Yenier, E., and G. M. Atkinson (2015). An equivalent point-source model for stochastic simulation of earthquake ground motions in California, *Bull. Seismol. Soc. Am.* (in review).

Yenier, E., and G. M. Atkinson (manuscript in preparation). Modeling source and attenuation attributes of the 2010-2012 Christchurch, New Zealand earthquakes based on equivalent point-source modeling technique.

Chapter 5

5   Conclusions and future studies

5.1   Summary and conclusion

In this thesis, we derive a regionally-adjustable generic GMPE based on equivalent point-source stochastic simulations. In Chapter 2, we model the source and attenuation attributes of well-recorded $\mathbf{M} \geq 6$ earthquakes based on the equivalent point-source approach, with the goal of determining how to treat ground-motion saturation effects within this context. We consider ground motions as originating from an equivalent point source such that ground motions are correctly predicted at close distances. This is achieved by using an effective distance metric $R = (D_{rup}^2 + h^2)^{0.5}$, where D_{rup} is the closest distance to the rupture and h is a "pseudo-depth" term that accounts for saturation effects. We identify the trade-offs between source and attenuation modeling parameters through analysis of Fourier amplitudes for several alternative attenuation models. We select the best-fitting attenuation model for each earthquake by regression analysis, using the residual statistics as a statistical constraint, and the known seismic moment as a physical constraint. We find that the distance-saturation effect is magnitude dependent, extending to further distances with increasing magnitude. We show that an equivalent point-source model based on the effective distance concept can successfully predict the average ground motions from moderate-to-large magnitude earthquakes over a wide distance range, including close distances (<20 km).

In Chapter 3, we calibrate equivalent point-source stochastic simulations to match the average response spectra for California earthquakes of $3.0 \leq \mathbf{M} < 7.5$. We test the performance of simulations for alternative attenuation models. The best-fit simulation model suggests that the attenuation in California can be modeled as $R^{-1.3}$ at distances < 50 km and $R^{-0.5}$ at further distances; this does a better job at matching attenuation trends than the traditional model $1/R$ model at distances < 50 km, particularly for small magnitude

events. We develop a regional model for the stress parameter using the values obtained from study events, as determined by matching the simulated and observed spectral shapes over a wide period range. The use of spectral shape breaks the trade-off between source and attenuation parameters and ensures that an appropriate corner frequency is determined for each event. Because the stress parameter is based on the spectral shape, the overall level of the spectrum requires an adjustment to match the observed ground-motion amplitudes. We calculate a simulation calibration factor for amplitude adjustment to match the observed response spectra with zero bias. We show that equivalent point-source simulation method with the proposed modeling parameters can predict average ground motions in California, generally within a ±25% error-band, for magnitudes up to **M**7.5, distances < 400 km and frequencies > 0.2 Hz.

Finally in Chapter 4, we develop a generic ground-motion prediction equation (GMPE) that can be adjusted for use in any region by modifying a few key model parameters. The basis of the GMPE is an equivalent point-source simulation model whose parameters have been calibrated to empirical data in California, in such a way as to determine the decoupled effects of basic source and attenuation parameters on ground motion amplitudes. We formulate the generic GMPE as a function of magnitude, distance, stress parameter, geometrical spreading rate and anelastic attenuation coefficient. This provides a fully adjustable predictive model, allowing users to calibrate its parameters using observed motions in the target region. We also include an empirical calibration factor to account for residual effects that are different and/or missing in simulations compared to observed motions in the target region. As an example application, we show how the generic GMPE can be adjusted for use in central and eastern North America (CENA), and calibrated with the NGA-East database. We provide median predictions of ground motions in CENA for average horizontal-component peak ground motions and 5%-damped pseudo spectral acceleration (periods up to T = 10 s), for magnitudes **M**3 to **M**8 and distance up to 600 km.

5.2   Suggestions for future studies

The proposed generic GMPE framework allows derivation of regional predictive models by modifying its source and attenuation parameters using empirical data. As noted earlier, a set of alternative GMPEs can be easily created by considering a range of possible parameter values that might be reasonable for the region, in order to account for uncertainty in modeling parameters. Analysis of the residual trends and their variability under these alternative models can provide information on the limitations of the alternative parameter sets. Additionally, comparison of predictive models adjusted for different regions can provide useful insights for the assessment of variations in source and attenuation attributes between the regions. Finally, predictions of the generic GMPE can provide a useful benchmark against which near-fault motions from large earthquakes can be compared in order to discriminate other extended rupture effects (e.g., hanging-wall/footwall effects and rupture directivity effects) that have not been accounted for by the equivalent point-source modeling technique.

Appendices

Table A.1 Model coefficients of the magnitude term (F_M) and geometrical spreading function (F_Z) in the generic GMPE

T (s)	M_h	e_0	e_1	e_2	e_3	b_3	b_4
0.010	5.85	2.23E+0	6.87E-1	-1.36E-1	7.64E-1	-6.21E-1	6.06E-2
0.013	5.90	2.28E+0	6.85E-1	-1.29E-1	7.62E-1	-6.26E-1	6.13E-2
0.016	5.85	2.27E+0	6.97E-1	-1.23E-1	7.59E-1	-6.31E-1	6.19E-2
0.020	5.90	2.38E+0	7.00E-1	-1.07E-1	7.49E-1	-6.38E-1	6.25E-2
0.025	6.00	2.56E+0	6.84E-1	-9.42E-2	7.41E-1	-6.31E-1	6.10E-2
0.030	6.15	2.81E+0	6.61E-1	-9.09E-2	7.39E-1	-6.03E-1	5.64E-2
0.040	5.75	2.73E+0	7.03E-1	-1.09E-1	7.38E-1	-5.48E-1	4.82E-2
0.050	5.35	2.56E+0	7.19E-1	-1.64E-1	7.54E-1	-5.10E-1	4.28E-2
0.065	5.75	3.00E+0	6.84E-1	-1.55E-1	7.55E-1	-4.67E-1	3.64E-2
0.080	5.20	2.58E+0	7.65E-1	-2.43E-1	7.87E-1	-4.21E-1	3.07E-2
0.100	5.45	2.78E+0	7.12E-1	-2.62E-1	7.94E-1	-3.77E-1	2.47E-2
0.130	5.35	2.64E+0	7.35E-1	-3.32E-1	8.12E-1	-3.55E-1	2.22E-2
0.160	5.25	2.47E+0	8.09E-1	-3.87E-1	8.41E-1	-3.26E-1	1.92E-2
0.200	5.45	2.55E+0	8.19E-1	-3.86E-1	8.43E-1	-2.87E-1	1.38E-2
0.250	5.60	2.52E+0	8.67E-1	-3.77E-1	8.78E-1	-2.43E-1	9.21E-3
0.300	5.85	2.63E+0	8.47E-1	-3.63E-1	8.76E-1	-2.12E-1	5.16E-3
0.400	6.15	2.67E+0	8.50E-1	-3.47E-1	8.97E-1	-1.93E-1	4.85E-3
0.500	6.25	2.54E+0	8.86E-1	-3.49E-1	9.18E-1	-2.08E-1	8.54E-3
0.650	6.60	2.62E+0	8.76E-1	-3.16E-1	9.25E-1	-2.28E-1	1.37E-2
0.800	6.85	2.66E+0	9.05E-1	-2.89E-1	8.94E-1	-2.52E-1	1.91E-2
1.000	6.45	1.99E+0	1.34E+0	-2.46E-1	9.83E-1	-2.97E-1	2.76E-2
1.300	6.75	2.01E+0	1.39E+0	-2.06E-1	1.00E+0	-3.50E-1	3.78E-2
1.600	6.75	1.75E+0	1.56E+0	-1.68E-1	1.05E+0	-3.85E-1	4.43E-2
2.000	6.65	1.25E+0	1.75E+0	-1.32E-1	1.19E+0	-4.35E-1	5.36E-2
2.500	6.70	9.31E-1	1.82E+0	-1.09E-1	1.29E+0	-4.79E-1	6.14E-2
3.000	6.65	5.16E-1	1.91E+0	-8.98E-2	1.42E+0	-5.13E-1	6.76E-2
4.000	6.85	3.44E-1	1.93E+0	-7.47E-2	1.51E+0	-5.51E-1	7.43E-2
5.000	6.85	-7.92E-2	1.98E+0	-6.21E-2	1.59E+0	-5.80E-1	7.90E-2
6.500	7.15	-6.67E-3	1.97E+0	-5.45E-2	1.63E+0	-5.96E-1	8.12E-2
8.000	7.50	2.56E-1	1.94E+0	-5.23E-2	1.59E+0	-6.09E-1	8.30E-2
10.000	7.45	-2.76E-1	1.97E+0	-4.63E-2	1.72E+0	-6.20E-1	8.42E-2
PGA	5.85	2.22E+0	6.86E-1	-1.39E-1	7.66E-1	-6.19E-1	6.03E-2
PGV	5.90	5.96E+0	1.03E+0	-1.65E-1	1.08E+0	-5.79E-1	5.74E-2

Table A.2 Model coefficients of the stress adjustment factor ($F_{\Delta\sigma}$) in the generic GMPE

T (s)	s_0	s_1	s_2	s_3	s_4
0.010	-2.05E+0	1.88E+0	-4.90E-1	5.67E-2	-2.43E-3
0.013	-1.92E+0	1.80E+0	-4.71E-1	5.47E-2	-2.36E-3
0.016	-1.71E+0	1.66E+0	-4.36E-1	5.09E-2	-2.20E-3
0.020	-1.16E+0	1.27E+0	-3.34E-1	3.91E-2	-1.70E-3
0.025	-1.54E+0	1.59E+0	-4.29E-1	5.10E-2	-2.24E-3
0.030	-1.06E+0	1.20E+0	-3.13E-1	3.62E-2	-1.55E-3
0.040	-8.57E-1	1.04E+0	-2.68E-1	3.08E-2	-1.33E-3
0.050	-9.63E-1	9.83E-1	-2.16E-1	2.08E-2	-7.42E-4
0.065	-2.23E+0	1.95E+0	-4.90E-1	5.49E-2	-2.29E-3
0.080	-3.68E+0	2.96E+0	-7.51E-1	8.42E-2	-3.51E-3
0.100	-4.05E+0	3.10E+0	-7.62E-1	8.33E-2	-3.39E-3
0.130	-4.17E+0	3.09E+0	-7.44E-1	7.98E-2	-3.21E-3
0.160	-3.96E+0	2.82E+0	-6.50E-1	6.72E-2	-2.61E-3
0.200	-2.71E+0	1.73E+0	-3.30E-1	2.82E-2	-9.06E-4
0.250	-1.77E+0	9.83E-1	-1.31E-1	6.00E-3	-1.16E-5
0.300	-3.18E-1	-1.39E-1	1.70E-1	-2.85E-2	1.42E-3
0.400	2.02E+0	-1.86E+0	6.12E-1	-7.67E-2	3.34E-3
0.500	3.96E+0	-3.29E+0	9.88E-1	-1.20E-1	5.14E-3
0.650	3.65E+0	-2.82E+0	7.93E-1	-8.93E-2	3.55E-3
0.800	2.40E+0	-1.65E+0	4.09E-1	-3.71E-2	1.05E-3
1.000	1.07E+0	-4.55E-1	3.74E-2	1.03E-2	-1.08E-3
1.300	-2.51E+0	2.52E+0	-8.45E-1	1.21E-1	-6.02E-3
1.600	-5.26E+0	4.74E+0	-1.48E+0	1.96E-1	-9.28E-3
2.000	-6.64E+0	5.77E+0	-1.74E+0	2.24E-1	-1.03E-2
2.500	-8.08E+0	6.84E+0	-2.02E+0	2.54E-1	-1.14E-2
3.000	-7.98E+0	6.64E+0	-1.92E+0	2.37E-1	-1.04E-2
4.000	-7.12E+0	5.78E+0	-1.61E+0	1.90E-1	-7.98E-3
5.000	-6.39E+0	5.08E+0	-1.38E+0	1.58E-1	-6.36E-3
6.500	-4.80E+0	3.68E+0	-9.37E-1	9.76E-2	-3.47E-3
8.000	-3.42E+0	2.51E+0	-5.80E-1	5.15E-2	-1.34E-3
10.000	-2.19E+0	1.51E+0	-2.87E-1	1.53E-2	2.38E-4
PGA	-2.13E+0	1.94E+0	-5.04E-1	5.82E-2	-2.50E-3
PGV	-2.25E+0	1.95E+0	-5.18E-1	6.14E-2	-2.73E-3

Table A.2 (cont'd)

T (s)	s_5	s_6	s_7	s_8	s_9
0.010	-1.44E+0	1.24E+0	-2.89E-1	3.09E-2	-1.25E-3
0.013	-1.35E+0	1.20E+0	-2.80E-1	3.01E-2	-1.23E-3
0.016	-1.08E+0	1.04E+0	-2.47E-1	2.69E-2	-1.11E-3
0.020	-1.27E+0	1.25E+0	-3.17E-1	3.62E-2	-1.55E-3
0.025	-1.45E+0	1.37E+0	-3.37E-1	3.73E-2	-1.54E-3
0.030	-2.24E+0	1.98E+0	-5.09E-1	5.78E-2	-2.44E-3
0.040	-3.31E+0	2.66E+0	-6.68E-1	7.42E-2	-3.06E-3
0.050	-4.23E+0	3.29E+0	-8.32E-1	9.30E-2	-3.87E-3
0.065	-3.96E+0	2.87E+0	-6.67E-1	6.88E-2	-2.65E-3
0.080	-3.14E+0	2.18E+0	-4.67E-1	4.47E-2	-1.60E-3
0.100	-2.45E+0	1.57E+0	-2.89E-1	2.30E-2	-6.57E-4
0.130	-1.38E+0	6.26E-1	-1.16E-2	-1.09E-2	8.28E-4
0.160	-2.00E-1	-3.37E-1	2.57E-1	-4.25E-2	2.18E-3
0.200	8.20E-1	-1.08E+0	4.40E-1	-6.10E-2	2.85E-3
0.250	1.78E+0	-1.77E+0	6.07E-1	-7.83E-2	3.50E-3
0.300	2.25E+0	-2.00E+0	6.33E-1	-7.70E-2	3.27E-3
0.400	2.42E+0	-1.94E+0	5.56E-1	-6.17E-2	2.39E-3
0.500	8.56E-1	-4.53E-1	6.46E-2	5.22E-3	-8.30E-4
0.650	-6.67E-1	9.28E-1	-3.71E-1	6.18E-2	-3.43E-3
0.800	-2.12E+0	2.15E+0	-7.30E-1	1.05E-1	-5.29E-3
1.000	-4.47E+0	4.05E+0	-1.27E+0	1.71E-1	-8.14E-3
1.300	-5.49E+0	4.77E+0	-1.44E+0	1.85E-1	-8.46E-3
1.600	-5.88E+0	4.98E+0	-1.46E+0	1.83E-1	-8.16E-3
2.000	-6.01E+0	4.99E+0	-1.43E+0	1.75E-1	-7.59E-3
2.500	-4.88E+0	3.95E+0	-1.09E+0	1.26E-1	-5.17E-3
3.000	-4.18E+0	3.32E+0	-8.86E-1	9.89E-2	-3.85E-3
4.000	-2.63E+0	1.96E+0	-4.62E-1	4.24E-2	-1.18E-3
5.000	-1.38E+0	9.09E-1	-1.42E-1	1.32E-3	7.11E-4
6.500	-3.93E-1	9.83E-2	9.53E-2	-2.78E-2	1.96E-3
8.000	-6.87E-3	-1.89E-1	1.69E-1	-3.53E-2	2.20E-3
10.000	2.68E-1	-3.86E-1	2.17E-1	-3.97E-2	2.30E-3
PGA	-1.44E+0	1.24E+0	-2.85E-1	3.02E-2	-1.22E-3
PGV	-1.76E+0	1.38E+0	-3.26E-1	3.50E-2	-1.42E-3

Table A.3 Anelastic attenuation coefficients to adjust the generic GMPE for CENA. The corresponding values for California are also shown.

T (s)	γ_{CENA}	$\gamma_{California}$
0.010	-4.66E-3	-9.82E-3
0.013	-4.69E-3	-9.83E-3
0.016	-4.69E-3	-9.83E-3
0.020	-4.67E-3	-9.82E-3
0.025	-4.88E-3	-9.88E-3
0.030	-5.11E-3	-1.01E-2
0.040	-5.27E-3	-1.08E-2
0.050	-5.47E-3	-1.13E-2
0.065	-5.71E-3	-1.19E-2
0.080	-5.79E-3	-1.24E-2
0.100	-5.64E-3	-1.25E-2
0.130	-5.24E-3	-1.22E-2
0.160	-4.77E-3	-1.17E-2
0.200	-4.20E-3	-1.09E-2
0.250	-3.65E-3	-1.02E-2
0.300	-3.12E-3	-9.43E-3
0.400	-2.44E-3	-8.26E-3
0.500	-2.04E-3	-7.36E-3
0.650	-1.64E-3	-6.45E-3
0.800	-1.43E-3	-5.85E-3
1.000	-1.26E-3	-5.13E-3
1.300	-1.06E-3	-4.35E-3
1.600	-1.17E-3	-3.90E-3
2.000	-1.02E-3	-3.36E-3
2.500	-1.06E-3	-3.01E-3
3.000	-1.09E-3	-2.72E-3
4.000	-1.30E-3	-2.12E-3
5.000	-9.35E-4	-1.70E-3
6.500	-7.87E-4	-1.31E-3
8.000	-6.43E-4	-1.06E-3
10.000	-3.65E-4	-8.49E-4
PGA	-4.67E-3	-9.81E-3
PGV	-2.79E-3	-6.31E-3

Curriculum Vitae

Name:	Emrah Yenier
Post-secondary Education and Degrees:	Geophysics, Ph.D., 2015 Western University, London, Ontario, Canada
	Structural Engineering, M.Sc., 2009 Middle East Technical University, Ankara, Turkey
	Civil Engineering, B.Sc., 2005 Middle East Technical University, Ankara, Turkey
Honors and Awards:	Western Graduate Research Scholarships, 2010-2014
	Thesis of the Year Award, 2009 Prof. M. Parlar Education and Research Foundation, Turkey
	Graduate Courses Performance Award, 2006 Middle East Technical University, Ankara, Turkey
Related Work Experience:	Teaching/Research Assistant, 2010-2014 Department of Earth Sciences Western University, London, Ontario, Canada
	Research Assistant, 2009-2010 SHARE: Seismic Harmonization in Europe Project Middle East Technical University, Ankara, Turkey.
	Research Assistant, 2005-2009 Turkish National Strong-Ground Motion Project Middle East Technical University, Ankara, Turkey.

Publications:

Yenier, E., and G. M. Atkinson (2015). Regionally-adjustable generic ground-motion prediction equation based on equivalent point-source simulations: Application to central and eastern North America, *Bull. Seismol. Soc. Am.* (in review).

Yenier, E., and G. M. Atkinson (2015). An equivalent point-source model for stochastic simulation of earthquake ground motions in California, *Bull. Seismol. Soc. Am.* (in review).

Yenier, E., and G. M. Atkinson (2014). Equivalent point-source modeling of moderate-to-large magnitude earthquakes and associated ground-motion saturation effects, *Bull. Seismol. Soc. Am.*, 104: 1458-1478.

Atkinson, G. M., D. W. Greig, and **E. Yenier** (2014). Estimation of moment magnitude (M) for small events (M<4) on local networks, *Seismol. Res. Lett.*, 85: 1116-1124.

Akkar, S., O. Kale, **E. Yenier**, and J. J. Bommer (2011). The high-frequency limit of usable response spectral ordinates from filtered analogue and digital strong-motion accelerograms, *Earthq. Eng. Struct. D.*, 40: 1387-1401.

Akkar, S., Z. Çağnan, **E. Yenier**, Ö. Erdoğan, M. A. Sandıkkaya, and P. Gülkan (2010). The recently compiled Turkish strong-motion database: preliminary investigation for seismological parameters, *J. Seismol.*, 14: 457-479.

Akkar, S., and **E. Yenier** (2009). Assessment of point-source stochastic simulations using recently derived ground-motion prediction equations, *Bull. Seismol. Soc. Am.*, 99: 3172-3191.